



Doctoral Thesis

Microstructures and transport properties of heterogeneous materials

Author(s):

Reuteler, Joakim

Publication Date:

2012

Permanent Link:

<https://doi.org/10.3929/ethz-a-007575842> →

Rights / License:

[In Copyright - Non-Commercial Use Permitted](#) →

This page was generated automatically upon download from the [ETH Zurich Research Collection](#). For more information please consult the [Terms of use](#).

Diss. ETH No. 20266

**MICROSTRUCTURES AND TRANSPORT PROPERTIES OF
HETEROGENEOUS MATERIALS**

A dissertation submitted to

ETH ZURICH

for the degree of

DOCTOR OF SCIENCES

presented by

JOAKIM REUTELER

Dipl. Phys. ETH Zurich

born on June, 15th 1979, citizen of Saanen, Switzerland

accepted on the recommendation of

Prof. Dr. Ludwig J. Gauckler, examiner

Prof. Dr. Markus Hütter, co-examiner

Prof. Dr. Vanessa Wood, co-examiner

Dr. Roger Wepf, co-examiner

2012

Notre tête est ronde pour permettre à la pensée de changer la direction.

Francis Picabia, 1922

Contents

Summary	vi
Zusammenfassung	viii
1 Introduction	1
1.1 Microstructure matters	2
1.2 Theories of heterogeneous materials	4
1.3 Imaging and analyzing microstructures	5
1.4 Scope and aim of the thesis	7
1.5 Outline of the thesis	8
Bibliography	9
2 Backbone of conductivity in two-dimensional metal-insulator composites	11
2.1 Introduction	12
2.1.1 Metal-insulator composites	12
2.1.2 Effective conductivity	13
2.1.3 Theories for the effective conductivity	16
2.1.4 Backbone of conductivity	17
2.2 Methods	19
2.2.1 Computing the effective conductivity	20
2.2.2 Image filter extracting the backbone	21
2.3 Results	23
2.4 Discussion	26
2.5 Conclusions	28
Bibliography	29
3 Networks of spherical particles: microstructure and effective conductivity	32
3.1 Introduction	33
3.2 Experimental	34

3.2.1	Preparation of copper-acrylic composites	34
3.2.2	Imaging of samples	38
3.3	Image processing	39
3.3.1	Processing of raw image data	39
3.3.2	Segmentation of smoothed gray level images	40
3.3.3	Extraction of percolating cluster and removal of small cavities	41
3.4	Estimation of effective conductivity	43
3.5	Characterization of microstructures	44
3.5.1	Betti numbers	44
3.5.2	Number of particles	45
3.5.3	Number of contacts	45
3.5.4	Critical radii	45
3.6	Results and discussion	46
3.7	Conclusions and outlook	49
	Bibliography	51

4 Simulation of electrical conduction in a micro-solid oxide fuel cell chip 53

4.1	Introduction	54
4.2	Simulation of electrostatics	56
4.2.1	Effective resistance of the current collector	59
4.2.2	Total power output of the chip	60
4.3	Results	65
4.4	Discussion	69
4.5	Conclusions	72
	Bibliography	73

5 Focused ion beam scanning electron microscope 76

5.1	Technological aspects of the FIB-SEM	76
5.1.1	Imaging cutting and writing at the nanoscale	77
5.1.2	The Liquid Metal Ion Source (LMIS)	79
5.1.3	Characteristics of FIB columns	84
5.1.4	Interaction of Ga ions with solids	86
5.2	Application of the FIB-SEM	90
5.2.1	Microcontacting	91
5.2.2	Micromechanical testing	92
5.2.3	Holes for various purposes	92
5.2.4	Ion irradiation	92
5.2.5	Cross Section	93
5.2.6	Three-dimensional imaging	95
5.2.7	TEM lamella preparation	98

5.2.8	Preparation of samples for APT	101
5.3	Examples	101
5.3.1	Inner surface of porous ceramic	102
5.3.2	Spatially resolved chemical analysis of grain boundaries in alumina	104
5.3.3	Chemical analysis of impurity phase in TZP	107
5.3.4	TiO ₂ nanotubes with coatings	111
5.4	Summary and outlook	114
	Bibliography	120
6	Conclusions and outlook	125
	Bibliography	128
A	Transport properties	129
A.1	Transport properties: a class of physical properties	129
A.2	Effective properties of heterogeneous materials	130
A.3	Diffusion and random walks	131
A.4	Estimation of effective transport properties	133
	Bibliography	135
B	Characterization of microstructures	136
B.1	Morphological operations	136
B.2	Minkowski functionals	138
B.3	Particle size from granulometry	142
	Bibliography	142
	Acknowledgements	144
	Curriculum Vitae	146

Summary

The overwhelming majority of man-made materials are heterogeneous: they are composed of different phases at the microscopic scale. The spatial distribution of the phases - the microstructure - has a major influence on the properties observed at the macroscopic scale. The classical theories of heterogeneous materials are largely based on assumed microstructures, because hitherto it has been hardly possible to gain detailed three-dimensional real-space information of microstructures. The recent advances in microscopy techniques as well as handling of spatial data sets enable us to explore directly the relation between complex microstructures and effective properties.

The aim of this thesis is to relate transport properties of heterogeneous materials to their microstructures. The focus is on metal-insulator composites and steady state effective transport properties, such as electrical conductivity. Our results, however, may be ported to describe diffusion of gases or solutes through porous materials as well as heat conduction through heterogeneous materials.

Concerning two-dimensional metal-insulator composites, e.g. porous platinum thin films used as electrodes in micro-solid oxide fuel cells, we developed an image filter that extracts that part from the metal phase which is relevant for electrical conduction. The filter is a generalization of the backbone from percolation theory. Using a collection of microstructures, for which we compute the effective conductivity by the finite element method before and after filtering, we show that the backbone filter changes the effective conductivity only in the range of few percent even for cases where the filter tremendously reduces the area fraction of the metal. Hence the backbone filter allows to reduce the microstructural complexity of a conductor-insulator composite, without altering its effective transport properties substantially. The backbone filter can be used to reduce computational effort in numerical studies and also provides a first step towards an estimator of the effective transport properties of conductor-insulator composites based on microstructural quantities.

In order to search for microstructural quantities that determine the effec-

tive transport properties in three-dimensional microstructures we investigate model metal-insulator microstructures represented by binary images. These studied microstructures consist of networks formed by spherical particles with contacts resembling sinter-necks. The images were created from micrographs of copper-polymer composites acquired by x-ray tomography. On the one hand we use the binary images to estimate the effective conductivity of the networks by a random walk technique and on the other hand we compute several microstructural quantities from them. One of the investigated quantities, namely the number of loops (the second Betti number), correlates well with the effective conductivity as opposed to other microstructural quantities such as the number of particle-particle contacts or the area of the critical contact for percolation. This indicates that the number of loops, which characterizes the topology of the networks, can be used as additional input for mixing rules besides the volume fraction of the conducting phase to describe the effective conductivity of metal-insulator composites.

Complex geometries occur often in microsystems, i.e., chips for data processing, sensing and energy conversion. Proper design of such devices includes optimization of the geometry of their components. We apply simulation of electrostatics to quantify the ohmic losses due to transport through a metal thin film used as current collector in a micro-solid oxide fuel cell chip containing individual fuel cells generating power. The chip integrates 30 cells that operate in parallel. The spatial arrangement of the current sources and the current sink results in a nontrivial modulation of the power delivered by the individual cells. The effect is studied as function of both the intrinsic cell losses and the thickness of the conducting platinum thin film connecting the cells. The results enable to optimize these geometrical parameters in order to get a high total performance from the chip at high power outputs of the individual cells.

The approach pursued in this thesis is coined by analysis of microstructures which itself is tightly bound to microscopy techniques. The final chapter of this thesis reviews the focused ion beam scanning electron microscope, which allows to image cut and write at the nano scale. The capabilities of this instrument are due to the combination of high resolution imaging by state of the art scanning electron microscopes with the microstructuring capabilities of a highly focused beam of gallium ions. We illustrate the use of this instrument in the field of materials science by several examples of microstructure analyses which either cannot be conducted with other methods or are carried out particularly efficiently with the presented technique.

Throughout this thesis image analysis and the concept of effective properties play a key role. In the appendices the relevant theoretical background is summarized in a self-contained manner.

Zusammenfassung

Der Grossteil der industriell hergestellten Materialien sind heterogen: sie zeigen auf der mikroskopischen Skala mehrere Phasen welche verschiedene physikalische Eigenschaften aufweisen. Die räumliche Anordnung der Phasen - die Mikrostruktur, auch das Gefüge genannt - hat massgeblichen Einfluss auf die makroskopisch beobachteten Eigenschaften solcher Materialien. Klassische Theorien der heterogenen Materialien basieren weitgehend auf angenommenen Mikrostrukturen, denn bisher war es nur schwer möglich detaillierte dreidimensionale Realraum-Informationen von Mikrostrukturen zu erhalten. Die Entwicklung bildgebender Verfahren mit geeigneter Auflösung und ausgeprägtem Materialkontrast in den letzten Jahrzehnten eröffnen uns die Möglichkeit den Zusammenhang zwischen effektiven Eigenschaften von heterogenen Materialien und deren Mikrostruktur direkt zu untersuchen.

Diese Doktorarbeit verfolgt das Ziel die Transporteigenschaften von heterogenen Materialien mit ihren Mikrostrukturen zu verbinden. Das Hauptgewicht liegt dabei auf Verbundmaterialien einer leitenden und einer isolierenden Phase und deren stationären Transporteigenschaften, wie der elektrischen Leitfähigkeit. Im Prinzip sind die gewonnenen Resultate jedoch auch auf die Diffusion von Gasen oder den Transport gelöster Teilchen in einer Flüssigkeit in porösen Materialien, sowie der Wärmeleitung in heterogenen Materialien übertragbar.

Bei der Betrachtung von zweidimensionalen Metall-Isolator Kompositen, wie sie in Form von porösen Platindünnschichten als Elektroden in miniaturisierten Feststoffelektrolytbrennstoffzellen eingesetzt werden, wurde ein Bildanalysefilter entwickelt, welcher den für die elektrische Leitfähigkeit relevanten Teil der Metallphase extrahiert. Dieser Filter ist eine Verallgemeinerung des "backbone" (Rückgrat) aus der Perkolationstheorie. Anhand unterschiedlicher metallischer Mikrostrukturen wurde die Änderung der elektrischen Leitfähigkeit vor und nach Anwendung des backbone Filters mit Hilfe der finite Element Methode berechnet. Es zeigt sich, dass diese Änderung der Leitfähigkeit im Bereich einiger Prozent liegt, auch wenn die Flächenfraktion der Metallphase durch den backbone Filter drastisch erniedrigt wird. Demzufolge

erzielt der backbone Filter eine erhebliche Verminderung der mikrostrukturellen Komplexität ohne dabei die effektive Leitfähigkeit wesentlich zu verändern. Der Filter kann eingesetzt werden um den Rechenaufwand in numerischen Studien zu reduzieren. Ausserdem eignet er sich als erster Schritt für eine näherungsweise Bestimmung der elektrischen Leitfähigkeit von komplexen Gefügen aus mikrostrukturellen Grössen.

Auf der Suche nach mikrostrukturellen Grössen, welche die effektive Leitfähigkeit dreidimensionaler Mikrostrukturen bestimmen analysieren wir Modellgefüge von Metall-Isolator Verbundmaterialien welche durch dreidimensionale binäre Bilder dargestellt werden. Die untersuchten Modellgefüge bestehen aus Netzwerken von kugelförmigen Partikeln mit Kontakten die Sinterhalsen ähneln. Die Bilder wurden aus röntgentomographischen Aufnahmen von Kupfer-Polymer Verbundmaterialien erzeugt. Ausgehend von den binären Bildern wurde einerseits die effektive Leitfähigkeit durch eine Zufallspfadmethode geschätzt und andererseits eine Anzahl mikrostruktureller Grössen der Partikelnetzwerke bestimmt. Eine der betrachteten Grössen, die Anzahl Schleifen (die zweite Bettizahl), zeigte eine gute Korrelation mit der effektiven Leitfähigkeit, wohingegen andere Gefügegrössen wie die Anzahl Partikel-Partikel Kontakte und die Fläche des für Perkolation kritischen Kontakts keine gute Korrelation zur effektiven Leitfähigkeit zeigen. Es deutet dies darauf hin, dass es sich ist die Anzahl Schleifen eines Netzwerks als zusätzliche Eingabegrösse neben dem Volumenanteil der leitfähigen Phase für empirische Mischregeln zur Schätzung effektive Leitfähigkeit nutzen lässt.

Komplexe Geometrien treten häufig in Mikrosystemen auf, zum Beispiel in Mikrochips zur Datenverarbeitung und für die Messtechnik oder zur Energiewandlung. Die Entwicklung solcher Systeme beinhaltet eine Optimierung der Geometrie der einzelnen Komponenten. Durch eine Simulation der Elektrostatik von passiven und aktiven Elementen konnten die Verluste aufgrund des Energietransports durch den metallischen Dünnsfilm, welcher als Stromsammelr die 30 einzelnen Mikrobrennstoffzellen auf einem Siliziumeinkristallchip parallel verbindet, quantifiziert werden. Die räumliche Anordnung der Quellen und Senken im Stromsammelr führen zu einer nicht trivialen Modulation der Leistung der einzelnen Mikrobrennstoffzellen. Dieser Effekt wird als Funktion des Flächenwiderstands und der Einzelzelleistung untersucht. Die Resultate erlauben eine Optimierung dieser geometrischen Parameter um bei hohen Einzelzelleistungen auch eine hohe Gesamtleistung aller Zellen auf dem Chip zu erzielen.

Der Ansatz welcher in dieser Doktorarbeit verfolgt wird ist durch die Analyse von Gefügen heterogener Materialien geprägt, diese wiederum hängt stark von der Mikroskopiertechnik ab. Das letzte Kapitel gibt einen Überblick der "focused ion beam scanning electron microscope" Technik, welche das Abbilden, Schneiden und Schreiben auf der Micro- bis Nanoskala ermög-

licht. Das System kombiniert die hohe Abbildungsauflösung moderner Rasterelektronenmikroskope mit den Mikrostrukturierungsmöglichkeiten eines hoch fokussierten Galliumionenstrahls. Der Einsatz dieses Gerätes wird anhand verschiedener Fragestellungen aus der Materialwissenschaft illustriert, welche entweder nicht anders gelöst werden können, oder mit Hilfe der gezeigten Methode besonders effizient angegangen werden können.

Die gesamte hier präsentierten Arbeit basiert auf Methoden der Bildanalyse und dem Konzept der effektiven Transporteigenschaften. In den Anhängen werden die relevanten theoretischen Grundlagen in weitgehend eigenständiger Weise zusammengefasst.

Chapter 1

Introduction

On the one hand we may claim that materials science is the oldest science that mankind pursues, since procedures to shape materials and to enhance their properties have been known and developed already in prehistoric times. On the other hand material science and engineering has existed as an own discipline only for about hundred years. Why is this?

A systematic approach to improving and controlling the properties of materials requires a proper understanding of the chemistry and physics of materials. More importantly the concept of microstructure had to be discovered. For this to happen powerful microscopes had to be enter the arena of science. The visualization of dark lines moving in a metal during its deformation proved the dislocation theory. This discovery enabled the development of steels with unprecedented properties, and at the same time initiated the study of the relation between microstructure and physical properties. Material science is the art of controlling the microstructure by processing and thereby the properties of the material. The importance of microscopes for materials science is highlighted by the following quote.

*In order to make you need to see.*¹

This chapter is organized as follows. In the first section we point out the relevance of material science for mankind, explain the notion of a microstructure and present an example from the field of ceramics to illustrate how the microstructure affects properties of materials. The second section gives an overview of the theoretical concepts that exist to describe the relation between microstructure and physical properties. The third section provides a brief account of nowadays possibilities to image microstructures. In the four

¹Thomas F. Kelly in a talk given at ETH Zurich on January 5th, 2011.

section the aims of the present thesis are formulated. This chapter concludes with an outline of the contents of the remainder of the thesis.

1.1 Microstructure matters

Research in the field of materials science and engineering concerns the development of new materials and their processing. The goals of such research may be one or several of the following: improving a physical property by orders of magnitude, combining certain properties in one material and precise tuning of the properties of the material. Regarding these goals the potential of materials composed of a single phase, so called homogeneous materials, is quite limited. Most technologically relevant materials are mixtures of different phases, so called heterogeneous materials, because they offer an additional degree of freedom to affect their physical properties by tailoring the amount and distribution of the different phases.

What is a microstructure?

To the human eye most materials appear homogeneous. However, using a microscope we can reveal that ceramics or metals actually are composed of tightly joined grains, i.e., regions with a uniform chemical composition and fixed crystal structure. Furthermore materials containing grains of different chemical composition exist, these are composite materials. A grain usually is homogeneous, however, it may contain a small region occupied by a foreign phase, a so called inclusion. The term microstructure refers to the spatial arrangement of phases within a material. Composition and microstructure are the two factors that determine the properties of a heterogeneous material. In some cases the interface between two phases may become an own phase, e.g. by creating a two-dimensional electron gas.

The microstructure of a material constitutes infinitely many degrees of freedom. In practice a complete characterization is out of question, and the aim is rather to find few easily computable microstructural characteristics which permit a reasonable description of the properties of the material. Polycrystalline materials are usually characterized using the grain size distribution. Composite materials are typically characterized by the volume fractions of the constituent phases. This, however, gives no information on how the phases are arranged with respect to each other. In theory this problem is overcome using the complete family of n -point correlation functions which contain all information on a microstructure in statistical sense [1]. Unfortunately the computational cost of higher order correlation functions prohibits their extensive use in practice. Therefore easily computable quanti-

ties that contain information of the microstructure beyond volume fractions are being sought for.

Transparent alumina

In the mid 1950ies the high pressure sodium vapor lamp was being developed at General Electric (GE). In low pressure sodium lamps, which did already exist at that time, the sodium arc is operated in quartz (SiO_2) tubes. If a high pressure sodium arc is operated in such a conventional arc tube it darkens within an hour of operation. This effect is caused by the chemical reaction of the hot sodium vapor with the silicon in the arc tube. A chemically more stable material for making arc tubes had to be found. Alumina (Al_2O_3) does withstand both the high temperature and the chemical attack of the high pressure sodium arc. However, at that time alumina was a lousy material in terms of its mechanical properties. Even worse, its opaque white appearance would prohibit its use as arc tube for a lamp. GE was fortunate enough to hire the young material scientist Robert L. Coble who found a way to produce translucent aluminum oxide. Under the trademark LUCALOX, standing for transLUCent ALuminum OXide, GE sells high pressure sodium lamps containing such alumina arc tubes until today. Application of these lamps for traffic and building illumination makes this a major business.

To understand what gives LUCALOX its extraordinary properties we need to discuss the basics of ceramics processing. Industrial production of alumina parts starts with bringing alumina powder into the desired shape. This so called green body is then sintered: exposed to elevated temperature the atoms become mobile and a rearrangement resulting in shrinkage of the macroscopic dimensions of the alumina part. On the microscopic scale a reduction of porosity and an increase of the grain size is observed. Depending on the details of the grain size distribution in the green body and the temperature program different microstructures of the final ceramic are obtained. Sintering in air yields irregular grain boundaries due to inclusion of nitrogen captured by closed porosity. Such grain boundaries and pores strongly scatter light. To reach theoretical density in pure alumina, high temperature treatment is necessary. This, however, also triggers discontinuous grain growth: giant grains form next to regions where the grains hardly grow. Such highly irregular grain structure results in alumina parts with lousy properties.

In 1961 Coble reported that a small addition of magnesia (MgO) to alumina powder compacts resulted in earlier sintering and furthermore absence of discontinuous grain growth [2]. Furthermore he realized that the amount of residual porosity was much lower when sintering under hydrogen atmosphere, because in contrast to nitrogen the hydrogen gas trapped in closed

porosity could diffuse interstitial through the ceramics. In 1962 he patented his technique for producing transparent ceramics [3]. The findings of Coble initiated the field of transparent ceramics: since then dopants suitable to produce other transparent ceramic materials have been found [4]. The mechanism by which the dopant assists the sintering process varies from case to case. In case of alumina the magnesia doping presumably both equalizes the grain boundary energies and enhances the self diffusion in alumina.

1.2 Theories of heterogeneous materials

Controlling the microstructure means controlling the properties, fine - but how exactly does this work? Which microstructural feature relates to which change of the properties in a specific material? There is no universal answer to this question. To engineer a material that possesses a certain profile of properties one approach is to mix materials that offer at least one of the required properties. No doubt, this pragmatic approach has provided us with a multitude of high tech materials. The limitation of the approach, however, lies in the time required to perform the experiments and the cost for equipment and manpower. In order to conduct systematic engineering of the properties of materials we need to explore the link between the microstructure to the properties of heterogeneous materials given the properties of the constituents.

All approaches to describe properties of heterogeneous materials are based on the idea that the heterogeneous material can be replaced by an equivalent homogeneous material. The intuition behind this approach is that the spatial modulation of the physical properties present at small length scales is averaged over large length scales, resulting in an effective property that has no spatial variation in case the microstructure is statistically equal throughout the material. There is also a rigorous justification for this idea. Homogenization is the mathematical discipline concerned with the study of the limits of partial differential equations with oscillating coefficients [5]. The information on microstructure and the properties of the constituent phases is coded in the spatially oscillating coefficients. The limit process represents the transition from the microscopic to the macroscopic length scale. The result is a differential equation that describes a homogeneous medium, possibly with a modulation of its properties on the macroscopic length length scale. The coefficients of the homogenized equation represent the effective properties, i.e., the properties of the homogeneous material which is equivalent to the heterogeneous material when considered at large length scales. Another valuable result from homogenization are bounds for the effective properties. There is a whole hierarchy of such bounds based on the n -point

correlation functions.

Materials composed of a matrix with a dilute addition of inclusions can be described well by effective medium theories [6]. Such theories are also known as mixing rules. For given volume fractions they predict the effective property in terms of an analytic expression.

Percolation theory is a unifying concept capable of describing problems ranging from spread of diseases to electrical conduction in metal-insulator composites [7]. The common ground is the critical dependence of the effect of interest on the existence of a connected network, called percolating cluster. The downside of the theory is that it relies on the assumption that the network is formed randomly.

Let's assume we know the microstructure and the properties of the constituents of a heterogeneous material. How can we determine its effective properties from this information in practice? According to homogenization theory we have to solve the boundary value problem describing measurement of the physical property of interest for a sufficiently large volume element. The problem with this answer is that it does not provide an insight on the relation between microstructure and properties.

The Finite Element Method (FEM) allows solving boundary value problems with complex boundary conditions. The main limitation of this method is the size of the system that can be handled with current computer power. For some cases it is possible to use probabilistic techniques such as simulation of random walks. This approach has the drawback that one order in magnitude more precision has to be paid with two orders of magnitude more computational effort.

1.3 Imaging and analyzing microstructures

The microstructures of metals were the first to be investigated extensively, hence the term metallography was coined. The procedure consists of three major steps: sample preparation, microscopy and image analysis. This remains true until nowadays and is applied for all kinds of materials.

A typical goal of a microstructural investigation is to estimate the grain size and grain size distribution of a polycrystalline material. First a small sample of the material is cut to expose its interior. Then it is polished until a shining flat cross section is obtained. Often etching either by wet chemistry or by thermal treatment is applied to make the grain boundaries visible. With a light microscope images with a clear contrast between grain and grain boundary are recorded. The grain size is then extracted for example by means of the lineal method. The latter is one of many techniques from stereology [8]. The lineal method also allows to determine the internal

surface area of a porous materials, see Sec. 5.3.1. Two-dimensional images of a microstructure yield a wealth of information, but in general nothing can be said about the spatial connectivity of the microstructure. This fact is illustrated in Fig. 1.1.

By today three-dimensional imaging of microstructures has become a standard technique. In terms of resolution the whole range from atomic to macroscopic scale can be covered by at least one technique, see Fig. 1.2. Due to the larger amount of information contained in three-dimensional images a higher computational effort is necessary for processing such images. Data sets of some 10^7 voxels are typically used since they can be handled by standard computers and yet are large enough for many kinds of microstructures in terms of being representative of the structure.

Image analysis concerns both the enhancement of image quality and the extraction of useful information. The distinction is somewhat fuzzy since already removal of noise requires a decision about which kind of features in the image are attributed to noise and which represent the microstructure. The information provided by an image can either be qualitative or quantitative. Very often qualitative information answers scientific questions. For example we may be interested whether a certain phase is distributed evenly throughout a material or accumulates at grain boundaries. An image showing the spatial concentration profile is sufficient to answer this question. In contrast to this situation we may ask why is the conductivity of sample A

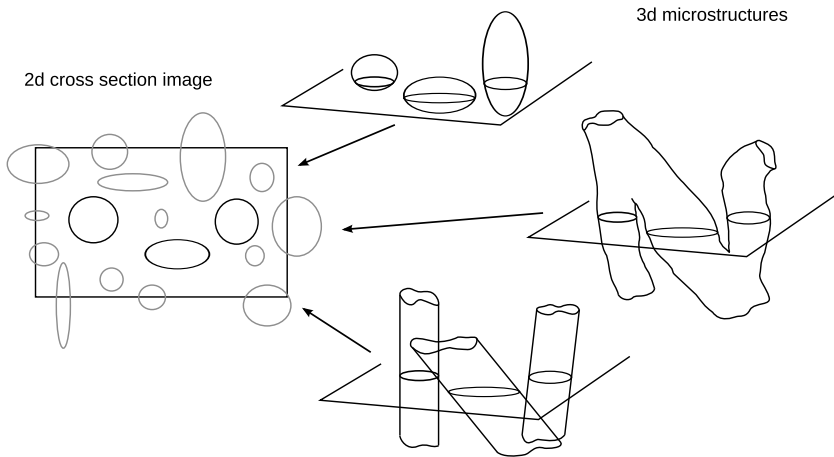


Figure 1.1: Several three-dimensional (3d) microstructures with very different connectivity can yield the same two-dimensional (2d) cross sectional image.

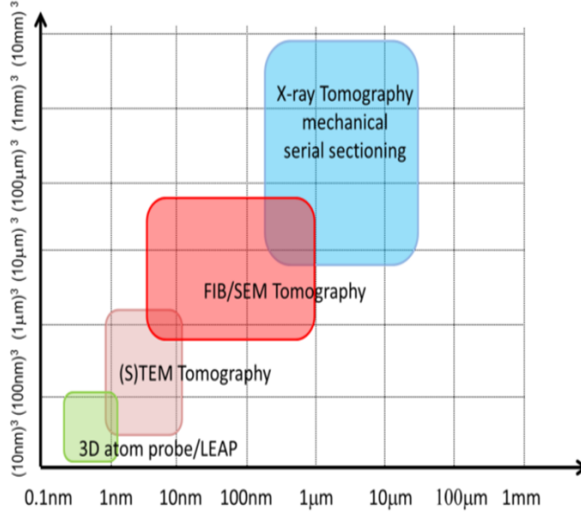


Figure 1.2: Overview of microscopy techniques illustrating their range of applicability regarding image volume and pixel size. (Illustration reproduced by courtesy of Marco Cantoni, CIME, École Polytechnique Fédérale de Lausanne)

50 % higher than for sample B. In case both samples have qualitatively the same microstructure the answer lies in a quantitative difference of a certain microstructural characteristic.

1.4 Scope and aim of the thesis

The present thesis is concerned with the relation between the microstructure and effective transport properties of conductor-insulator composites. Here the term “transport properties” refers to the following three mathematically equivalent physical properties: electrical conductivity, thermal conductivity and diffusivity (see App. A.1). Hence by the term “conductor” we understand a phase which can sustain either electrical, thermal or material transport. The insulating phase blocks such transport completely. In reality there are hardly systems with truly infinite phase contrast, however, in many cases several orders of magnitude separate the transport property of the constituent phases. Bearing this in mind conductor-insulator composites cover a broad range of heterogeneous materials. Porous cermets (ceramic-metal composites) are for example used as anodes in solid oxide fuel cells. The

ceramic conducts oxygen ions, the metal conducts electrons and the pore space sustains gas transport.

As explained in Sec. 1.2 percolation theory concerns the sharp transition between zero transport and finite transport in random structures. The question of how transport properties relate to microstructural quantities is thereby left open. The aim of the present thesis is to explore the methods of image analysis in order to better describe the relation between the microstructure and the effective properties of conductor-insulator composites. Structures within the conducting phase which govern the effective transport shall be identified. Furthermore microstructural quantities that can be used to describe the effective transport properties should be sought for. The full microstructure is too detailed information, thus the goal is to extract those features which are relevant for transport. The starting point are actual microstructures rather than assumed or modeled synthetic microstructures. This approach is encouraged by the nowadays availability of detailed microstructure images.

1.5 Outline of the thesis

The red line of the present thesis is formed by the use of micrographs of microstructures. Throughout they are the object of concern. The bulk of the thesis deals with their quantification. Only in Chp. 5 the focus is on the microscopy method. Two chapters concern two-dimensional microstructures and one deals with three-dimensional structures. As mentioned above and explained in detail in App. A.1 all results derived for electrical transport apply equally for heat transport and diffusion.

We now briefly summarize the contents of each chapter.

Chp. 2 presents an image filter, called backbone. The backbone filter extracts that part from the conducting phase of a metal-insulator composite which contributes to the electric transport. Using a variety of two-dimensional microstructures we confirm quantitatively that the backbone filter is suited to describe electrical transport and hardly affects the effective conductivity although it might remove quite large parts of the original metal phase.

Chp. 3 deals with model microstructures of metal-insulator composites. The metal phase consists of a network formed by spherical particles with contacts resembling sinter-necks. The effective conductivity, as estimated using a random walk technique, shows a good correlation with the number of loops in the networks. This indicates that the number of loops, which is a topological quantity, may be used besides the volume fraction as additional input for empirical mixing rules in order to increase their accuracy and range

of applicability.

Chp. 4 concerns a silicon single crystal based chip that integrates 30 miniaturized solid electrolyte fuel cells. The device employs a platinum thin film as current collector to join all the anodes of the cells and to deliver the generated electrical current to the external power consumer. Using the finite element method the influence of the current collector on the total chip output power is studied. The effect of the spatial arrangement of the individual fuel cells and the current sink on the total power output of the chip is discussed in detail and suggestions for optimizing the chip layout are presented.

Chp. 5 is a review on the focused ion beam scanning electron microscope and its use in the field of materials science. First the physics of ion beams relevant for understanding the possibilities and limitations of the method is discussed. Then applications of the focused ion beam system for preparation of samples for physical characterization as well as imaging are presented. Finally examples of its use for analysis of microstructures are given.

In Chp. 6 the conclusions of the thesis are drawn and ideas for further studies are presented.

Bibliography

- [1] S. Torquato, *Random heterogeneous materials : microstructure and macroscopic properties*. Springer, 2002.
- [2] R. L. Coble, "Sintering crystalline solids. ii. experimental test of diffusion models in powder compacts," *J. App. Phys.*, vol. 32, pp. 793–799, 1961.
- [3] R. L. Coble, "Transparent alumina and method of preparation," U.S. Patent 3 026 210, March 20, 1962.
- [4] A. J. Stevenson, X. Li, M. A. Martinez, J. M. Anderson, D. L. Suchy, E. R. Kupp, E. C. Dickey, K. T. Mueller, and G. L. Messing, "Effect of SiO₂ on densification and microstructure development in Nd:YAG transparent ceramics," *J. Am. Ceram. Soc.*, vol. 94, pp. 1380–1387, 2011.
- [5] D. Cioranescu and P. Donato, *An introduction to homogenization*. Oxford University Press, 1999.
- [6] D. S. McLachlan, M. Blaskiewicz, and R. E. Newnham, "Electrical resistivity of composites," *J. Am. Ceram. Soc.*, vol. 73, no. 8, pp. 2187–2203, 1990.
- [7] P. G. de Gennes, "La percolation: un concept unificateur," *La Recherche*, vol. 7, pp. 919–927, 1976.

- [8] J. Ohser and F. Mücklich, *Statistical Analysis of Microstructures in Materials Science*. John Wiley & Sons, Ltd., 2000.

Chapter 2

Backbone of conductivity in two-dimensional metal-insulator composites¹

Abstract

In percolation theory, the backbone is defined by chopping off dangling ends from the percolating cluster. For structures with high degree of spatial correlation, as they are typical for porous thin films, trimming of the full structure to reveal the part determining the electrical conductivity is more subtle than the classic definition of the backbone. To expand the applicability of the concept, we present a purely geometric definition for the backbone of a two-dimensional percolating cluster. It is based on a sequence of image analysis operations defining the backbone in terms of an image filter. The change of both area fraction and effective conductivity induced by applying the backbone filter to various binary images and a two-parameter family of sets is assessed by numerical means. It is found that the backbone filter simplifies the geometry of complex microstructures significantly and at the same time preserves their electrical DC behavior. We conclude that the backbone will be useful as a first ingredient for a geometric estimator of the effective conductivity of metal-insulator composites.

¹Published in Journal of Applied Physics **110**, 024909 (2011)

2.1 Introduction

At the heart of material science is the development of materials with improved properties. Nowadays many industrially relevant materials belong to the class of composite materials. Based on trial and error, compositions and processing have been optimized. There is no doubt that the microstructure has a crucial influence on the properties of composites. However, there is a lack in theoretical knowledge for relating the microstructure to the properties of such materials [1].

Metallic thin films are employed in various miniaturized devices ranging from microelectronics and micromechanics to miniaturized fuel cells. In particular the electrodes of nowadays best performing low temperature miniaturized solid oxide fuel cells consist of porous platinum thin films [2, 3]. These films have a lateral extension larger than $100\text{ }\mu\text{m}$, a thickness in the range of 100 nm and are flat in the simplest case. Typically they are deposited by magnetron sputtering in a low pressure argon atmosphere. The Pt grains grow in columnar fashion yielding a quasi two-dimensional microstructure. The influence of the microstructure of such electrodes on cell performance is very complex. Thermal stability, amount of electrochemically active sites as well as electrical conductivity have to be optimized. In this study we focus on the electrical conductivity of two-dimensional metal-insulator composites.

We start with a brief review of the notion of composites and explain the relation to binary images. Then we derive the boundary value problem describing electrical conductivity. We briefly discuss present theories describing the effective conductivity of metal-insulator composites. Then we review in detail the definition of the backbone and state the main finding of this study.

2.1.1 Metal-insulator composites

Composite materials consist of a mixture of at least two immiscible phases. Typically the different phases are finely dispersed but the regions occupied by one phase are still large compared to the atomic length scale. The heterogeneous nature becomes apparent in the microscopic range. On the macroscopic scale such composites behave as if they were one-phase materials. This means that there is a length scale such that all samples of the composite larger than a square of this length have statistically the same properties. This idea is closely related to the definition of a so-called representative volume element of a composite. A rigorous study of the approximations adopted by this approach was given by Sab [4]. Therein a practical procedure for determining the effective properties of a composite with microstructure modeled by a random field is given. The properties observed at the macroscopic

scale are called effective properties. They are determined by three factors: the properties of the phases, the properties of the interfaces and the spatial arrangement of the phases. The latter is called microstructure and is exactly what makes composites so attractive: properties can be combined and tuned by altering the microstructure. In a composite it is even possible to obtain properties which never can be observed in one-phase materials [5].

In this study, we consider macroscopically homogeneous two-dimensional metal-insulator composites. The property we investigate is the effective electrical conductivity. We assume that the interface between the metal and the insulator does not develop a conductivity higher than that of the metal, and can hence be neglected. Fixing the conductivity of the metal phase we are interested in the relation between the effective conductivity and the microstructure.

A sample of a metal-insulator composite is a rectangle W with a subset $M \subset W$ that represents the space occupied by the metal phase. The complement M^c is the space occupied by the insulator. A binary image is a discrete representation of such a sample. The white pixels approximate the metal phase and the black pixels approximate the space occupied by the insulator. We thus can interpret any binary image as a sample of a metal-insulator composite. Fig. 2.1(a) shows an example of such a sample. Actually, this image is a thresholded scanning electron micrograph of an agglomerated Pt thin film deposited on a ceramic substrate. The width of the metal rods is in the range of 200 nm.

2.1.2 Effective conductivity

The effective electrical conductivity σ_e of a square sample is determined experimentally by applying a voltage drop V on opposing edges and measuring the current I that flows [Fig. 2.2(a)].

In two dimensions the effective conductivity is defined by

$$\sigma_e = \frac{I}{V}. \quad (2.1)$$

The physics of the measurement of the effective conductivity is described by the Maxwell equations [6]

$$\begin{aligned} \nabla \cdot \mathbf{E} &= 4\pi\rho \\ \nabla \times \mathbf{E} &= -\frac{\partial}{\partial t}\mathbf{B} \\ \nabla \cdot \mathbf{B} &= 0 \\ \nabla \times \mathbf{B} &= \frac{1}{c}\frac{\partial}{\partial t}\mathbf{E} + 4\pi\mathbf{j}, \end{aligned} \quad (2.2)$$

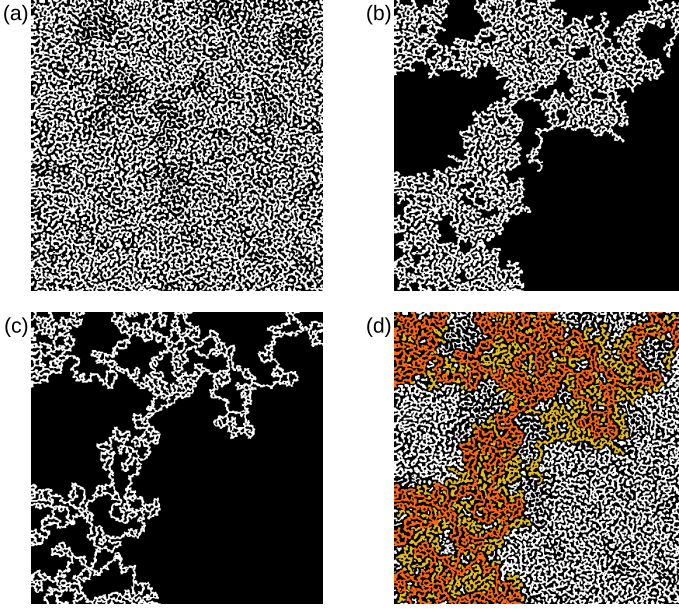


Figure 2.1: (a) Sample of metal-insulator composite represented by a binary image. White pixels represent the metal and black pixels the insulating phase. (b) Percolating cluster of the metal phase obtained by removing isolated islands. (c) Backbone of the percolating cluster obtained by chopping off dead-ends according to the definition presented in this study. (d) Visualization of this division of the metal phase: white for isolated islands, yellow for dead-ends and orange for the backbone.

where \mathbf{E} is the electric field, ρ is the charge density, \mathbf{B} is the magnetic induction and \mathbf{j} is the current density. In the present case all time dependent terms can be dropped. Thus the electric field \mathbf{E} has a potential u , i.e., $\mathbf{E} = \nabla u$. The subset $M \subset W$ is the space occupied by metal, its left boundary is denoted A and its right boundary is B . The remaining boundary of the metal is denoted $C = \partial M \setminus (A \cup B)$, see Fig. 2.2(b). The divergence of the last Maxwell equation shows that the current density is solenoidal, i.e., $\nabla \cdot \mathbf{j} = 0$. This implies that no current flows across the boundary C , i.e., $\mathbf{n} \cdot \mathbf{j} = 0$ on C , where \mathbf{n} denotes the normal vector on C . To see this, consider a box of width $\epsilon > 0$ around a piece of the boundary and integrate the divergence of the current density. Apply Gauss' theorem and then let $\epsilon \rightarrow 0$. Within a metal the current density is proportional to the electric field, i.e., $\mathbf{j} = \sigma \nabla u$ (Ohm's law), where $\infty > \sigma > 0$ is the isotropic and constant conductivity

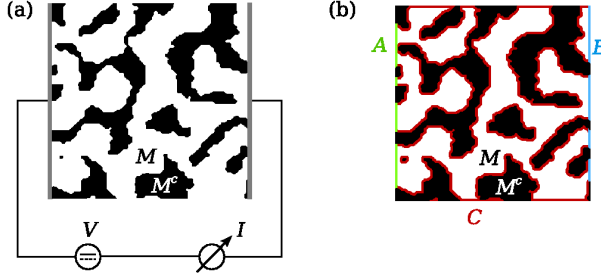


Figure 2.2: (a) Experimental setup for measurement of the horizontal effective conductivity of a metal-insulator composite. (b) Geometry of the boundary value problem describing the physics of the measurement of the effective conductivity.

of the metal. Thus we get $\mathbf{n} \cdot \nabla u = 0$ on C . Within the metal M we have $0 = \nabla \cdot \mathbf{j} = \nabla \cdot \sigma \nabla u = \sigma \Delta u$. Considering all this, we get the following boundary value problem

$$\begin{aligned} \Delta u &= 0, & \text{on } M \\ \mathbf{n} \cdot \nabla u &= 0, & \text{on } C \\ u &= 0, & \text{on } A \\ u &= V, & \text{on } B \end{aligned} \quad (2.3)$$

for the electric potential u . The total current through the sample is $I = \sigma \int_B \mathbf{n} \cdot \nabla u \, d\mu$. Using Eq. (2.1) the effective conductivity is given by

$$\sigma_e = \sigma \frac{\int_B \mathbf{n} \cdot \nabla u \, d\mu}{V}. \quad (2.4)$$

We now derive an alternative expression for the effective conductivity from Eq. (2.4). Without changing the value of the integral we can replace the integrand by $\frac{1}{V} u \nabla u \cdot \mathbf{n}$ and extend the integration to the whole boundary of M . Using $\nabla \cdot u \nabla u = |\nabla u|^2 + u \Delta u$ we can apply Gauss' theorem. Since u satisfies the Poisson equation we have shown that the effective conductivity can be computed by the following energy functional

$$\sigma_e = \sigma \frac{\int_M |\nabla u|^2 \, d\mu}{V^2}. \quad (2.5)$$

The dependence of the effective conductivity on the geometry of the metal phase M is implicit for both of these expressions.

2.1.3 Theories for the effective conductivity

It is an old problem to describe the effective conductivity of metal-insulator composites in terms of their microstructure [7]. In principle the area fraction and the spatial arrangement of the metal phase determine the effective conductivity. The question is how to reduce this information to one number giving the effective conductivity. Solving the boundary value problem given by Eq. (2.3) on a computer is limited by the complexity of the set representing the metal phase. There is no way to determine the effective conductivity in an efficient way directly from the microstructure. Various approaches to the problem have been made. We refer to the following monographs [5, 8] and the short and transparent review [9]. We now comment on the relevant results.

So called effective medium theories result in expressions which link the area fraction of metal directly to the conductivity. The exact form is determined analytically from assumptions on the microstructure. The expressions from Bruggeman's symmetric and asymmetric media theory can be interpolated yielding a general effective media equation [9]. Interestingly for metal-insulator composites this equation reduces to the expression which is postulated in percolation theory.

In percolation theory [10] the effective conductivity is assumed to follow a power law above the percolation threshold ϕ_c , i.e.,

$$\sigma_{PT}(\phi) = \sigma \left(\frac{\phi - \phi_c}{1 - \phi_c} \right)^t, \quad (2.6)$$

where ϕ is the area fraction of metal. The critical exponent t should be universal for fixed space dimension. Unfortunately it cannot be computed directly and so has to be determined from fitting Eq. (2.6) to experimental and simulation data. The percolation threshold ϕ_c depends on the underlying lattice. For two dimensions the values have been determined analytically for the possible lattices. The theory is only valid for the case of structures where each site has a fixed probability to be occupied, independent of all other sites. Therefore in practice both ϕ_c and t are treated as fitting parameters in order to accommodate small deviations from purely uncorrelated random structures.

Using homogenization theory rigorous bounds for the effective conductivity have been derived. Based on information coded in the n -point correlation functions there is a whole hierarchy of nontrivial upper bounds for the effective conductivity. We summarize the review and the formulae given in a monograph by Torquato for the case of a metal-insulator composite in two dimensions [8]. The two-point correlation function yields a bound which, interestingly, only depends on the area fraction ϕ covered by the metal. It

reads

$$\sigma^{(2)}(\phi) = \sigma \frac{\phi}{2 - \phi}, \quad (2.7)$$

and is called upper Hashin-Shtrikman bound [11, 12]. The three-point upper bound is much more tedious to compute. Expressions given by Prager [13] and Beran [14] were later simplified: it was shown that the three-point bound can be written using a threefold integral of the three-point correlation function of the metal [15, 16]. This functional is often denoted by $\zeta \in [0, 1]$. An algorithm for the computation of ζ from discrete images was reported by Berryman [17]. There seems to be no simple interpretation of ζ , see [16]. In this notation the three-point bound reads

$$\sigma^{(3)}(\phi, \zeta) = \sigma \frac{\phi \zeta}{1 - \phi + \zeta}. \quad (2.8)$$

The four point bounds were also computed [16]. In two dimensions the four-point parameters vanish. The upper four-point bound depends only on ϕ and ζ , it reads

$$\sigma^{(4)}(\phi, \zeta) = \sigma \frac{\phi \zeta}{2 - 2\phi + \phi \zeta}. \quad (2.9)$$

All the corresponding lower bounds are trivial for metal-insulator composites in two-dimensional space.

2.1.4 Backbone of conductivity

Only the metal belonging to the percolating cluster can carry a nonzero current density. Thus isolated islands can be neglected. By experiment Last and Thouless showed that the effective conductivity is not proportional to the area fraction of metal in the percolating cluster [18]. Their explanation was that only a small fraction of the sites belonging to the percolating cluster actually carry current. If the percolating cluster represents a resistor network, dangling bonds lead to resistors that carry no current and are dead-ends in this sense. The backbone of the percolating cluster was then defined as the part of the percolating cluster which carries current [19, 20]. The way to compute the backbone is left unclear in the latter publications. Later Kirkpatrick defined the backbone to be the maximal biconnected component of the percolating cluster [21]. An algorithm to compute this was already at hand before [22, 23]. More efficient algorithms were found later [24, 25]. However, this definition of the backbone does not allow for dead-ends with a minimal width larger than one. For example a branch of width two is biconnected to its mother branch because a one pixel wide path can go into it and return without crossing itself. The biconnected component of the percolating cluster in Fig. 2.1(b) actually is equal to the percolating cluster.

Recently another definition for dead-ends of a set was given by Jørgensen [26]. His definition is based on computing traveling distances when going from one edge to the opposing one. This is done by solving the Eikonal equation with constant velocity within the foreground. Then the shortest path is reconstructed by back tracing from the destination edge towards the departure edge. The algorithm works in any space dimension. In fact the most direct path is computed, i.e., detours are chopped off. Therefore this definition of “dead-ends” does not generalize the earlier definitions discussed above.

The original definition of the backbone as the current carrying part of the percolating cluster is based on the idea that there are parts of the percolating cluster in which the current density vanishes. This only holds for discrete networks of ideal resistors. Let’s assume that a percolating metal cluster in continuous space contained a part that carries no current at all. Mathematically speaking this means that there is an open subset $O \subset M_{PC}$ within the percolating metal cluster where the current density $\sigma \nabla u$ vanishes. This implies that the potential u is constant in this subset. Since u is the solution of an elliptic partial differential equation it possesses the “unique continuation property” and thus the potential has to be constant on the whole percolating cluster M_{PC} . Consequently the current density vanishes on M_{PC} which is in contradiction to the fact that a percolating cluster will carry current if its ends are subject to a potential drop. Thus the current density in the percolating cluster is zero nowhere. So by the original definition the backbone is equal to the percolating cluster. In other words dead-ends do not exist, there are only broadened rods carrying lower current density. Looking at Eq. (2.5) we see that the effective conductivity can only decrease if parts of the percolating cluster are truncated. We found a subset of the percolating cluster whose effective conductivity is only slightly smaller.

In the remainder of this paper we present an algorithm based on image analysis operations, which is able to reduce the percolating cluster significantly in mass while leaving the effective conductivity essentially constant. In this sense we give a geometrical definition of the backbone of conductivity. An example of the result of our algorithm is shown in Fig. 2.1(c). The invariance of the effective conductivity is observed for various samples represented by binary images and a two-parameter family of sets, see Figs. 2.3 and 2.4(c). In contrast to the original definition of the backbone as used in percolation theory our definition contains the case of dead-ends of arbitrary width. Therefore the backbone of the percolating cluster shown in Fig. 2.1(b) is a proper subset according to our definition. The backbone as defined by Jørgensen is more restrictive than the one presented here. His definition frees the percolating cluster from all detours, whereas our backbone may contain detours as long as the starting and end point are separate.

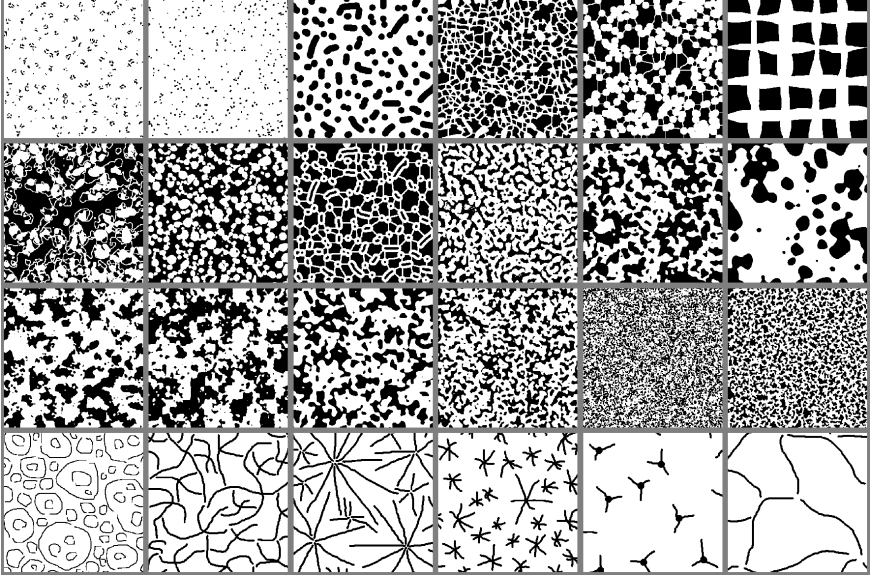


Figure 2.3: Montage of the binary images representing metal-insulator composites investigated in this study. In all images the metal phase is represented by white.

See the loops in Fig. 2.1(c) on the upper right side.

For the purpose of this study it is irrelevant if the binary images are smaller than the representative volume element of the random sets they were taken from.

2.2 Methods

Samples of metal-insulator composites are the basis of this study. On the one hand we use binary images with the size of 500x500 pixels (Fig. 2.3). These images were obtained from microscopy, simulation of random fields and freehand drawing. The aim was to generate a broad range of microstructures. On the other hand we use square symmetric subsets of the unit square [Fig. 2.4(a)]. They are determined by two parameters, the width of the rods ensuring percolation and the side length of the central square. The width of the rods a was varied at equal steps of 0.2 from 0.1 to 0.9 in units of the side length of the image window. For each such value the range of the side length of the central square b was varied between a and the side length of the image window. For each of the five values of a , parameter b was chosen

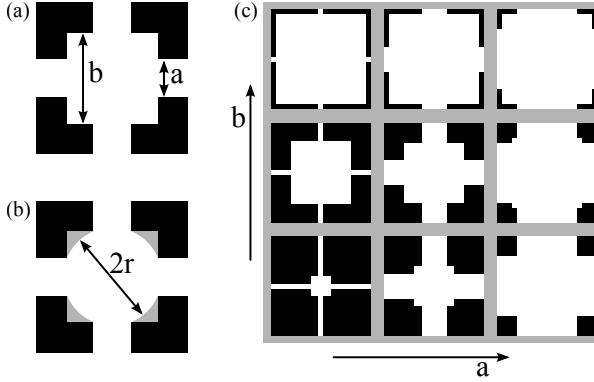


Figure 2.4: (a) A simple two-parameter family of sets representing the microstructure of a metal-insulator composite consisting of a single percolating cluster. (b) Backbone according to the definition given in Eq. (2.10) with dead-ends shown in gray. (c) Illustration of the sets obtained for small, middle and large values of the two parameters a and b .

to take on 20 equally spaced values. Some examples of sets obtained by varying the two parameters are given in Fig. 2.4(c). It will become clear in Sec. 2.3 that the pairs (ϕ, σ_e) obtained from such sets cover a large fraction of all combinations attainable by macroscopically isotropic metal-insulator composites.

2.2.1 Computing the effective conductivity

The computation of the effective conductivity was made by the finite element method using the commercial software COMSOL. The binary images were converted to meshes by a partially self-written code. In the first step ordered lists containing the coordinates of the pixels belonging to a connected piece of boundary were generated. Each such list represents a polygonal approximation of the boundary of a connected piece of the metal phase. The second step is to fill the interior of these polygons with a triangular mesh. After setting the boundary values the Poisson equation was solved by the software. The standard direct solver for the linear system was used. All images and their backbones were used to solve two boundary value problems: one for the setup where the horizontal conductivity is measured and one for the vertical setup.

The square symmetric sets and their backbones were generated by union of rectangles and disks. A script sweeping the two parameters, as detailed above, generated the samples, set the boundary values and solved the Poisson

equation automatically.

For every sample and its backbone the area fraction of the metal phase was computed from the mesh representation that was used to solve the boundary value problem.

2.2.2 Image filter extracting the backbone

The image filter we present is composed of different traditional image processing operations. In Sec. 2.3 it is shown that the image filter introduced only slightly decreases the effective conductivity. We therefore call the filter BackBone (BB). All image processing operations used were implemented from scratch in C++ to allow incorporation of modifications of these operations. The labeling of clusters of white pixels is done by the algorithm originally proposed by Hoshen and Koopelman [27]. A cluster is considered to percolate the image window, if it connects to all four edges. White pixels need to share an edge to be considered connected, while black pixels are considered connected if they share at least a corner. As a consequence of these requirements, in two dimensions the Percolating Cluster (PC) is unique, if it exists. The Euclidean Distance Transform (EDT) was implemented according to the algorithm of Saito and Toriwaki [28]. It assigns to each white pixel the Euclidean distance to the next black pixel. Finally the computation of the SKeleton by Influence Zones (SKIZ) is based on the algorithm published by Soille and Vincent [29]. Here the clusters of black pixels are considered water basins and the EDT values of the white pixels as height of a mountain landscape. The watersheds of this landscape are the SKIZ of the white pixels, they are formed by those crests that separate different basins. The basins must be labeled using 8-connectivity, since the white pixels are subject to 4-connectivity. For our purpose it was necessary to add to the SKIZ all white pixels which lie along the boundary of the image. This makes sure that the SKIZ of a percolating cluster is again a percolating cluster, see bottom right in Fig. 2.5. We denote this operation by SKIZb, standing for SKeleton by Influence Zone with boundary. To obtain the backbone we composed the above mentioned filters in the following way

$$\begin{aligned} \text{BB} : M \subset W &\mapsto M_{\text{BB}} \subset M, \\ M_{\text{BB}} &= \bigcup_{p \in \text{PC} \circ \text{SKIZb}(M)} b_{\text{EDT}(M)|_p}(p), \end{aligned} \quad (2.10)$$

where $b_{\text{EDT}(M)|_p}(p)$ is the maximal disk contained in M centered at the point p . The formula states that the BB is the subset of the white pixels which is covered by maximal disks sitting on the percolating cluster of the SKIZb. This is shown schematically in Fig. 2.5. The less metal pixels are present



Figure 2.5: The backbone (BB), shown in yellow, is the union of maximal disks centered on the percolating part of the SKkeleton by Influence Zones with boundary (SKIZb), here shown in orange. For the green SKIZb-pixel the maximal disk associated with it is shown.

in the input image, the faster is the computation of image transformations. Thus extracting the percolating cluster of the metal phase before proceeding as given by Eq. (2.10) will speed up the computation of the backbone for many cases.

Typically the above filter results in loss of boundary pixels. This is a severe drawback, if the metal phase consists of structures that are only few pixels wide. To circumvent this problem, we dilate the set obtained from the above filter with a 3×3 structuring element, this amounts to adding a one pixel thick layer of white pixels at all boundaries between white and black pixels. Then we intersect this image with the input image to make sure that the result is a subset of the input set. For very fine structures however pixels sharing only a corner with the pixels of the backbone are added in this step, so another application of the filter extracting the percolating cluster is needed. In formulae this reads

$$\tilde{M}_{BB} = PC(\delta_{3 \times 3}(M_{BB}) \cap M). \quad (2.11)$$

For all binary images we use \tilde{M}_{BB} , but we drop the tilde from now on, since the difference between \tilde{M}_{BB} and M_{BB} is essentially a technical detail.

For the case of the two-parameter square symmetric sets described above, the backbone can be determined by hand from Eq. (2.10). The SKIZ is a simple cross made up of two lines. Taking the union of the maximal disks on this cross amounts to replacing the centered square of side length b with a disk of radius $r = \frac{1}{4}\sqrt{b^2 + a^2}$, as shown in Fig. 2.4(b).

2.3 Results

The basic data for each sample and its backbone consists of the triple

$$\left(\sigma_e^{(ver)}, \sigma_e^{(vhor)}, \phi\right) \quad (2.12)$$

of effective conductivities in vertical setup, horizontal setup and the area fraction covered by metal. Therefrom the mean value of the effective conductivity

$$\sigma_e = \frac{1}{2} \left(\sigma_e^{(ver)} + \sigma_e^{(hor)} \right) \quad (2.13)$$

was computed. The relative difference for the conductivity in horizontal and in vertical setup ranges from 0 to 0.25 relative to the mean. Most samples show a relative difference smaller than 0.1. We will from now on only consider the mean conductivity of samples and their backbone, i.e., $\sigma_e(M)$ and $\sigma_e(M_{BB})$ respectively, instead of the conductivities in horizontal and vertical setup.

In Fig. 2.6(a) the normalized mean conductivity of the samples represented by binary images is plotted versus the area fraction of metal. For each sample an asterisk shows the value $(\phi(M), \sigma_e(M)/\sigma)$ obtained from

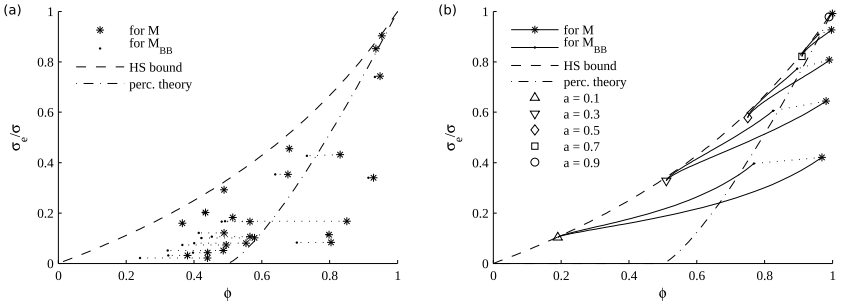


Figure 2.6: (a) Normalized mean effective conductivity for samples of metal-insulator composites represented by binary images versus the area fraction covered by metal. The points $(\phi, \sigma_e/\sigma)$ plotted as asterisk were obtained from the unfiltered images and those plotted as dots from the backbones. The dotted lines connect corresponding pairs of unfiltered and filtered images. (b) Effective conductivity for the samples represented by the two-parameter sets versus area fraction. Each pair of curves joining at an open symbol is obtained from sets with parameter a fixed, see legend, and varying parameter b . See Fig.2.4 for an illustration of the meaning of the two parameters.

the unfiltered image. The dot shows the value $(\phi(M_{BB}), \sigma_e(M_{BB})/\sigma)$ obtained after passing the image through our filter. The dotted lines connect corresponding pairs. The dashed line shows the upper Hashin-Shtrikman bound, see Eq. (2.7). The dash-dotted line shows the curve for bond percolation on the square grid, i.e., percolation threshold $\phi_c = 0.5$ and critical exponent $t = 1.3$ in Eq. (2.6), see [10]. Fig. 2.6(b) shows the plot for the pairs $(\phi, \sigma_e/\sigma)$ obtained from the two-parameter sets both filtered and unfiltered ones. As described in Sec. 2.2 the values of parameter a , the minimal width of the rods, are coarsely spaced. The values for parameter b , the side length of the central square, are narrowly spaced. Let's keep the value of a fixed for a moment. Varying parameter b the points $(\phi, \sigma_e/\sigma)$ range over a continuous curve once for the unfiltered set and once for its backbone. The open symbols code the value of a as indicated by the legend. At the minimal value of parameter b the set consists of a simple cross and thus is identical to its backbone. Furthermore it has minimal area fraction and conductivity. Thus the curves for the filtered and unfiltered sets meet at the side of small area fraction. For increasing values of b the area fraction and the conductivity increase and the unfiltered and filtered set become more and more different regarding area fraction. On the side of high area fraction each curve is marked with either an asterisk indicating that it corresponds to unfiltered sets or with a dot for the filtered sets. The curves for the unfiltered sets evidence that the majority of the area below the Hashin-Shtrikman bound is filled when the values of both parameter a and b are varied continuously in their admissible range. Surely, for $\phi = 1$ the range $0 \leq \sigma_e/\sigma < 1$ cannot be covered and if $\sigma_e = 0$ then necessarily $\phi = 0$ for the sets of the two parameter family.

The relative difference between the effective conductivity of the filtered and unfiltered sample is shown in Fig. 2.7 for every sample. The x-axis in this plot is the relative change of area fraction induced by the filter. Samples which are almost identical to their backbone are located at small relative change of area fraction. The relative difference in effective conductivity for the samples represented by binary images, shown in Fig. 2.7(a), is in the range of a couple of per mill. Only one sample yields a relative change in effective conductivity in the range of one percent. It is the third from left in the last row of Fig. 2.3. This observation is discussed in more detail in Sec. 2.4. Again for the samples represented by two-parameter sets each chosen value of a yields a continuous curve for varying b . Notice that in this case the relative difference in effective conductivity increases with increasing relative change of area fraction induced by the backbone.

In Fig. 2.8, the ratio between the effective conductivity of each sample and the Hashin-Shtrikman bound was computed once using the area fraction of the unfiltered sample and once using the area fraction of the

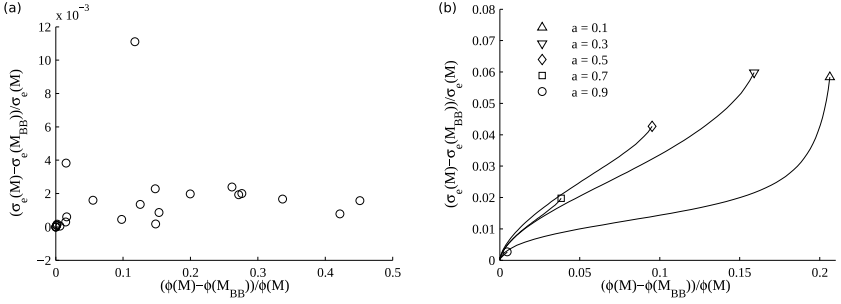


Figure 2.7: Relative difference of the mean effective conductivity of the filtered and unfiltered samples. The data for the binary images is shown on the left side (a) and the data for the two-parameter sets on the right side (b). The x-axis is the relative reduction of area fraction of metal when reducing the sample to its backbone. The curves in the plot in panel (b) correspond to varying parameter b and fixed value of parameter a , as indicated by the legend.

backbone. The ratio of the effective conductivity of a sample to the value of the Hashin-Shtrikman bound [Eq. (2.7)] computed from the area fraction of the backbone, i.e., $\frac{\sigma_e(M)}{\sigma^{(2)}(\phi(M_{BB}))}$ is plotted versus the ratio of the effective conductivity to the value of the Hashin-Shtrikman bound evaluated at the area fraction of the unfiltered sample, i.e., $\frac{\sigma_e(M)}{\sigma^{(2)}(\phi(M))}$. The meaning of these

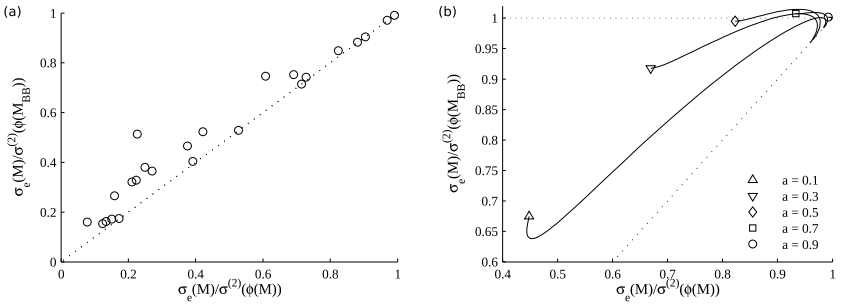


Figure 2.8: The ratio of the effective conductivity and the Hashin-Shtrikman bound evaluated using the area fraction of the backbone is shown versus the ratio of the effective conductivity evaluated at the area fraction of the sample as is. (a) The data for the binary images. (b) The data for the two-parameter sets.

expressions will be discussed in Sec. 2.4. Fig. 2.8(a) shows the plot for the samples represented by binary images. All data points lie above the diagonal (dotted line) and are smaller than one. The corresponding plot for the samples represented by the two-parameter sets is shown in Fig. 2.8(b) where again all values are above the diagonal (dotted line), but here some values larger than one occur.

All samples represented by a binary image were used to generate two other images by filtering once and twice. For every sample their difference was then computed. It was found for all studied samples that the second application of the BB filter did not change the once filtered image.

2.4 Discussion

In this section speaking of the “backbone” we mean the image filter $BB : M \rightarrow M_{BB}$, as defined by Eq. (2.10), as well as the resulting set M_{BB} .

We will first discuss the change in the effective conductivity induced by the backbone. The backbone is always a subset of the sample itself, i.e., $M_{BB} \subset M$. This implies that the effective conductivity of the backbone is a lower bound for the effective conductivity of a sample, i.e.,

$$\sigma_e(M) \geq \sigma_e(M_{BB}), \quad \forall M. \quad (2.14)$$

In other words the error in conductivity induced by reducing the sample to its backbone $\sigma_e(M) - \sigma_e(M_{BB})$ is never negative. This implies that the errors obtained for the horizontal and vertical setup cannot cancel each other when taking the mean of the conductivity from these two setups, Eq. (2.13). For most of the samples represented by the binary images the relative error in mean conductivity is below 0.3 % as can be seen in Fig. 2.7(a). The one data point close to 1.2 % stems from the binary image with the “line stars” (third from right in the bottom line in Fig. 2.3). The sharp corners close to the star centers are chopped off by the backbone. The sum of the current density in these regions appears to be considerably large. Still the data shows that the conductivity of the samples and the respective backbones are very close. This is what the name backbone refers to: electrical conductivity is essentially sustained by the backbone. The plot in Fig. 2.7(a) shows the relative error versus the relative reduction of area induced by the backbone. There is no apparent correlation between the error and the area reduction, thus it is less important how much metal is removed rather than where it is removed from.

In the case of the samples represented by the two-parameter family of square symmetric sets (see Fig. 2.4) the relative error in conductivity reaches values up to 7 %, see the plot in Fig. 2.7(b). This is significantly larger than

for the case of the binary images (Fig. 2.3). The reason is that the corner parts of the central square are not retained by our backbone as illustrated in Fig. 2.4(c). However, the current density in these “dead-ends” seems to be quite large. The effect is more pronounced for sets with large change of area induced by the backbone, i.e., large value of parameter b (the side length of the central square). This shows that large step like changes in the width of a rod are primarily responsible for the change in effective conductivity after filtering with the BB. The sets of the two-parameter family range over microstructures which are worst case structures regarding the backbone. By cutting the sample as represented in Fig. 2.4(a) into four squares swapping positions over the diagonals and joining again to one big square an alternative representation looking like a Swiss cross is obtained. It can be shown by symmetry arguments that it is equivalent in terms of effective conductivity to the original representation. Interestingly this representation reveals the microstructural similarity to the sample with the star shaped inclusions (Fig. 2.3, bottom line, third from right) discussed earlier.

We now comment on the relation between conductivity and the area fraction of metal. The existence of a percolating cluster in the metal phase is a 0-1 criterion for the effective conductivity. If there is no percolating cluster the effective conductivity is necessarily zero, else it has an unknown positive value. If the area fraction is known, the effective conductivity is limited to the interval $[0, \sigma^{(2)}(\phi)]$, see Eq. (2.7). From Fig. 2.6 we see that the area fraction of metal in the backbone is not proportional to the effective conductivity: the data points $(\phi(M_{BB}), \sigma_e(M_{BB})/\sigma)$ scatter over a broad area. There can be well connected backbones with evenly distributed mass or such which have bottlenecks limiting the transport capacity. Nevertheless the backbone optimizes a given metal phase in the sense that the most wasted metal is removed. The remaining set is closer to the optimal one: the data points for the backbones lie closer to the Hashin-Shtrikman bound than those of the unfiltered samples.

Fig. 2.8 shows plots of the data where the x-axis is a measure for how efficiently the metal present in the sample contributes to the effective conductivity. If the value of $\frac{\sigma_e(M)}{\sigma^{(2)}(\phi(M))}$ is one, the microstructure M is optimal in the following sense. For given metal content $\phi(M)$ there is no microstructure with an effective conductivity larger than $\sigma_e(M)$. Knowing that only the backbone M_{BB} carries significant current we interpret $\sigma^{(2)}(\phi(M_{BB}))$ as an estimator for the effective conductivity $\sigma_e(M)$ of the metal insulator M . Now the y-axis of the plots in Fig. 2.8 has the meaning of the accuracy of this estimator. Values below one indicate an overestimation of the effective conductivity, whereas values larger than one indicate underestimation of the effective conductivity. The dotted line shows the quality of the Hashin-Shtrikman bound when interpreted as an estimator for the effective

conductivity. The data points in Fig. 2.8 in general lie above the diagonal, this means that $\sigma^{(2)}(\phi(M_{BB}))$ is closer to the true value $\sigma_e(M)$ than the Hashin-Shtrikman bound is. Thus using the area fraction of the backbone leads to an improved estimator for the effective conductivity based on the Hashin-Shtrikman bound. However, many of the values of the quality are well below one. So this representation of the data clearly shows that the mass of the backbone can be distributed more or less efficiently regarding transport. The less efficiently the metal is distributed regarding conductivity, the more off is the estimated value for the conductivity.

As pointed out in Sec. 2.1.4, the notion of a dead-end is trivial if the criterion of no current flowing through it is applied strictly. Because the transition from “local broadening” of a rod to a long sideways protrusion is continuous there is no canonical way to define the backbone. The longer a dead-end is, the smaller will the current density at its tip be. This suggests using a threshold for the current density in order to define which parts can be chopped off. However, this would require that the current density field were known and thus is not useful in the present context. In order to be easily computable the dead-ends and the backbone have to be defined by geometrical means. Our definition of the backbone and thus of dead-ends is based on image analysis and so is purely geometric. The image analysis operations used dictate the precise position of the cut between backbone and dead-end. The data of the effective conductivity for filtered and unfiltered images indicates that our definition is meaningful.

We finally comment on the observation that repeated application of the BB to all images studied here, resulted in no further change after the first application. We conjecture that this holds for any image, i.e., we argue that the BB is an idempotent set operation. From its definition we see that the BB is anti-extensive, i.e., it maps a set to a subset of itself. Together these two properties would make the BB a morphological filter [30].

2.5 Conclusions

The classic definition of the backbone of a percolating cluster was extended with regard to identification of the electrically conducting backbone of two-dimensional metal-insulator composites. This allows to extract the backbone from any structure containing a percolating cluster. From a numeric study of the effective conductivity we conclude that the backbone filter frees a given structure from those parts which are irrelevant for its steady state DC transport properties. This opens the way for further geometrical characterization with the aim to develop a geometrical estimator for transport properties. For example, it would be interesting to investigate whether the microstruc-

tural characteristic ζ , mentioned in Sec. 2.1.3, can be used to construct a reasonably accurate estimator for the effective conductivity. An immediate idea is to compute $\zeta(M_{BB})$, i.e., its value after filtering by the backbone. Together with $\phi(M_{BB})$, the area fraction of metal after filtering, they could be inserted in either the three- or four-point bound [Eqs. (2.8),(2.9)] to obtain an estimate of the effective conductivity. The advantages of a purely geometric approach in contrast to the simulation of electrostatics are speed of the algorithms and lower memory requirement. Due to equivalence or similarity of the governing equations the backbone will also be useful to treat elasticity, thermal conductivity, transport by diffusion and fluid or gas flow in porous media [8].

From the mathematical point of view our finding shows that it is possible to approximate the solution of a boundary value problem defined on a spatially complex set by the solution on a subset, which is in general less complex. This could help to push the limits of the size of systems that can be simulated.

Acknowledgements

For their interest in the topic, the hint to Eq. (2.5) and helpful discussions the author would like to thank Prof. Camillo De Lellis and Elisabetta Chiodaroli from the Institute for Mathematics at the University of Zurich. The contact to them was initiated by Prof. Jürg Fröhlich at ETH Zurich, whose stimulating input during several discussions is also acknowledged. JR thanks his colleagues Henning Galinski, Pierre Elser and Lukas Schlagenhauf for providing micrographs of dewetted Pt thin films (Fig. 2.1(a) and fourth from left in second line in Fig. 2.3). Furthermore the author would like to thank Dr. Andreas Rüegg and Prof. Ralph Spolenak for their encouragement and hints to improve the manuscript. Finally, financial support by Gloor Instruments is acknowledged.

Bibliography

- [1] M. Wang and N. Pan, “Predictions of effective physical properties of complex multiphase materials,” *Mater. Sci. Eng., R*, vol. 63, pp. 1–30, 2008.
- [2] H. Huang, M. Nakamura, P. Su, R. Fasching, Y. Saito, and F. B. Prinz, “High-performance ultrathin solid oxide fuel cells for low-temperature operation,” *J. Electrochem. Soc.*, vol. 154, no. 1, pp. B20–B24, 2007.

- [3] X. Wang, H. Huang, T. Holme, X. Tian, and F. Prinz, "Thermal stabilities of nanoporous metallic electrodes at elevated temperatures," *J. Power Sources*, vol. 175, pp. 75–81, 2008.
- [4] K. Sab, "On the homogenization and the simulation of random materials," *Eur. J. Mech., A/Solids*, vol. 11, no. 5, pp. 585–607, 1992.
- [5] G. Milton, *The theory of composites*. Cambridge monographs on applied and computational mathematics ; 6, Cambridge University Press, 2002.
- [6] J. D. Jackson, *Classical Electrodynamics*. Wiley, 1990.
- [7] J. C. Maxwell, *Treatise on electricity and magnetism*. Clarendon Pres, 1873.
- [8] S. Torquato, *Random heterogeneous materials : microstructure and macroscopic properties*. Springer, 2002.
- [9] D. S. McLachlan, M. Blaskiewicz, and R. E. Newnham, "Electrical resistivity of composites," *J. Am. Ceram. Soc.*, vol. 73, no. 8, pp. 2187–2203, 1990.
- [10] D. Stauffer and A. Aharony, *Introduction to Percolation Theory*. Boca Raton: CRC Press, 1994.
- [11] Z. Hashin and S. Shtrikman, "A variational approach to the theory of the effective magnetic permeability of multiphase materials," *J. Appl. Phys.*, vol. 33, pp. 3125–3131, 1962.
- [12] Z. Hashin, *Theory of composite materials*. Pergamon Press, 1970.
- [13] S. Prager, "Interphase transfer in stationary two-phase media," *Chem. Eng. Sci.*, vol. 18, pp. 227–231, 1963.
- [14] M. Beran, "Use of variational approach to determine bounds for effective permittivity in random media," *Nuovo Cimento*, vol. 38, no. 2, pp. 771–782, 1965.
- [15] S. Torquato, *Microscopic approach to transport in two-phase random media*. PhD thesis, State University of New York at Stony Brook, 1980.
- [16] G. Milton, "Bounds on the transport and optical properties of a two-component composite material," *J. Appl. Phys.*, vol. 52, no. 8, pp. 5294–5304, 1981.
- [17] J. G. Berryman, "Interpolating and integrating three-point correlation functions on a lattice," *J. Comput. Phys.*, vol. 75, pp. 86–102, 1988.

- [18] B. J. Last and D. J. Thouless, "Percolation theory and electrical conductivity," *Phys. Rev. Lett.*, vol. 27, pp. 1719–1721, 1971.
- [19] A. S. Skal and B. I. Shklovskii, "Topology of an infinite cluster in the theory of percolation and its relationship to the theory of hopping conduction," *Sov. Phys. Semicond.*, vol. 8, no. 8, pp. 1029–1032, 1975.
- [20] P. G. De Gennes, "On a relation between percolation theory and the elasticity of gels," *J. Phys. Lett.*, vol. 37, pp. L1–L2, 1976.
- [21] S. Kirkpatrick, "The geometry of the percolation threshold," *AIP Conf. Proc.*, vol. 40, pp. 99–117, 1978.
- [22] R. Tarjan, "Depth-first and linear graph algorithms," *SIAM J. Comput.*, vol. 1, no. 2, pp. 146–160, 1972.
- [23] J. E. Hopcroft and R. E. Tarjan, "Efficient algorithms for graph manipulation," *Commun. A.C.M.*, vol. 16, pp. 372–378, 1973.
- [24] H. J. Herrmann, D. C. Hong, and H. E. Stanley, "Backbone and elastic backbone of percolation clusters obtained by the new method of 'burning,'" *J. Phys. A*, vol. 17, pp. L261–L266, 1984.
- [25] W.-G. Yin and R. Tao, "Algorithm for finding two-dimensional site percolation backbones," *Physica B*, vol. 279, pp. 84–86, 2000.
- [26] P. S. Jørgensen, *Quantitative data analysis methods for 3d microstructure characterization of solid oxide fuel cells*. PhD thesis, technical university of Denmark, 2010.
- [27] J. Hoshen and R. Kopelman, "Percolation and cluster distribution. i. cluster multiple labelling technique and critical concentration algorithm," *Phys. Rev. B*, vol. 14, pp. 3438–3445, 1976.
- [28] T. Saito and J.-I. Toriwaki, "New algorithms for euclidean distance transformation of an n-dimensional digitized picture with applications," *Pattern Recognit.*, vol. 27, pp. 1551–1565, 1994.
- [29] L. Vincent and P. Soille, "Watersheds in digital spaces: an efficient algorithm based on immersion simulations," *IEEE Trans. Pattern Anal. Mach. Intell.*, vol. 13, no. 6, pp. 583–598, 1991.
- [30] P. Soille, *Morphological image analysis: principles and applications*. Springer, 2nd edition ed., 2004.

Chapter 3

Networks of spherical particles: microstructure and effective conductivity

Abstract

Effective properties allow to describe the behavior of macroscopic workpieces made of heterogeneous materials. However, an efficient method to determine the effective properties directly from the microstructure is lacking. A solution for this problem is to use mixing rules. In order to go beyond the volume fraction typically used as their only input, we investigate the correlation of the effective conductivity with certain microstructural quantities for model metal-insulator microstructures. The metal phase consists of networks of spherical particles with contacts resembling sinter-necks. The model microstructures are represented by binary images derived from x-ray tomographies of samples consisting of copper particles in a polymer matrix. The effective conductivity of the networks is estimated from the binary images using a random walk technique. Furthermore the microstructures are characterized by the number of loops, number of contacts and the critical radius of contacts. We observe a good correlation of the effective conductivity with the number of loops for the studied microstructures. Hence this topological quantity may be used as additional input besides the volume fraction for an empirical mixing rule describing the effective conductivity of metal-insulator composites.

3.1 Introduction

Transport through complex networks occurs in several fields of science. In soil physics transport of water as well as diffusion of solutes are of interest. Petrol industry relies on estimates of oil content and accessibility in reservoir rock. The performance of electrochemical devices depends on the interplay of electrical conductivity, gas diffusion and ionic conductivity in the electrode materials employed. In each field the relation of the microstructure to the transport properties is studied.

Vogel used a connectivity function to describe the morphology of the pore space of two soil horizons [1]. Arns employed Minkowski functions of erosion/dilation radius to tune the parameters of geometrical models to mimic the microstructure of reservoir rock [2]. Wilson computed the tortuosity of the three interpenetrating phases of a solid oxide fuel cell anode using the finite element method [3]. Berson recently employed a simulation of random walks to determine the effective diffusivity of the pore space of electrodes used for solid oxide fuel cells [4]. In spite the relevant physics in the above mentioned examples differs, the equations describing the transport are equivalent in mathematical terms. We here consider as an example the electrical conductivity, but with appropriate translation our results are also relevant to the other above mentioned fields.

The concept of effective properties allows to describe the behavior of macroscopic volumes of heterogeneous materials [5]. The idea is that for given composition and microstructure, a macroscopic volume of heterogeneous material behaves like a fictitious homogeneous material. Unfortunately determining the effective properties for a given microstructure involves great computational effort since complicated boundary value problems must be solved. An approach to circumvent this issue is to use empirical expressions which predict the effective properties from easily computable microstructural quantities. The volume fractions of the constituent phases of composites are the most frequently used input for such models. For overviews on such mixing rules we refer to the literature [6, 7]. The main drawback of mixing rules is that no information on the spatial arrangement of the constituent phases is used as input. To increase the accuracy and applicability of such empirical formulae, microstructural quantities that do depend on the spatial distribution of the phases must be used as additional input. The classical theory of heterogeneous materials is based on the family of n -point correlation functions, which provide complete statistical information of a microstructure [8, 9]. However, in practice the use of higher order correlation functions is hampered by several drawbacks. On the one hand determination of higher order correlation functions involves high computational effort and on the other hand they are complicated multivariate functions. Therefore

alternatives to the correlation functions are sought for.

We study model metal-insulator microstructures, represented by three-dimensional binary images, with the aim to identify microstructural characteristics that are correlated to the effective conductivity. The approach we follow is illustrated in Fig. 3.1. Samples of composites composed of spherical copper particles embedded in a polymer matrix serve as template: the samples are imaged by x-ray tomography and processed into binary three-dimensional images representing networks of spherical particles with contacts resembling sinter-necks. With the present resolution the real microstructure of the composites, where no sinter-necks occur, cannot be captured. In fact all images contain a percolating network of the conducting phase, whereas the measured resistance of the samples shows that three out of five samples are electrically insulating. In other words, a correlation of microstructural characteristics derived from the images with the measured electrical resistance is not meaningful. Therefore we restrict our attention to the binary images, which hence represent *model microstructures*. Using a random walk technique we estimate the effective conductivity of the networks represented by these images. The topology of the networks is characterized by the *number of loops*, also called *second Betti number* b_1 , see Fig. 3.2. Furthermore the number of particles contained in the network is estimated which then allows to estimate the *number of particle-particle contacts* C . The geometry of the networks is characterized by two critical radii. The *critical radius of contacts* r_c^ε is the minimal size of particle-particle contacts required for percolation, and the *critical radius of particles* is the minimal size of particles required to maintain a percolating network. Inspecting the correlation of these microstructural quantities with the effective conductivity singles out the number of loops to be directly related to the effective transport through the investigated networks.

3.2 Experimental

3.2.1 Preparation of copper-acrylic composites

Polydisperse copper powder (ECKA Kupfer AK < 500 μm , ECKA Granules Velden GmbH) was passed through a stack of increasingly finer sieves (Analysesieb, Retsch GmbH). Only the fraction of the copper particles with a diameter between 200 μm and 355 μm was used to prepare the composites. The particle size distribution of this powder fraction was assessed by light microscopy and is shown in Fig. 3.3. Three images taken in transmission mode from some of the copper powder loosely strewn on a glass plate were analyzed. The images were processed using the free software ImageJ [10], as follows below. First noise was reduced by convolution with a Gaussian.

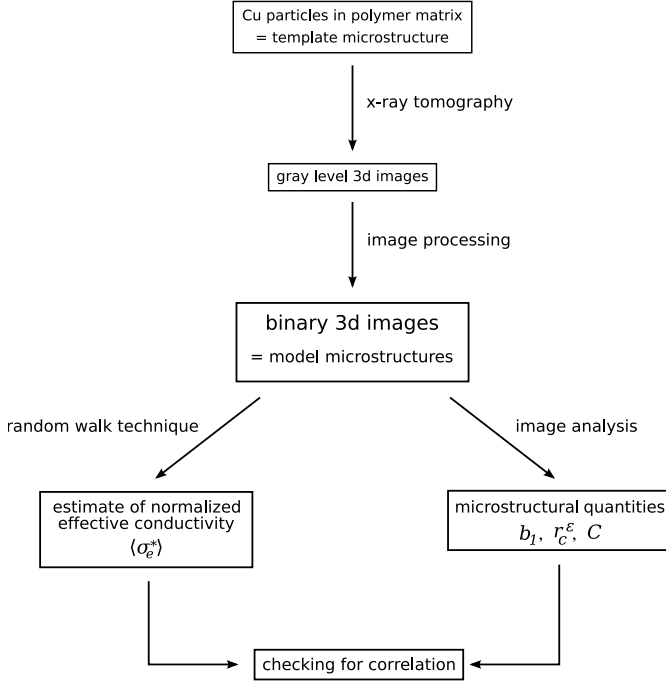


Figure 3.1: Flow diagram of approach to investigate the relation between the effective conductivity and the microstructure of metal-insulator composites. Samples of copper particles in a polymer matrix serve as template to create model microstructures represented by binary three-dimensional images. Based on these images microstructural quantities that show a good correlation with the estimated effective conductivity are identified.

Then the gray level images were segmented to binary images by thresholding. Holes within the copper particles were filled to minimize artifacts from subsequent cutting apart of connected particles by the watershed filter. From the resulting binary images the radius of the area-equivalent disk was computed for each particle. The total histogram of these particle radii for all three images yields the particle size distribution, from which the number weighted mean particle radius was derived: $\langle r \rangle = 125 \pm 24 \mu\text{m}$, where the error is the standard deviation.

The above described fraction of copper powder was mixed with acrylic resin powder (SpeciFast, Struers). The well stirred powder mixture was put in a hot press (LaboPress-3, Struers) to obtain dense composites. All samples had the same volume and shape: cylinders with a diameter of 30 mm

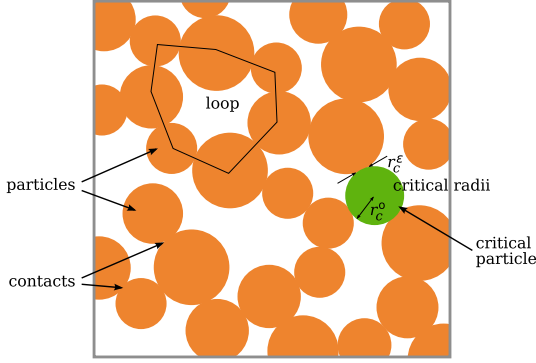


Figure 3.2: Illustration of an image containing a network formed by spherical particles in contact with each other. The second Betti number b_1 is obtained from counting the number of loops in the network, in this image $b_1 = 3$. Upon removal of progressively larger particles the percolation of the network is lost at some point. The critical particle size is denoted by r_c^o and the corresponding critical contact radius r_c^e .

and a height of 20 mm. The hot pressing parameters were the same for all samples: 7 minutes of heating to 180 °C and 5 minutes cooling at a pressure of 241 bar. We aimed for a set of five samples with volume fractions of copper ranging from 40 to 60 vol% in steps of 5 vol%. The powders were mixed by hand thoroughly. However, due to the very different densities of copper and acrylic, demixing during filling into the hot press occurred. For mixtures with low copper content an acrylic rich top layer emerged. Conversely for the copper rich mixtures a top layer depleted of acrylic and some porosity was observed. After the hot pressing the raw cylinders were sawed into quarters and one for each copper load was lathed into a cylinder with a diameter of $d = 5$ mm and a height of $h = 18$ mm. Thereby the macroscopically inhomogeneous parts of the composites were discarded.

To measure the actual volume fractions of copper present in the samples each small cylinder was weighted. All cylinders had the same height h and diameter d . From the measured weight m , the volume fraction of copper ϕ_{Cu} was computed from the following relation,

$$\phi_{Cu} = \frac{m/V - \rho_{acrylic}}{\rho_{Cu} - \rho_{acrylic}}. \quad (3.1)$$

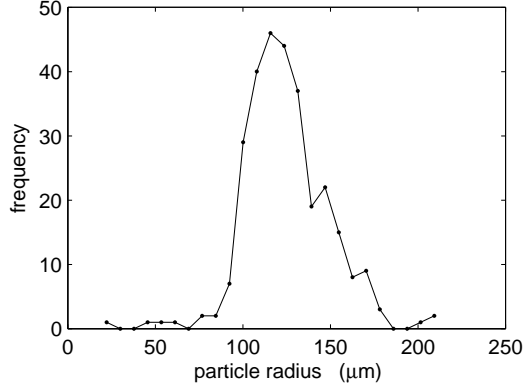


Figure 3.3: Particle size distribution determined from transmission light microscopy images.

The density of copper is $\rho_{\text{Cu}} \approx 8.92 \cdot 10^3 \text{ kg/m}^3$ [11], and the density of acrylic is $\rho_{\text{acrylic}} \approx 1.19 \cdot 10^3 \text{ kg/m}^3$, as measured by Archimedes principle using a solid piece of pure acrylic. The measured weights and calculated copper volume fractions are listed for all samples in Tab. 3.1. The deviations of the measured copper volume fractions from the target volume fractions ϕ_{nom} are a consequence of the demixing discussed above. For simplicity we will refer to the individual samples by their target volume fractions in the following, hence the subscript in ϕ_{nom} standing for “nominal”.

The copper acrylic composites exhibit an extremely high electrical resistance, see Tab. 3.1. For this measurement the small copper-acrylic cylinders were contacted at both front faces by copper plates and wired to the instrument. To ensure proper contact between the small cylinders and the copper plates, a thin layer of Ag paste (G 3303A, Plano GmbH) was painted to them before clamping between the copper plates. The resistance was measured directly with a measurement bridge (PM334, Mastech). The error due to the resistance of the cables and contacts is negligible since the absolute resistance of the samples is very high. The samples with nominal copper

ϕ_{nom} (vol%)	40	45	50	55	60
m (g)	1.590	1.67	1.78	1.89	1.99
ϕ_{Cu} (vol%)	42.8	45.8	49.6	53.6	57.3
R (Ω)	$20 \cdot 10^6$	$20 \cdot 10^6$	$20 \cdot 10^6$	$1.5 \cdot 10^4$	$1 \cdot 10^3$

Table 3.1: Results of physical measurements of CA51 cylinders.

load of 40, 45 and 50 vol% had a resistance in excess of 20 M Ω , the upper measurement limit of the bridge. The sample at 55 vol% showed a resistance of 15 k Ω and the one at 60 vol% showed a value of 1 k Ω . This is a rather unexpected result and we briefly explain how it can be understood.

Fig. 3.4 was taken by light microscopy from the mixed powders. The acrylic particles stick to the surface of the copper particle, presumably due to electrostatic attraction. Thus in uncompressed state most copper particles will be separated by acrylic particles. Upon hot pressing the copper particles are brought closer together, however, as soon as molten acrylic is present the particle surfaces will be wetted. Apparently the wetting angle is so small that by capillary action the melt even separates copper particles initially in contact by a thin insulating layer. Hence electrically conducting contacts between the copper particles are destroyed. Only for very high copper load the copper particles in contact are pressed together strong enough to prevent the acrylic melt from creeping in between. This explains the extraordinarily high threshold of the copper volume fraction separating insulating from conducting effective behavior observed for these composites.

3.2.2 Imaging of samples

All five lathed cylinders were imaged by x-ray computer tomography with an industrial computer tomograph located at EMPA Dübendorf, Switzerland. The polychromatic x-ray beam was generated from a tungsten target hit by an electron beam of 0.08 mA at 158 kV. The source size was measured to be about 15 μ m. Transmission images were recorded with a CCD camera (Flatpanel C7942 CA-02, Hamamatsu) after a filter of 0.6 mm of brass. The scan was done at 600 angles spaced by 0.6°, each frame was reduced to 560 \times 560 pixels by 4 \times 4 binning. The reconstruction was done by filtered backprojection for cone beam after Feldkamp [12]. The reconstructed three-dimensional (3d) images consist of stacks of 560 images each with 560 \times 560 pixels of 16-bit unsigned integers. The pixel size is 10 μ m. The images in the stacks are spaced by a distance exactly equal to the pixel size. This resolution is not sufficient to image thin insulating layers of acrylic between adjacent copper particles. Hence the acquired tomographies cannot represent the real microstructure of the composites.

The contrast in the 3d images from x-ray computed tomography is due to the different attenuation of x-rays in copper and acrylic. At a photon energy of 50 kV the attenuation coefficient of dense copper is about hundred times larger than for dense acrylic. X-rays travelling through a lot of copper have a lower intensity than such traveling largely through acrylic. Consequently in the images acquired by the CCD camera the copper phase is represented by dark pixels. It is, however, customary to invert the contrast, mimicking

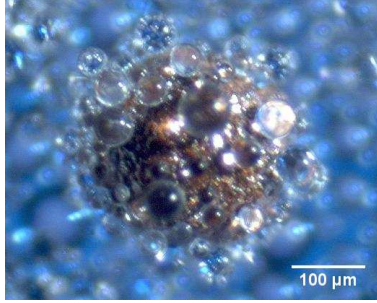


Figure 3.4: Light microscopy image of loose mixture of copper particles with acrylic resin powder showing a copper particle with acrylic resin particles sticking to the surface of it.

the images obtained when using photographic films. Thus regions with high attenuation are represented by bright voxels and such with low attenuation by dark voxels. In all subsequent images the bright voxels correspond to the copper phase and the dark voxels represent the polymer phase. Even if no x-rays are incident on the CCD camera some pixels record a non zero signal, this is the intrinsic noise of the device due to charge fluctuations. Therefore all images contain a superimposed noise signal in form of random fluctuations of the gray level at every voxel.

3.3 Image processing

The creation of the binary images, representing the model microstructures consists of three steps. First the tomographies are cropped and smoothed. Then they are segmented, i.e., a phase is attributed to each voxel. Finally artifacts are removed and the relevant part of the conducting phase, i.e., the percolating cluster is extracted. All image processing was done using the free software ImageJ [10]. The 3d image filters applied are contained in the VTK plugin [13, 14].

3.3.1 Processing of raw image data

First all images were converted to 8-bit format for further processing. Then cubes of 340^3 voxels, corresponding to a volume of 3.4^3 mm^3 , were cropped from the full images such that the distortions occurring at the borders were left outside of the cubes. These cubes were the starting data for all subsequent image enhancement steps. In order to have similar gray level

gradients in all images the brightness and contrast was adjusted in all images to fill the whole gray level range from 0 to 255. Then the images were smoothed in two steps: first by anisotropic diffusion and second by median filtering. The anisotropic diffusion [15] was applied with a diffusion factor of one voxel, diffusion threshold of 40, magnitude gradient threshold on, i.e., each neighbor is examined independently. The number of iterations was set to three. With these parameters all image regions but those containing boundaries between the copper and the polymer phase were smoothed. To reduce the jaggedness of these boundaries a median filter with kernel size of $3 \times 3 \times 3$ voxels was applied. Fig. 3.5 shows slice number 170 from the image cube of the sample with a nominal copper load of 45 vol%. Image (a) shows the the original image and (b) the smoothed one.

3.3.2 Segmentation of smoothed gray level images

In order to attribute a phase to each voxel, thresholding of the smoothed gray level images was performed. The measured volume fraction of copper, see Tab. 3.1, served as criterion for the placement of the threshold value. Threshold values were computed individually for every gray level 3d image. For each image the gray level histogram was generated and stored in form of a text file. A MATLAB script, described below, was used to process these histograms and to compute the threshold for each image. The bright voxels in the images represent the copper phase, thus the script starts at gray level 255 then sums level by level the frequency of smaller gray levels until the first gray level g is reached upon which the sum exceeds the measured volume fraction of copper. The gray level range attributed to the copper phase is then chosen to be from $g+1$ up to 255, yielding a minute deficiency of voxels attributed to the copper phase. As an example the gray level histogram of the image of the sample at 45 vol% is shown in Fig. 3.6. The threshold is indicated by an asterisk. The outliers of the gray level frequency are due to the adjustment of brightness and contrast.

After thresholding binary images which represent the copper and the acrylic phase are obtained. Fig. 3.7 shows a three-dimensional visualization of a small part of the image derived from the tomography of the sample with a nominal copper load of 50 vol%. The surface of the copper phase is represented by a mesh and rendered for perspective view including shadows and reflections. The visualization shows that the copper phase consists of a network of spherical particles with particle-particle contacts resembling sinter-necks. These contacts are due to the limited resolution of the x-ray tomographies. Note that the shown volume covers only about 2 % of the total image volume.

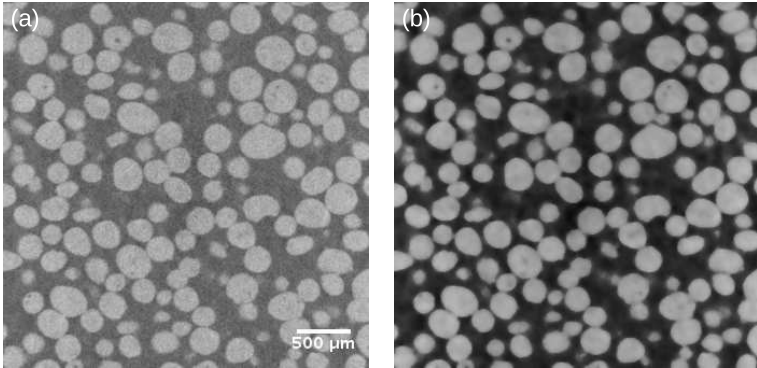


Figure 3.5: Slice 170 of tomography of sample with nominal copper load of 45 vol%. The bright pixels represent the copper and the dark pixels represent the acrylic phase: (a) no smoothing applied and (b) after adjusting the brightness and contrast and application of anisotropic diffusion and median filtering.

3.3.3 Extraction of percolating cluster and removal of small cavities

The binary images obtained after thresholding contain small cavities within the copper phase due to noise in the tomographies. These cavities have to be removed. Furthermore we only want to keep the percolating cluster of the networks formed by the copper phase, as isolated islands of the conducting phase are irrelevant for electrical conduction.

The study of clusters in random sets with no spatial correlation is the topic of percolation theory [7]. We briefly recall the definition of a cluster and then explain the main idea of an algorithm that allows to assign a unique label to every cluster in a binary image. We use the cluster labelling for two purposes: extracting the percolating cluster and removing small cavities.

A cluster in a binary image is defined as a set of connected voxels belonging to the same phase. For the cubic lattice underlying the 3d images we consider, there are different notions of connectivity. Here we use 6-connectivity, i.e. two voxels are connected if they share at least one face. Given a binary image we wish to label all clusters sequentially and to know their mass, i.e., the number of voxels each cluster contains. For this purpose a very elegant algorithm was proposed by Hosheen and Koopelman [17]. The basic idea is to scan the backward neighborhood of each voxel in the image and in case a neighboring voxel belongs to a cluster, to assign the same label to the current voxel. This, however, will not result in a consistent labelling

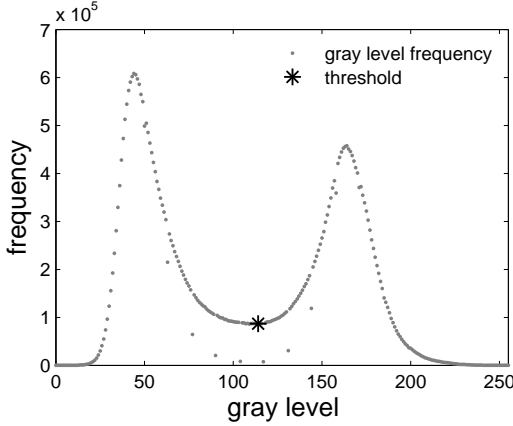


Figure 3.6: Gray level histogram for sample with nominal copper load of 45 vol%. The location of the threshold used for segmentation is indicated by an asterisk.

of clusters. To cope with this problem a list with “good and bad labels” is used. In [7] a concise explanation of this trick can be found. After the whole image has been scanned a list with a unique label for each cluster and its mass can be constructed.

A cluster in a 3d image is called percolating if it connects to all six faces of the image. This property is mandatory for transport through a conducting network embedded in an insulating environment. Therefore we wish to retain only the percolating cluster of the copper phase in our binary images. After all copper clusters are labeled, all faces of the image are scanned. For all faces a list containing the cluster labels occurring in it is generated. Clusters spanning the x-direction are identified by those labels which occur in the lists of the two faces that are perpendicular to the x-direction. Accordingly, clusters spanning the y- and z-direction can be determined. Percolating clusters span all three directions, thus are easily identified as those clusters whose labels occur in all lists. In three dimensional space several percolating clusters can coexist. Regarding effective transport properties we may, however, restrict our attention to the case of a single cluster without loss of generality.

To remove cavities within the copper phase the binary images were inverted and all clusters labeled. The largest cluster represents the acrylic matrix. The remaining clusters are cavities in copper particles which are to be removed. After inverting the images again the white voxels represent the percolating clusters made up by spherical particles with no cavities.

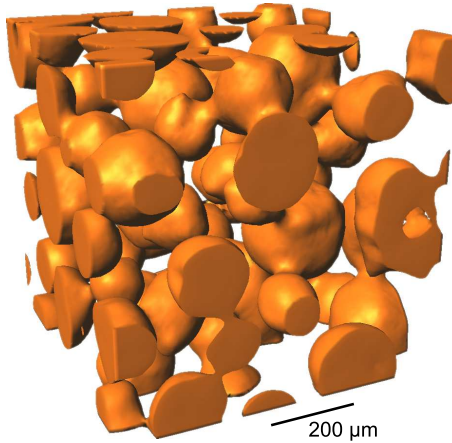


Figure 3.7: Visualization of a small part of the three-dimensional image derived from the tomography of the sample with a nominal copper load of 50 vol%. (Visualization created with Imaris software [16].)

3.4 Estimation of effective conductivity

Based on the binary images that represent the model microstructures the effective conductivity is estimated by a random walk technique.

In principle the effective conductivity of a metal-insulator composite can be computed from the microstructure by solving a boundary value problem based on the Laplace equation as described in Chp. 2. The differential equation itself is simple, however, the complexity of the boundary conditions inhibits analytical solution. Numerical solution of the problem by the finite element method is computationally too expensive for the present microstructures. We therefore resort to a random walk technique based on ideas reported by Laso [18]. The theoretical background for this approach is described in App. A. The random walks are performed directly on the binary images, i.e., the step size is equal to the voxel size, namely 10 μm. It is mandatory that these binary images contain only the percolating cluster of the conducting phase, else the program may fail to terminate. The details of the algorithm we have used are summarized in App. A.4. With this random walk method estimates $\langle \sigma_e^* \rangle_\alpha$ of the unidirectional normalized effective conductivity for the three directions $\alpha = x, y, z$ defined by the face normals of the image cubes are obtained. For a cube completely filled by the conducting phase the normalized effective conductivity is one. We set the z-direction to be parallel to the axis of the cylinder of the samples that served as template to create the model microstructures. We denote by $\langle \sigma_e^* \rangle$

the mean of the three unidirectional estimates.

We performed simulations with 10^4 to 10^8 random walks for each binary image. The effective conductivities obtained from 10^6 and 10^8 random walks agree better than 8 %. This indicates sufficient convergence of the estimates.

Note that the method used overestimates the influence of scattering at the boundaries of the metal phase. The mean free path of electrons in copper at room temperature is about 40 nm as computed using the Drude model with bulk conductivity, Fermi velocity and density of free electrons as input [19]. Thus the step of the simulated random walks is at least two orders of magnitude too large. Resampling the images with higher resolution prior to simulation of random walks implies a strong increase of computational cost and hence is discarded.

3.5 Characterization of microstructures

We summarize the methods used to determine microstructural quantities from the binary images representing the model microstructures. Theoretical background on the applied techniques can be found in App. B.

3.5.1 Betti numbers

The Betti numbers in three-dimensional space are the number of components b_0 , the number of loops (tunnels or handles) b_1 and the number of cavities b_2 of a set. Note that these quantities are dimensionless and invariant under continuous deformations of the set: they are topological rather than geometrical quantities. The alternating sum of the Betti numbers is the well known Euler characteristic χ . Hence the Betti numbers contain more information of a set than the Euler characteristic alone.

A practical way of determining the first and third Betti number is by labeling of clusters, see Sec. 3.3.3. White voxels sharing a face are considered connected, consequently black voxels sharing either a face, an edge or a vertex must be considered connected for consistency reasons [20]. The number of 6-connected clusters in the image is b_0 . The number of 26-connected clusters in the inverted image is $b_2 + 1$. Given the first and third Betti number, the second Betti number can be computed from the Euler characteristic [20], namely by

$$b_1 = b_0 - \chi + b_2. \quad (3.2)$$

Note that this implies that the 6-connected Euler characteristic must be used. The basic algorithm to compute the Euler characteristic relies on analyzing the neighborhood of every voxel and then to contract the corresponding histogram with certain weights [21]. We have modified the vector used for the

contraction in order to obtain exactly the 6-connected Euler characteristic, see App. B.2.

3.5.2 Number of particles

The networks in our binary images consist of particles in contact, see Fig. 3.2. In order to count the number of particles N that form a percolating cluster it is necessary to cut all contacts. This separation of the individual particles can be achieved by appropriately eroding the structure. The strength of the erosion must be chosen such that all particles are separated but the smaller ones are not yet annihilated. Once the particles are separated they are counted easily by computing the first Betti number.

3.5.3 Number of contacts

The number of contacts C in a network formed by N spherical particles in contact can be obtained from its Betti numbers, namely

$$C = N - b_0 + b_1. \quad (3.3)$$

To see why this holds consider N spherical particles forming a long chain as shown in Fig. 3.8(a). The number of contacts is one less than the number of particles. Since the chain forms one component we have $C = N - b_0$. This expression remains true even if we separate the long chain into several short ones, as shown in Fig. 3.8(b). The situation becomes interesting when the chain is deformed and further contacts between particles are established. Each new contact will introduce a loop, hence increase the value of b_1 by one, see Fig. 3.8(c). Therefore Eq. (3.3) holds for the case of any network formed by N spherical particles. The requirement of having spherical particles guarantees that neither cavities nor gap-less agglomerates can be formed by the particles.

3.5.4 Critical radii

Erosion with progressively larger structuring elements allows reducing step-wise the width of all structures in a binary image. In the case of our networks at some point percolation breaks down, i.e., there is no path within the network that connects to all six faces of the image. Since wider contacts can withstand stronger erosions there is a critical radius of contacts r_c^ε in the sense that percolation breaks down if all contacts with radius $r \leq r_c^\varepsilon$ are removed. An algorithm to compute the critical radius of contacts is based on extracting of the percolating cluster for progressively eroded sets. The

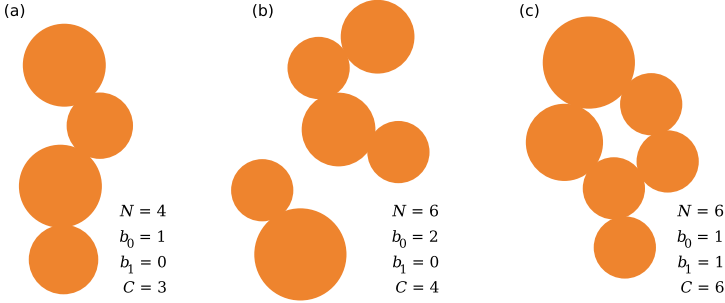


Figure 3.8: Illustration of argument to compute the number of contacts C from the number of particles N and the first two Betti numbers b_0 and b_1 . Three cases are show: (a) single chain, (b) several chains, (c) arbitrary network including loops.

critical radius of contacts is defined by

$$r_c^\varepsilon = \min \{r \mid \text{PC}(\varepsilon_{b_r} X) = \emptyset\}, \quad (3.4)$$

where X denotes the network of particles, ε_{b_r} is the erosion with a ball of radius r , and PC denotes extraction of the percolating cluster.

Opening with progressively larger structuring elements removes stepwise larger and larger particles from a structure. Similarly as with the erosion, at some point percolation of the network breaks down. The critical radius of particles is defined by

$$r_c^\circ = \min \{r \mid \text{PC}(\circ_{b_r} X) = \emptyset\}, \quad (3.5)$$

where \circ_{b_r} denotes opening by a ball of radius r . If all particles with radius $r \leq r_c^\circ$ are removed from the network, it doesn't percolate any more.

3.6 Results and discussion

All results presented below were obtained from five binary images representing model metal-insulator microstructures, namely percolating networks of a conducting phase consisting of spherical particles with contacts resembling sinter-necks. The volume fraction of the percolating networks is denoted by ϕ_{PC} . The cubic images contain 340^3 cubic voxels representing a volume of $(3.4 \text{ mm})^3$.

The estimates of the unidirectional normalized effective conductivities $\langle \sigma_e^* \rangle_\alpha$ ($\alpha = x, y, z$) versus the volume fraction of the percolating network are

shown in Fig. 3.9 by open markers. The variation of the results obtained from different runs of the random walk based simulation is very small, therefore no error bars are shown. Apparently there is a significant anisotropy in the effective conductivity: the value belonging to the z-direction is offset. Interestingly this axis is parallel to the pressing direction during preparation of the samples used as templates for creating the binary images. Within the xy-plane the conductivity appears to be isotropic.

The mean of the three unidirectional normalized effective conductivities $\langle\sigma_e^*\rangle$ is shown by dots connected with solid lines in Fig. 3.9. Note that this normalized effective conductivity rises in excess of the change of the volume fraction: ϕ_{PC} ranges over a factor of 1.5, whereas the effective conductivity covers a factor of 4. This indicates that the networks at high volume fractions are more effective for conduction, i.e., the conducting phase sustains a higher current density.

Tab. 3.2 summarizes the microstructural characteristics determined from the binary images. The volume fraction of the percolating network ϕ_{PC} is only slightly smaller than that of the copper phase in the samples used as templates to create the model microstructures ϕ_{Cu} , see Tab. 3.1. The estimated number of particles N is in good agreement with the mean particle radius $\langle r \rangle$, see Sec. 3.2.1, and the volume fraction of the percolating network ϕ_{PC} , namely $4\pi/3 \langle r \rangle^3 N \approx \phi_{\text{PC}} (3.4 \text{ mm})^3$. The number of loops b_1 increases significantly faster than the number of particles with increasing volume fraction. Since the number of loops is a measure of connectivity, this observation indicates that the networks at high volume fraction are “tighter” as compared to those at low volume fractions. This is in qualitative agreement with the strong increase of the effective conductivity with increasing volume fraction shown in Fig. 3.9. The number of contacts $C = N - 1 + b_1$ by construction shows a behavior intermediate to that of the number of particles and the number of loops. Qualitatively the behavior of the number of contacts agrees with the trend of the effective conductivity. Both critical radii increase with

ϕ_{nom} (vol%)	40	45	50	55	60
ϕ_{PC} (vol%)	41.9	45.5	49.6	53.9	57.8
N (-)	1966	2141	2362	2603	2777
b_1 (-)	774	1226	1856	2856	4136
C (-)	2739	3366	4217	5458	6912
r_c^e (μm)	30	40	40	40	50
r_c^o (μm)	70	80	90	100	100

Table 3.2: Volume fraction of percolating cluster and microstructural characteristics: number of loops b_1 , number of particles N

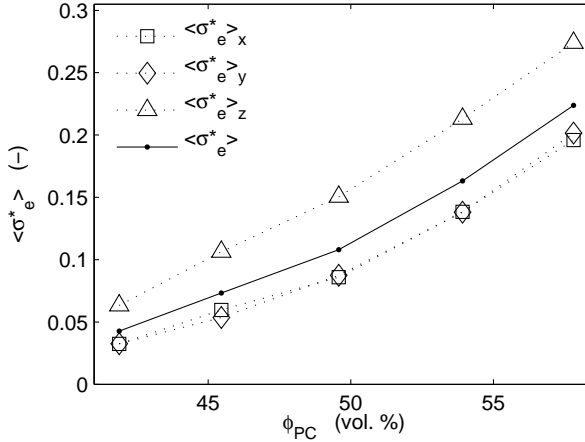


Figure 3.9: Estimated effective conductivity versus volume fraction of percolating cluster ϕ_{PC} . The open markers show the values for conduction in the three directions defined by the face normals of the cubic sample. The mean value is shown with dots and a solid line as guide to the eye.

increasing volume fraction. This means that the networks at higher volume fraction are more robust than those at low volume fractions: the size of contacts (particles) that have to be removed to destroy percolation increases with the volume fraction of the network. Since the particles in all networks have the same size distribution, a plausible explanation for this is that, the higher the volume fraction the more individual paths from one image face to another exist and hence the more likely it is that large particles forming wide contacts form a path that percolates the image. This explanation is in accordance with the observation that the ratio of the critical radii r_c^ε/r_c^o is almost constant.

Next we investigate in how far the above listed microstructural quantities are related to the effective conductivity of the microstructures. Since all considered microstructural quantities are isotropic we compare them to the mean of the estimated unidirectional normalized effective conductivity. Regarding the critical radii, theory suggests that the area of contacts is relevant for the effective conductivity. Therefore we only inspect the squared critical radius of contacts $(r_c^\varepsilon)^2$, as follows below.

Fig. 3.10 shows the ratios of the mean estimated normalized effective conductivity $\langle \sigma_e^* \rangle$ and three microstructural characteristics: b_1 , C and $(r_c^\varepsilon)^2$. Apparently the number of loops b_1 is the only quantity that shows a good correlation with the effective conductivity. The ratio $\langle \sigma_e^* \rangle/b_1$ is constant

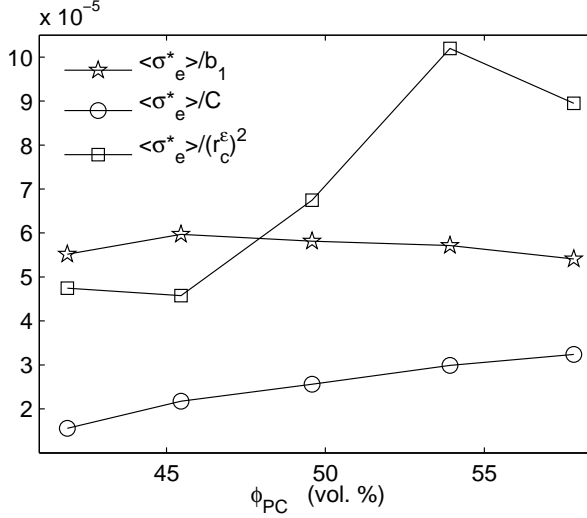


Figure 3.10: Correlation of the mean effective conductivity $\langle \sigma_e^* \rangle$ with microstructural characteristics. Ratios of the conductivity and the number of loops b_1 , the number of contacts C and the area of the critical contact $(r_c^e)^2$ are respectively shown versus the volume fraction of the percolating cluster ϕ_{PC} .

within an error of about 4 %: its mean value is 5.7×10^{-5} and the standard variation is 2.25×10^{-6} . The ratio $\langle \sigma_e^* \rangle / C$ increases monotonously with increasing volume fraction, this indicates poor correlation, as is also reflected by the ratio of the standard deviation to the mean value, namely $2.5 \times 10^{-5} / 6.7 \times 10^{-6} \approx 26.6\%$. There appears to be no correlation with the area of the critical contact. This is surely a consequence of the many different paths that are present in the studied networks. It is expected that the correlation becomes better for lower volume fraction of the percolating cluster, i.e., close to the percolation threshold.

3.7 Conclusions and outlook

A good correlation of the effective conductivity and a microstructural characteristic, namely the number of loops, was shown for a sequence of five model metal-insulator microstructures with varying volume fraction of the conducting phase. The conducting phase of all microstructures is composed of the same kind of spherical particles. These form percolating networks

through particle-particle connections resembling sinter-necks. Since the effective conductivity rises disproportionately to the volume fraction, the variation of the volume fraction necessarily triggers a variation of the connectivity of the networks. We conclude that the effective conductivity of the studied microstructures is determined by the way the particles forming the networks are connected rather than by the number of particles present in the network. This is corroborated by the observation that neither the number of particle-particle contacts nor the minimal cross section area of the critical path through the network show a good correlation with the effective conductivity. We remark that the product of the the mean area of contacts with the number of contacts, i.e., $2\pi(r_c^\varepsilon)^2 C$, also yields a fairly good correlation with the estimated effective conductivity. This and other combinations of microstructural characteristics would surely be worth a thorough investigation.

For networks close to the percolation threshold the cross section area and the length of the critical contact, also known as red bond, determines the effective conductivity. It would be interesting to investigate microstructures covering the range of volume fraction from the percolation threshold up to virtually dense structures using the approach of this study. This would allow to study the cross-over from the regime of the effective conductivity determined by the geometry of the red bond to the regime dominated by the number of loops. Another interesting extension of the here studied microstructures would be to vary the connectivity of the networks while keeping a fixed volume fraction. Possibly such microstructures could be derived from tomographies of template samples made from copper particles with different size distributions. In addition completely synthetic microstructures, i.e., such generated by random set models, could be studied as well.

For the case of finite phase contrast, i.e., a mixture of a good and a bad conductor, it was shown by Heggli that tomographies allow to compute the effective conductivity in good agreement with the measured value [22]. The case of metal-insulator microstructures, i.e., infinite phase contrast, is much more delicate since fine details concerning connectivity may discriminate between insulating and conducting effective behavior. The random walk technique we used to estimate the effective conductivity of the microstructures allows to study the relation between microstructure and effective conductivity without the need for physical measurements on real samples. The computational effort of the random walk technique is between the high cost of the finite element method and the very easily computable microstructural characteristics. Thus the random walk approach allows to study larger data sets as compared to studies based on the finite element method. This is of particular importance when studying networks close to the percolation threshold since there the size of the representative volume element diverges.

Acknowledgments

The author would like to thank Niklaus Koch from the workshop of the materials department of ETH Zurich for shaping small cylinders from the sensitive composite samples. Peter Wyss from Empa is acknowledged for carrying out the tomography scans and reconstructions. The estimation of the effective conductivity using random walk techniques was suggested by Prof. Andrei Gusev from the polymer physics group at ETH Zurich. We are grateful to Prof. Hans-Christian Öttinger, also from the polymer physics group, for his ingenious advice leading to the random walk approach we finally used.

Bibliography

- [1] H. J. Vogel, “Morphological determination of pore connectivity as a function of pore size using serial sections,” *Eur. J. Soil Sci.*, vol. 48, pp. 365–377, 1997.
- [2] C. H. Arns, *The influence of morphology on physical properties of reservoir rocks*. PhD thesis, School of Petroleum Engineering, The University of New South Wales, 2002.
- [3] J. R. Wilson, W. Kobsiriphat, mendoza R., H.-Y. Chen, J. M. Hiller, D. J. Miller, K. Thornton, P. W. Voorhees, S. B. Adler, and S. A. Barnett, “Three-dimensional reconstruction of a solid-oxide fuel-cell anode,” *Nat. Mater.*, vol. 5, pp. 541–544, 2006.
- [4] A. Berson, H.-W. Choi, and J. G. Pharoah, “Determination of the effective gas diffusivity of a porous composite medium from the three-dimensional reconstruction of its microstructure,” *Phys. Rev. E*, vol. 83, p. 026310, 2011.
- [5] D. Cioranescu and P. Donato, *An introduction to homogenization*. Oxford University Press, 1999.
- [6] D. S. McLachlan, M. Blaskiewicz, and R. E. Newnham, “Electrical resistivity of composites,” *J. Am. Ceram. Soc.*, vol. 73, no. 8, pp. 2187–2203, 1990.
- [7] D. Stauffer and A. Aharony, *Introduction to Percolation Theory*. Boca Raton: CRC Press, 1994.
- [8] S. Torquato, *Random heterogeneous materials : microstructure and macroscopic properties*. Springer, 2002.

- [9] G. M. Milton, *The theory of composites*. Cambridge monographs on applied and computational mathematics ; 6, Cambridge University Press, 2002.
- [10] W. S. Rasbad, “Imagej.” U. S. National Institutes of Health, Bethesda, Maryland, USA, <http://imagej.nih.gov/ij/>, 1997-2011.
- [11] N. N. Greenwood and A. Earnshaw, *Chemie der Elemente*. VCH, 1988.
- [12] L. A. Feldkamp, L. C. Davis, and J. W. Kress, “Practical cone-beam algorithm,” *J. Opt. Soc. Am. A*, vol. 1, no. 6, pp. 612–619, 1984.
- [13] W. Schroeder, K. Martin, and B. Lorensen, *The visualization toolkit: an object-oriented approach to 3D graphics*. Kitware, 2006.
- [14] <http://ij-plugins.sourceforge.net/ij-vtk/index.html>.
- [15] P. Perona and J. Malik, “Scale-space and edge detection using anisotropic diffusion,” in *Proceedings of IEEE Computer Society Workshop on Computer Vision*, pp. 16–22, 1987.
- [16] <http://www.imaris.com/>.
- [17] J. Hoshen and R. Kopelman, “Percolation and cluster distribution. i. cluster multiple labelling technique and critical concentration algorithm,” *Phys. Rev. B*, vol. 14, pp. 3438–3445, 1976.
- [18] M. Laso, “Stochastic dynamic approach to transport phenomena,” *AlChE J.*, vol. 40, pp. 1297–1311, 1994.
- [19] C. R. Nave, “Hyperphysics.” Department of Physics and Astronomy, Georgia State University, <http://hyperphysics.phy-astr.gsu.edu/hbase/electric/ohmmic.html>. online, accessed August 23, 2011.
- [20] P. Soille, *Morphological image analysis: principles and applications*. Springer, 2nd edition ed., 2004.
- [21] J. Ohser and F. Mücklich, *Statistical Analysis of Microstructures in Materials Science*. John Wiley & Sons, Ltd., 2000.
- [22] M. Heggli, T. Etter, P. Wyss, P. J. Uggowitzer, and A. A. Gusev, “Approaching representative volume element size in interpenetrating phase composites,” *Adv. Eng. Mater.*, vol. 7, pp. 225–229, 2005.

Chapter 4

Simulation of electrical conduction in a micro-solid oxide fuel cell chip

Abstract

Miniaturized solid oxide fuel cells (micro-SOFCs) integrated on a chip are potential candidates to replace Li-ion batteries in portable power systems. We focus on the current collector used to connect in parallel individual electrochemical fuel cells on a silicon single crystal chip substrate. Simulation of the electrostatics of the current collector is used to determine its effective resistance. Furthermore the total power output of the chip when all cells operate in parallel is determined employing a linear model for the cell losses. The maximum power delivered by individual cells is varied from state of the art micro-SOFCs up to two orders of magnitude higher. The current collector limits the total power output by promoting interaction between the individual cells in the chip. The more power can be delivered by one cell, the more the cells in the array hinder each other and the chip fails to deliver the theoretically possible power. The presented method to investigate the influence of the geometry of the current collector on chip performance is a valuable tool for optimizing future micro-SOFC devices.

4.1 Introduction

The increasing power demands for portable electronic devices have led to optimization of Li ion batteries in the last decade. For future portable devices however, yet higher energy density and faster recharge is demanded as well as geographical independence from a power grid. As Li ion technology has limited improvement potential, new technologies are being considered [1]. Particularly promising are miniaturized fuel cells. A great benefit that would come with this technology is the virtually instantaneous recharging by simple replacing of the empty fuel tank with a full one. Amongst the different types of fuel cells in development, solid oxide fuel cells (SOFCs) offer the advantage of being able to run on hydrocarbons, e.g. liquid pressurized gas with a high energy density with respect to weight and volume. Conventional solid oxide fuel cells operate at a temperature above 800°C and are on the scale of power plants providing electrical power in the kW to MW range. For such systems high power densities up to 1 kW/kg and 800 W/\ell with respect to the whole fuel cell system are achieved [2]. The electrochemical parts of conventional SOFCs consist of an electrolyte with a thickness of some 100 to $250\text{ }\mu\text{m}$ and electrodes on either side. This membrane electrode assembly (MEA) is typically produced by conventional ceramics technology, such as tape casting and screen printing [3]. Both the electrochemical activity of the electrodes and the ionic conductivity of the solid electrolyte are thermally activated. If a SOFC shall be operated at much lower temperature the slow down of kinetics must be compensated by thinning of the electrolyte and increasing the porous electrode internal surface area by employing extremely fine grained material nanostructures. This approach has been pursued in the last years with appreciable success [4]. The basic idea for producing micro-SOFCs is to employ techniques used for processing of microelectromechanical systems (MEMS). One of the key achievements is the preparation of extremely thin free standing solid electrolyte membranes [5]. The macroscopic mechanical support of the electrochemical active membranes is provided by a microstructured silicon single crystal wafer. The functional ceramic is applied by thin film coating processes. The final electrochemically active cells typically consist of a dense yttria stabilized zirconia thin film sandwiched between two platinum thin films. Each of the three films has a thickness of around 100 nm or less. The active area of the cells is some hundred by hundred micrometers large. Several groups conduct research on such micro-SOFCs. The reported power density, as well as the operating temperature of micro-SOFCs vary depending on the membrane properties and preparation technologies [6, 7, 8, 9, 10]. On average a power density of 200 mW/cm^2 at a cell voltage of 0.4 V is achieved at present when operating the cell around 400°C . The low cell voltage is due to the relatively large overpotential loss

at low operating temperature as compared to conventional SOFCs, which typically yield maximal power at 0.7 V.

For most applications a voltage of 0.4 V is too low, thus several cells must be connected in series to increase the output voltage. To reach a reasonable target power output, say 5 W, it is furthermore necessary to operate cells in parallel since the maximal single cell area is limited. Therefore an actual fuel cell system will consist of a large number of individual fuel cells connected in series and parallel, similarly as in a battery pack [11]. The performance of a multi-cell system depends on the performance of the individual cells. Ideally all cells should have identical electrical properties. It is a problem in its own right to achieve this, but we will not be concerned with this issue here.

We investigate a particular layout of a chip integrating 30 individual micro-SOFCs each with an active area of $200 \times 200 \mu\text{m}^2$ and identical current voltage characteristics. The anodes of the cells are connected by a planar current collector. The layout is detailed in Sec. 4.2.

Our investigation concerns two distinct aspects of the current collector:

1. We determine the effective resistance of the current collector for a current from the site of an individual cell to a current sink. This resistance is simply due to the finite conductivity of the current collector and depends on the location of the current source, as well as the geometry of the current sink. The effective resistance of the current collector is compared to the intrinsic losses occurring within a cell when operated at the working point yielding maximal power output.
2. We investigate the behavior of the chip when all cells operate in parallel. This case requires modeling the current voltage characteristic for each individual cell. The current collector couples the voltages of the individual cells and thus modulates the current delivered by the cells according to their position and the current voltage characteristic. The total power output of the chip is studied as a function of two parameters, namely the power delivered by an individual cell when operated alone and the thickness of the platinum thin film current collector. This addresses the question, whether the parallel operation of the cells in the chip results in the theoretically possible power output, namely the product of the number of cells and the maximal power one cell can deliver. The answer is shown to depend mainly on the geometry of the current sink. Furthermore both the power delivered by the individual cells as well as the thickness of the thin film current collector play a role.

4.2 Simulation of electrostatics

The layout of the chip considered is shown in Fig. 4.1(a) and (b). The lateral extension of the chip is $23 \times 23 \text{ mm}^2$ and the thickness is $500 \text{ }\mu\text{m}$. Two different types of connection to outer circuitry are considered: Either by contacting the whole boundary of the chip, called ring sink (RS) or by a wire bonded to the current collector in one corner of the chip, called wire sink (WS). The chip is based on a Si_3N_4 coated Si wafer structured by photolithography and wet etching. Holes with the shape of truncated pyramids go through the wafer and end at the individual fuel cells, see Fig. 4.1(b). The angle of 54.7° between the walls of the hole and the wafer surface is typical for KOH etching. The base area of the holes is $910 \times 910 \text{ }\mu\text{m}^2$, leading to an area of $200 \times 200 \text{ }\mu\text{m}^2$ at the individual fuel cells. Only the free standing area of the fuel cells is electrochemically active since adjacency to the gas phase is mandatory for fuel cell operation. The whole chip area on the side

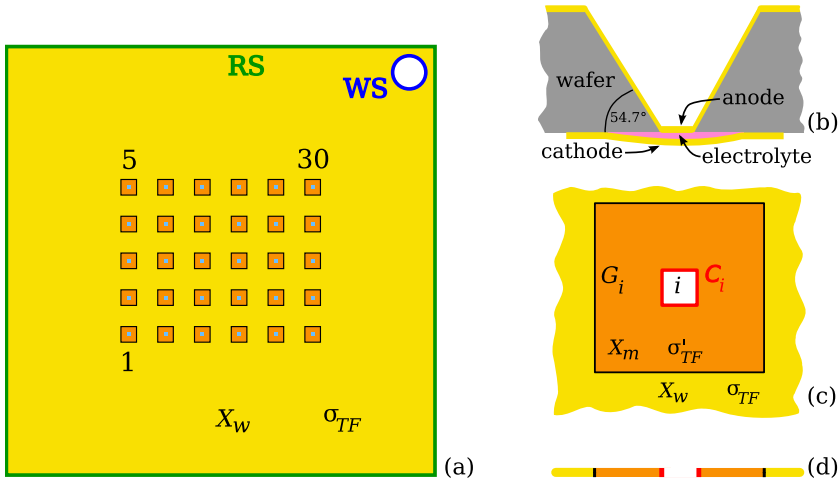


Figure 4.1: Layout of micro-SOFC chip. (a) Overview from anode side: cells are labeled 1 to 30. The wire current sink (WS) is shown in dark blue, the ring current sink (RS) in green. (b) Cross section view at one of the cells showing the electrolyte sandwiched between the electrodes. (c) Detailed view of cell i : its boundary C_i is shown in red, the part of the current collector actually lying in the wafer plane X_w is shown in yellow, the part mapped into the wafer plane X_m in orange and the boundary between these parts G_i is shown in black. (d) Cross section view of planar current collector geometry after mapping.

with the large openings i.e., the anode side, is coated by a chromium layer of 30 nm and a platinum thin film with thickness of 100 nm. This bi-layer thin film serves as current collector. It connects the anodes of all individual cells with the current sink, either WS or RS. This is the negative pole of the chip. The cathodes are connected individually by wires bonded to them and leading to the positive pole of the chip. The power consumer is attached between the two poles. We focus our attention on the current collector on the anode side and neglect effects from the current collection on the cathode side.

We now detail the boundary value problem that describes the electrical current flow from the sources, i.e., the boundaries of the cells C_i to the sink S , i.e., either wire or ring current sink, RS and WS in Fig. 4.1(a) respectively. In principle the current collector is three-dimensional, but since it is very thin compared to its lateral extension we may treat it as a two-dimensional conductor. The advantage of this is the reduction of the complexity of the numerical problem. The three-dimensional specific resistance of bulk platinum at 400 °C is $\rho_{Pt} = 244.6 \text{ n}\Omega\text{m}$ and chromium has a bulk resistivity of $\rho_{Cr} = 282.0 \text{ n}\Omega\text{m}$, as obtained by linear interpolation from the values given in [12]. Thus the 30 nm chromium layer has the same resistance as a 26 nm thin platinum layer. Therefore the chromium-platinum bi-layer is equivalent in terms of resistivity to a platinum thin film of thickness $d = 126 \text{ nm}$. The two-dimensional conductivity, i.e., the inverse of the sheet resistance, of the chromium-platinum thin film is $\sigma_{TF} = \frac{d}{\rho_{Pt}} \approx 0.515 \text{ S}$.

Due to the inclination towards the wafer normal, the platinum thin film in the walls of the etched hole is thinner by a factor of $\cos(54.7^\circ) \approx 0.578$ than that lying in the wafer plane. Furthermore the conductivity is reduced additionally by the fact that agglomeration of the Pt thin film will be more progressed in the thinner film on the tilted walls than on the rest of the current collector [13]. Determining the precise value by which the conductivity is reduced due to this effect requires to image the actual microstructure generated by the thin film agglomeration and to compute the effective conductivity therefrom. For the purpose of the present study we use an estimated value of 0.6 for the factor by which the conductivity of the agglomerated film is reduced as compared to a dense platinum film. Finally we map the 3d structure of the tilted walls of the etched holes to a computationally equivalent 2d structure. We require that the current flowing through the mapped and the tilted walls be the same, if the same voltage drop is applied from inner to outer boundary, i.e. the resistance shall be equal, see Fig. 4.2. For given geometry and potential drop the current can be tuned by scaling the conductivity. Since the geometry is not trivial an analytic expression for the potential is not at hand. Simulation of current flow through the tilted and the mapped walls shows that the conductivity

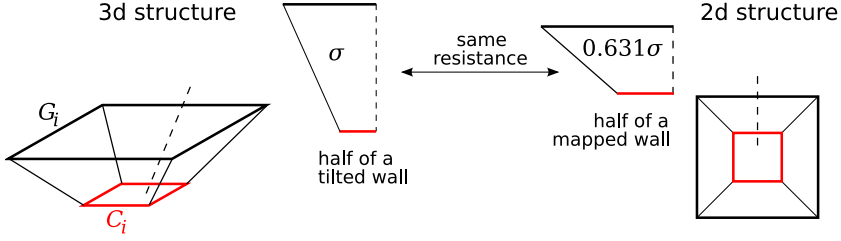


Figure 4.2: Mapping the 3d structure to a 2d structure with equal resistance. The tilted walls are longer than the mapped ones. The 2d conductivity is reduced to compensate the loss of length.

in the mapped wall must be set to 0.631 times the conductivity in the tilted walls to fulfil the above mentioned condition.

Thus in total the conductivity of the mapped regions of the current collector must be attributed a conductivity σ'_{TF} lower by a factor of $\alpha = 0.219$ than the rest of the current collector, where α is the product of the three above mentioned factors. In absolute numbers we thus have $\sigma'_{TF} = \alpha\sigma_{TF} = 0.113S$. Let X denote the planar current collector. We denote the part that actually lies in the wafer plane by X_w and the part mapped to the wafer plane by X_m , thus $X = X_m \cup X_w$. Within X_w the conductivity is given by σ_{TF} , whereas in X_m it is $\sigma'_{TF} = \alpha\sigma_{TF}$, see Fig. 4.1(a) and (c).

The equations describing electrostatics follow from the Maxwell equations [14]. The boundary value problem describing an electrical current going from a source to a sink through a complex two-dimensional geometry is derived in detail in [15]. For the present case, and in the steady state, the electrical potential u within the current collector X is the solution of the following boundary value problem,

$$\begin{aligned}
 \Delta u &= 0, \text{ on } X \\
 u &= U_S, \text{ on } S \\
 \mathbf{n} \cdot \nabla u &= 0, \text{ on } B \\
 \sigma_{TF} \mathbf{n} \cdot \nabla u^+ &= \sigma'_{TF} \mathbf{n} \cdot \nabla u^-, \text{ on } G \\
 u &= U_C, \text{ on } C,
 \end{aligned} \tag{4.1}$$

where S is the current sink, $C = \bigcup_{i \in O} C_i$ specifies the boundaries of operating cells $O \subset \{1, 2, \dots, 30\}$, $B = \partial X \setminus (C \cup S)$ is the insulated part of the boundary of the current collector and $G = \bigcup_{i=1}^{30} G_i$ is the union of the boundaries between the regions with different conductivity within X . We remark that the expression in the second last line can be reduced to $\mathbf{n} \cdot \nabla u^+ = \alpha \mathbf{n} \cdot \nabla u^-$ on G . The meaning of this equation is that the current

density is continuous across the boundary G_i . The vector \mathbf{n} is the normal vector on a given boundary, e.g. G_i here.

The boundary value problem given by Eq. (4.1) can be solved numerically by the finite element method (FEM).

4.2.1 Effective resistance of the current collector

We here only consider the current collector without any fuel cells attached to it. As explained above the current collector is a metallic thin film with shape X . The conductivity is independent from the potential or current density but has a spatial variation. Within X_w the conductivity is $\sigma_{TF} = 0.515 \text{ S}$ and within X_m it has the value $\sigma'_{TF} = 0.113 \text{ S}$. We wish to determine the effective resistance $R_{i,S}$ for a current flowing from a given boundary C_i to a given sink S . Due to its complex shape, however, this resistance cannot be computed analytically. Therefore we perform a simulation of the electrostatics. A constant potential drop $U = |U_{C_i} - U_S| > 0$ applied between the current source C_i and sink S drives a current $I_{i,S}(U)$. The ratio of voltage drop to current is the effective resistance, namely

$$R_{i,S} = \frac{U}{I_{i,S}(U)}. \quad (4.2)$$

The boundary value problem describing this situation is given by Eq. (4.1) with $C = C_i$, $U_C = 1 \text{ V}$, $U_S = 0 \text{ V}$. The choice of the two potentials is arbitrary up to the requirement that their difference U be nonzero. All boundaries of the current collector which are not subject to fixed voltages are insulated. In particular we have $\bigcup_{j \neq i} C_j \subset B$. Let $u_{i,S}$ denote the solution of this boundary value problem. The current $I_{i,S}(U)$ from source C_i to sink S driven by the voltage drop U is given by the flux of current density $\sigma_{TF} \mathbf{n} \cdot \nabla u_{i,S}$ going through the sink S , namely

$$I_{i,S} = \sigma_{TF} \int_S \mathbf{n} \cdot \nabla u_{i,S} \, dl. \quad (4.3)$$

Next we will determine how the effective resistance of the current collector is distributed. The average voltage on the boundary G_i , denoted by $\langle U \rangle_{G_i,S}$ is a measure for the portion of the resistance that is due to X_w , the part of the current collector actually located in the wafer plane. In formulae it reads

$$\langle U \rangle_{G_i,S} = L(G_i)^{-1} \int_{G_i} u_{i,S} \, dl, \quad (4.4)$$

where $L(G_i)$ is the length of boundary G_i .

The relevant potentials and the setup considered in this section are summarized in Fig. 4.3. This setup corresponds to a short circuited chip in

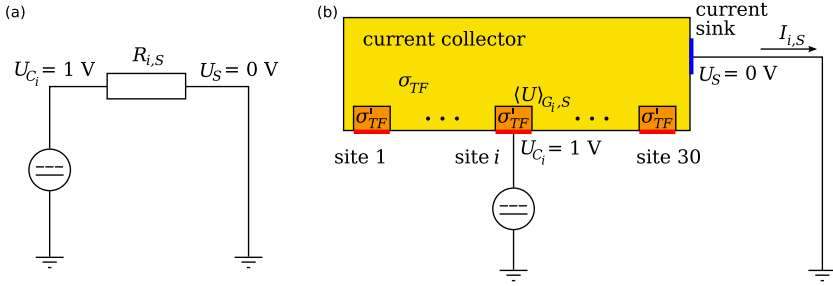


Figure 4.3: (a) Circuit diagram corresponding to the simulation of the effective resistance of the current collector. (b) Detailed schematic of setup used to determine the effective resistance of the current collector for current flowing from site i to sink S . The colors code the relevant components of the current collector, see also Fig. 4.1.

which only one fuel cell, modeled as ideal voltage source, is operated while all others are inactive. The inactive cells have no contact attached to the cathode side. If several sites were connected to ideal voltage sources one may think that this represents parallel operation of these cells. However, the fixed potential of the cells close to the current sink acts like a barrier for the current from cells located more remotely from the current sink. It is therefore not possible to simulate operation of all fuel cells with the model used to determine the effective resistance of the current collector. In the next section we describe how to model the voltage at the cell boundaries more appropriately.

4.2.2 Total power output of the chip

We now wish to investigate the electrostatics of the current collector when fuel cells are connected to it. We start by recalling the facts from electrochemistry relevant to understanding of the current voltage characteristic of fuel cells. Then we describe the model that we employ to simulate fuel cells attached to the current collector. This model can describe the current-voltage characteristic around a certain working point to which it has been tuned. The calibration of the model is done by simulating operation of a single cell in the chip. After the calibration parallel operation of all cells in the chip can be simulated around the chosen working point.

The maximum voltage a fuel cell generates is called open circuit voltage (OCV), it is about 1.2 V at an operating temperature of $400\text{ }^\circ\text{C}$. The OCV is given by the thermodynamics of the underlying chemical reaction, namely $\text{H}_2 + \frac{1}{2}\text{O}_2 \rightleftharpoons \text{H}_2\text{O}$, and the corresponding Nernst equation [2]. According to

the Butler-Volmer equation, voltage has to be sacrificed in order to generate a finite current from an electrochemical reaction. This voltage drop is known as overpotential, it is an intrinsic loss of a fuel cell. Another voltage drop is due to the ohmic resistance the ion current experiences when flowing through the electrolyte. These voltage drops taken together are referred to as cell losses. They are a nonlinear function of the current that flows. A typical current voltage characteristic of a micro-SOFC is shown in Fig. 4.4.

To model the current voltage characteristics of the fuel cells in the chip one could in principle apply a self-consistent boundary condition in Eq. (4.1), namely $U_{C_i} = OCV - f(I_{C_i})$, where $I_{C_i} = \sigma'_{TF} \int_{C_i} \mathbf{n} \cdot \nabla u dl$ is the current from cell i and $f(I_{C_i})$ specifies the cell losses as function of the current. To simplify this complicated boundary condition, we apply a trick similar to the one used in [16]. The current voltage characteristic is linearized in order to allow modeling of the cell losses by an ohmic resistance located right at the boundary of the fuel cell. For this purpose small frames are joined to each fuel cell boundary. Within all these small frames X_{CL} the conductivity is σ_{CL} , see Fig. 4.5. The inner boundary H_i of the frame located at cell i is subject to a constant potential U_H . The outer boundary C_i of the frame is subject to the condition that the normal component of the current is continuous. In formulae these two boundary conditions read

$$\begin{aligned} \sigma'_{TF} \mathbf{n} \cdot \nabla u^+ &= \sigma_{CL} \mathbf{n} \cdot \nabla u^-, \text{ on } C \\ u &= U_H, \text{ on } H, \end{aligned} \quad (4.5)$$

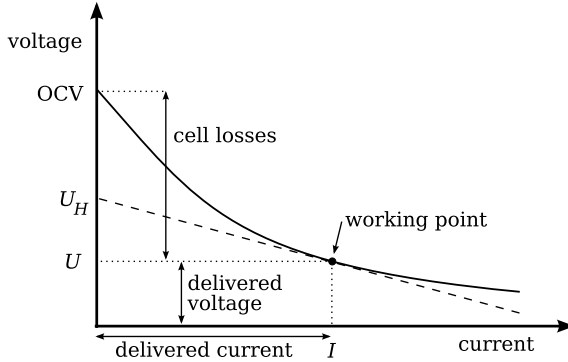


Figure 4.4: Schematic of typical micro-SOFC current voltage characteristic (solid line). The dashed line indicates the linearized current voltage characteristic fitting the indicated working point (I, U) . U_H is the y-axis intercept of the linearized curve, whereas OCV is the open circuit voltage of the fuel cell.

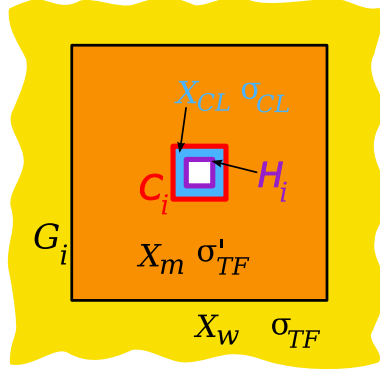


Figure 4.5: Detailed geometry at cell site i including region X_{CL} , shown in light blue, and its inner boundary H_i , shown in purple. These small frames are used to model cell losses.

where $H = \bigcup_{i \in O} H_i$ and $O \subset \{1, 2, \dots, 30\}$ is the collection of the operating cells and u is the electric potential. We remark that in our model the average voltage $\langle U \rangle_{C_i, S}$ at the site of the operated cell corresponds to the cell voltage, i.e., OCV minus cell losses, see Fig. 4.4. This average voltage is defined by

$$\langle U \rangle_{C_i, S} = L(C_i)^{-1} \int_{C_i} u_S \, dl, \quad (4.6)$$

where u_S is the potential and the subscript refers to the chosen current sink S . The model has two parameters, namely U_H and σ_{CL} . They control the y-axis intercept and the slope of the linear current voltage characteristic respectively. The slope is proportional to $1/\sigma_{CL}$. We linearize the current voltage characteristic of all cells around the same working point. In the simulation of all cells operating in parallel the individual cells actually operate at different working points on the linearized current voltage characteristic.

We now explain how the parameter U_H is determined in order to fit a given working point. In general the voltage U_H is given by the y-axis intercept of the tangent to the current voltage characteristic at the given working point, see Fig. 4.4. We wish to fit the linearized current voltage characteristic to the working point yielding maximal power. For a given fuel cell it is characterized by a pair $(I, U(I))$ at which the power $P(I) = IU(I)$ is maximal. For this particular choice of the working point we have $U_H = 2U_S$, since a voltage source with a linear inner resistance delivers maximal power at half of its open circuit voltage [17]. As stated in Sec. 4.1 at present a maximal power density of 200 mW/cm^2 is achieved at a cell voltage of 0.4 V .

For a cell area of $200 \times 200 \mu\text{m}^2$ thus the working point yielding maximal power is characterized by $I = 0.2 \text{ mA}$ and $U(I) = 0.4 \text{ V}$. Consequently we use $U_H = 2U_S = 0.8 \text{ V}$ for our simulation.

Next we need to set the slope of the linearized current voltage characteristic, i.e., we want to determine the value of σ_{CL} that fits the chosen working point. For this purpose we simulate operation of a single cell. The voltage drop occurring within the current collector is orders of magnitude smaller than that due to cell losses. Therefore the current a single cell delivers is mainly controlled by σ_{CL} even when operated within the chip, i.e., simulated including the current collector. We therefore tune the value of σ_{CL} such that the chip delivers a current $I'_{i,S} = 0.2 \text{ mA}$. The boundary value problem for this simulation is given by Eq. (4.1) with the last line replaced by Eq. (4.5) and $X = X_w \cup X_m \cup X_{CL}$, $H = H_i$, $B = \partial X \setminus (S \cup H)$, $U_H = 0.8 \text{ V}$, $U_S = 0.4 \text{ V}$, $\sigma_{TF} = 0.515 \text{ S}$, $\sigma'_{TF} = 0.113 \text{ S}$. Let $u'_{i,S}$ denote the solution of this boundary value problem. The current $I'_{i,S}$ is obtained by evaluating Eq. (4.3) on $u'_{i,S}$. Using $\sigma_{CL} = 4.89 \cdot 10^{-5} \text{ S}$ yields $I'_{i,S} = 0.200 \text{ mA}$ for all cells and both the wire current sink and the ring current sink. This value is in agreement with the target value to within less than one percent error.

The setup used to simulate operation of a single cell is shown schematically in Fig. 4.6. Cell i is operated alone such that a terminal voltage $U_S = 0.4 \text{ V}$ is delivered to the power consumer. The current $I'_{i,S}$ is computed and tuned by adjusting parameter σ_{CL} .

We are now in the position to simulate the electrostatics of the current collector when all cells operate in parallel. The boundary value problem defined by Eq. (4.1) with the last line replaced by Eq. (4.5) is solved for

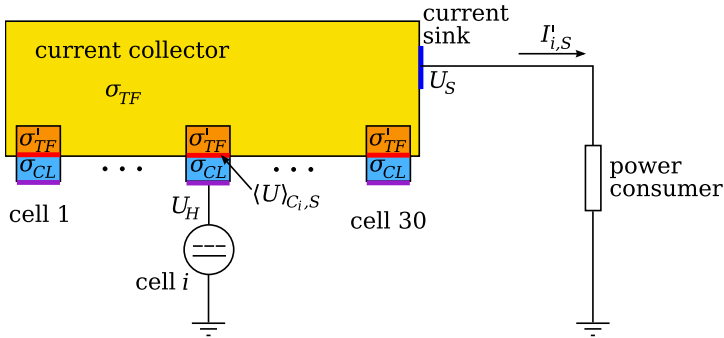


Figure 4.6: Schematic of setup used to calibrate the model used to represent the fuel cells. The values of U_S and U_H are fixed, whereas the value of σ_{CL} is tuned such that current $I'_{i,S}$ corresponds to the desired working point.

X as above, $H = \bigcup_{i=1}^{30} H_i$, $B = \partial X \setminus (S \cup H)$, $U_H = 0.8 \text{ V}$, $U_S = 0.4 \text{ V}$, $\sigma_{TF} = 0.515 \text{ S}$, $\sigma'_{TF} = 0.113 \text{ S}$ and $\sigma_{CL} = 4.89 \cdot 10^{-5} \text{ S}$. Let u_S denote the solution of this boundary value problem for the sink S . The total power P_S that the cell array delivers to the power consumer is given by the product of the voltage U_S at the current sink and the current I_S leaving through the sink. The current I_S is obtained from the solution u_S using Eq. (4.3). The setup used for the simulation of parallel operation of all cells in the chip is shown schematically in Fig. 4.7. The cell voltages $\langle U \rangle_{C_{i,S}}$, obtained from Eq. 4.6, vary for different cell sites i .

By increasing the value of σ_{CL} we can model cells with higher power output, whereas we keep the same value for $U_H = 2U_S$. Physically this corresponds to either a larger active cell area or a higher density of catalytic active sites or both together. Since we are interested in the onset of chip power limitation due to the current collector, we monitor the ratio $P_S/P'_{i,S}$ of the total power delivered by the chip and the power one cell delivers when operated alone. To keep the notation short we suppress from now on the subscripts and write P/P' , and keep in mind that this expression in principle depends on the choice of the current sink S and the reference cell site i . If no limitation occurs, the ratio P/P' is equal to the number of cells in the chip, i.e., 30 for the specific chip studied here. Thus P/P' is interpreted as the effective number of cells in the chip.

Varying the value of σ_{TF} and therewith of $\sigma'_{TF} = \alpha \sigma_{TF}$ we can simulate current collectors of varying thickness. The film thickness is given by

$$d = \sigma_{TF} \rho_P t, \quad (4.7)$$

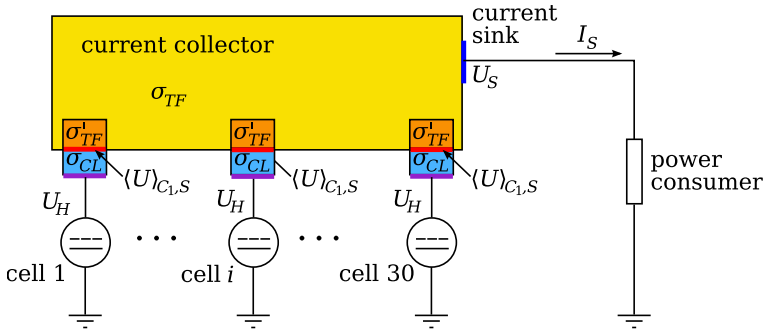


Figure 4.7: Schematic of setup used to simulate the operation of all fuel cells in parallel. The gray level gradient indicates the variation of the potential within the current collector and therewith the variation of the working points of the individual cells.

where ρ_{Pt} is the three-dimensional bulk resistivity of platinum at 400 °C.

4.3 Results

The boundary value problems described in the previous section were solved numerically by the finite element method. We employed the commercial software COMSOL version 3.5 for this purpose. The total current was determined by boundary integration. The mesh size was refined until two stable digits for the total current were obtained. The corresponding triangle meshes consisted of over 400'000 elements.

We present data from two distinct simulations. First we determine the effective resistance of the current collector. We simulate a current entering the current collector at cell site i and leaving it at current sink S . The setup used for these simulations is schematically shown in Fig. 4.3.

The effective resistances $R_{i,S}$ and the average voltages $\langle U \rangle_{G_{i,S}}$ at the boundaries G_i were computed according to Eq. (4.2) and Eq. (4.4) respectively. Tab. 4.1 lists the values for both the case where selected cells are operated using the wire current sink and the ring current sink. The selected cells cover the full variation of cell location with respect to the current sink. Note that in case of the ring sink the cell sites $i = 5, 26, 30$ are equivalent to site $i = 1$ due to symmetry. Apparently the effective resistances vary relatively strong when compared for different cells. The same is also true for the average voltages. However, in case of the ring current sink the variation is much smaller than for the wire current sink. The larger the effective resistance $R_{i,S}$, the more electrical power is lost due to conduction in the current collector. The smaller the average voltage $\langle U \rangle_{G_{i,S}}$, the lower is the loss occurring within X_w , the part of the current collector actually lying in the wafer plane. Equivalently this means that a large portion of the effective resistance is due to conduction within the walls of the etched holes. We re-

sink S	WS	WS	WS	WS	RS	RS	RS
cell # i	1	5	18	30	1	3	18
$R_{i,S}$ (Ω)	5.75	5.37	5.05	4.19	2.99	3.05	3.18
$\langle U \rangle_{G_{i,S}}$ (V)	0.648	0.623	0.598	0.516	0.322	0.336	0.362

Table 4.1: Effective resistance $R_{i,S}$ of current collector for a current from cell i to sink S , and average voltage $\langle U \rangle_{G_{i,S}}$ at boundary of etched hole at cell i . The selected cells cover the full variation of cell location with respect to the current sink. Note that in case of the ring sink the cell sites $i = 5, 26, 30$ are equivalent to site $i = 1$ due to symmetry.

mark that the effective resistivity $R_{i,S}$ from individual cells to the sink varies less than does the distance from the individual cells to the current sink. In this sense the effective resistances contain nontrivial geometric information.

Fig. 4.8(a) shows a map of the chip with an area of $23 \times 23 \text{ mm}^2$, where the colors code the potential $u_{30,WS}$. This potential is the solution of the boundary value problem defined by Eq. (4.1) for the case of the wire current sink (WS). The current collector is a Pt thin film with a thickness of 126 nm. In this particular case, close to half of the total voltage drop occurs within the absolute vicinity of cell site $i = 30$. Fig. 4.8(b) shows the potential $u_{30,RS}$, corresponding to current flowing from the cell boundary at site $i = 30$ to the ring sink (RS). The potential in the vicinity of site $i = 30$ drops faster in case of the ring sink. This is reflected in the low value of $\langle U \rangle_{G_{30,RS}}$ as compared to $\langle U \rangle_{G_{30,WS}}$. The voltages $\langle U \rangle_{G_{i,S}}$ listed in Tab. 4.1 range from 0.32 to 0.65 V. Recall that the total potential drop is 1 V. Thus roughly equal resistances are due to conduction in the walls of the etched hole and in the wafer plane.

We now come to the results for operation of cells at the working point yielding maximal power. The corresponding boundary value problem is detailed in Sec. 4.2.2. The power P' an individual cells delivers when operated alone is controlled by the parameter σ_{CL} , the conductivity within the small frames X_{CL} . As explained in Sec. 4.2.2 the value $\sigma_{CL} = 4.89 \cdot 10^{-5} \text{ S}$ corre-

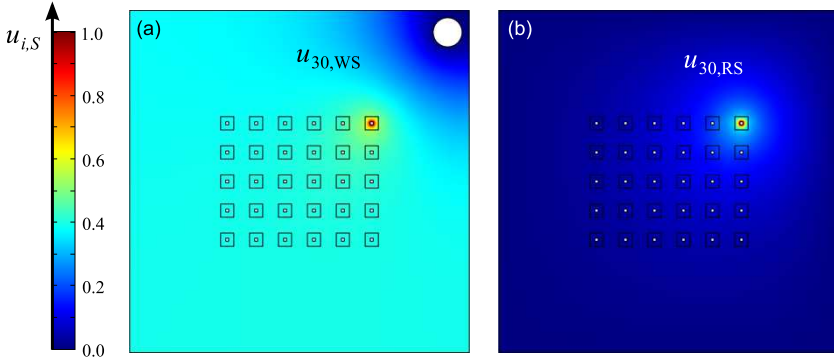


Figure 4.8: Maps of the potential $u_{i,S}$ for cell site $i = 30$, colors code the potential as given by the legend to the left. (a) shows the potential for the case of the wire sink (WS). (b) shows the potential for the case of the ring sink (RS). The potentials are solutions of the boundary value problem defined by Eq. (4.1). The current collector is a Pt thin film of 126 nm thickness covering the whole chip of $23 \times 23 \text{ mm}^2$, the effective resistance $R_{i,S}$ derived from these simulations are given in Tab. 4.1.

sponds to a moderate power output of a single cell, namely $P'_{i,S} = 80 \mu\text{W}$. For this regime of σ_{CL} the value of $P'_{i,S}$ is hardly a function of the cell site i and the current sink S . We thus write P' for short. In the regime of very high power output, i.e., σ_{CL} on the order of 10^{-3} S , the variation is about 5 %, as will be seen below. If the individual cells do not hinder each other at parallel operation, the power generated by the chip P is equal to the product of the number of physical cells in the chip and the power P' delivered by one cell when operated alone. The ratio P/P' corresponds to the effective number of cells operating at the working point yielding maximal power. For the chip considered in the present study values lower than 30 evidence that the cells hinder each other at parallel operation, i.e., the cells do not run at the working point yielding maximal power.

To assess the limits of the investigated chip layout, σ_{CL} was increased in four steps by two orders of magnitude, see the first row in Tab. 4.2. For all these five settings of the cell losses simulations of the operation of a single cell and all cells in parallel were performed. The results shown in Tab. 4.2 correspond to a film thickness of $d = 126 \text{ nm}$ of Pt for the current collector. The power delivered by individual cells $P'_{i,S}$ shows a slight dependence on the cell site i . The lower the cell losses, i.e., the larger the value of σ_{CL} , the stronger is this variation. For the investigated range this variation reaches maximal values of 6.3 % and 0.73 % at $\sigma_{CL} = 4.89 \text{ mS}$ in case of the wire sink and ring sink respectively. In view of this small variation it is irrelevant which cell site actually is used as reference to determine the value of single cell power output P' . We remark that cell at site $i = 30$ was found to have the highest power output for both types of current sink, whereas the lowest power output is obtained from cell $i = 1$ and cell $i = 18$ in case of the wire sink and ring sink respectively. Note that in case of the ring sink the cell sites $i = 1, 5, 26$ are equivalent to site $i = 30$ due to symmetry.

$\sigma_{CL} \text{ (mS)}$	0.0489	0.155	0.489	1.55	4.89
$P'_{1,WS} \text{ (mW)}$	0.0800	0.251	0.779	2.32	6.19
$P'_{30,WS} \text{ (mW)}$	0.0801	0.252	0.785	2.37	6.58
$P_{WS} \text{ (mW)}$	2.33	6.85	17.8	36.2	54.1
$P'_{18,RS} \text{ (mW)}$	0.0801	0.252	0.789	2.41	6.87
$P'_{30,RS} \text{ (mW)}$	0.0801	0.252	0.790	2.42	6.92
$P_{RS} \text{ (mW)}$	2.39	7.47	22.7	64.1	151

Table 4.2: Values of parameter σ_{CL} and the corresponding chip power output obtained from simulations of operation of a single cells $P'_{i,S}$ and all cells in parallel P_S . The thickness of the current collector used in theses simulations is $d = 126 \text{ nm}$ throughout.

From the solutions u_S of the boundary value problem describing operation of all cells in parallel the total power P_S of the chip was computed as described in Sec. 4.2.2. Fig. 4.7 summarizes the simulation graphically. As mentioned above we are interested in the dependence of the effective number of cells at the working point yielding maximal power P/P' . As can already be seen from the values listed in Tab. 4.2 the power output at parallel operation P_S depends on the type of the current sink. Fig. 4.9 shows P/P' the effective number of cells in the chip versus P' , the power that a single cell yields when operated alone using a 126 nm thick current collector. The higher P' , the smaller the effective number of cells in the chip apparently is. Boosting the performance of the cells leads to less than expected gain in chip performance. The effect is much stronger for the case of the wire current sink (WS) than for the ring sink (RS), as seen from the big gap between the two curves. We explain this in detail in Sec. 4.4.

Fig. 4.10 shows the effective number of cells P/P' as a function of the thickness of the thin film used as current collector. According to Eq. (4.7), the conductivity of the current collector, i.e., the value of σ_{TF} and therewith the value of $\sigma'_{TF} = \alpha\sigma_{TF}$, is proportional to the thickness of the current

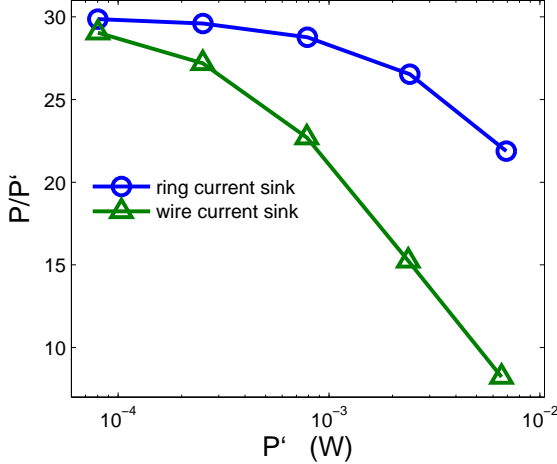


Figure 4.9: Influence of single cell power P' on chip power: P/P' is the effective number of cells in the chip at parallel operation for a platinum thin film current collector of 126 nm thickness. Data points are shown by markers, the lines are a guide to the eye. The smallest value of single cell power is $P' = 80 \mu\text{W}$, e.g. a cell with an area of $200 \times 200 \mu\text{m}^2$ delivering a power density of $200 \text{ mW}/\text{cm}^2$.

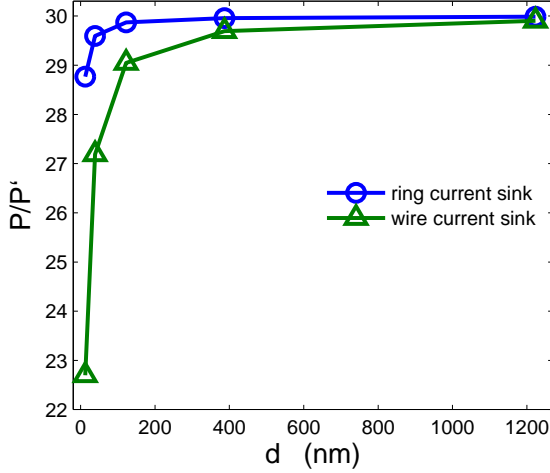


Figure 4.10: Influence of film thickness d of current collector on effective number of cells P/P' for a single cell power P' of $80 \mu\text{W}$, e.g. a cell with an area of $200 \times 200 \mu\text{m}^2$ delivering a power density of $200 \text{ mW}/\text{cm}^2$.

collector. The value $\sigma_{TF} = 0.515 \text{ S}$ as used for the data shown in Fig. 4.9 corresponds to a state of the art current collector consisting of a bi-layer of 30 nm chromium and 100 nm platinum, equivalent to a platinum film of 126 nm thickness. From this value the thickness of the current collector was both lowered and increased each in two steps by an order of magnitude. In case of the ring sink the effective number of cells P/P' is practically constant for film thickness above 40 nm , whereas for the wire sink a strong decline is observed below 126 nm . The data shown was computed using $\sigma_{CL} = 4.89 \times 10^{-5} \text{ S}$ corresponding to a single cell power $P' = 80 \mu\text{W}$, e.g. a cell of $200 \times 200 \mu\text{m}^2$ area and a power density of $200 \text{ mW}/\text{cm}^2$.

4.4 Discussion

We start with a comparison of the voltage drop due to the ohmic resistance of the current collector and that due to the intrinsic cell losses. We represent both losses by a resistance. At the working point characterized by $U = 0.4 \text{ V}$ and $I = 0.2 \text{ mA}$, i.e., when a single cell delivers $80 \mu\text{W}$, the voltage drop due to cell losses is about 0.8 V assuming an OCV of 1.2 V . Thus the cell losses correspond to a resistance of $R_{cell} = 4 \text{ k}\Omega$. The effective resistances $R_{i,CC}$ of the current collector connecting individual cells with the current sink, see

Tab. 4.1, are about three orders of magnitude smaller than R_{cell} representing the cell losses. Thus the resistance of the current collector is only responsible for a negligible part of the total losses of the studied fuel cell system. The ohmic resistance of the current collector does not limit the power that a single cell can deliver, provided all other cells are inactive. If the power output of a single cell exceeds a value of about 80 mW the losses in the current collector start to dominate over the cell losses.

Regarding the distribution of the effective resistance within the current collector we find that the voltage drop occurring within the tilted walls X_m is roughly equal to that occurring within the wafer plane X_w , see Fig. 4.8 and Tab. 4.1. This has two reasons. On the one hand the conductivity within X_m is suppressed due to the smaller film thickness and the progressed agglomeration. On the other hand the current source, i.e., the cell is very small, making the “width” of the current carrying film very small as well. Both these effects raise the effective resistance for conduction through the tilted walls.

If the fuel cells in the chip are operated in parallel, the potentials at the cell boundaries C_i are coupled by the current collector. Mathematically this is expressed by the first line in Eq. (4.1), i.e., the whole potential field must satisfy the Laplace equation. To make the coupling more tangible we describe in detail how the potential behaves at parallel operation. We start with an open circuit, thus the potential is constant over the whole current collector. Once the circuit is closed, as is shown schematically in Fig. 4.7, the potential at the current sink is lowered and current starts to flow from the cells through the current collector out through the sink to the power consumer. The lower the potential at the boundary of a cell is, the larger is the current it delivers. Due to the finite conductivity of the thin film making up the current collector a potential gradient is required to drive a current through it. The potential must decrease steadily along the path from a cell delivering current to the sink. Thus cells located close to the current collector reside on a lower potential than those located more remotely from it. This results in a variation of the cell potential with respect to the cell location. Consequently the cells in the array operate at different working points and thus not all can operate at the working point yielding maximal power. The result of this is that the power P delivered by the chip is smaller than the theoretical maximum, which would be the product of the physical number of cells and the maximal power one cell delivers when operated alone.

The effective number of cells P/P' obtained from our simulations is a quantitative measure for the reduction of the chip performance due to the effect explained above. From Fig. 4.9 we observe that the effect becomes significantly stronger for large values of P' , the power delivered by a single cell. The reason is for this is twofold. First, for fixed perturbation of the

voltage of a cell the variation of the current it delivers is proportional to σ_{CL} . In other words the lower the inner resistance of the cell the larger is the change of current it delivers when shifting the cell voltage by a certain amount. Second, for fixed current collector the modulation of the individual cell voltages is proportional to the current flowing. Thus the more power a cell can deliver, the larger is the variation of the individual working points and the much larger is the associated variation of the power delivered by the individual cells.

We stress that the ohmic loss due to the current collector is not responsible for the fact that $P/P' < 30$. If we assume that the cells do not interact with each other at parallel operation we must expect that the chip delivers at least 30 times the power the cell located most remotely from the current sink can deliver when operated alone. We thus have

$$\begin{aligned} P_{noninteract,WS} &\geq 30P'_{1,WS} \\ P_{noninteract,RS} &\geq 30P'_{18,RS} \end{aligned} \quad (4.8)$$

Computing the values on the right hand side for $\sigma_{CL} = 4.89 \times 10^{-5} \text{ S}$ we get $P_{noninteract,S} \geq 2.40 \text{ mW}$ for both the wire and ring sink. These values are larger than the actual chip powers $P_{WS} = 2.33 \text{ mW}$ and $P_{RS} = 2.39 \text{ mW}$ listed in Tab. 4.2. The difference becomes more pronounced when considering the results obtained for higher values of σ_{CL} .

The gap between the curve for the wire sink and the curve for the ring sink in Fig. 4.9 evidences the influence of the geometry of the current sink on chip performance at parallel operation. In case of the wire sink much more cells are in the situation that other cells lie between them and the current sink as compared to the case of the ring sink. This geometric difference is responsible for the poor performance of the chip using a wire current sink. Looking at Fig. 4.10 we see that to obtain equal power from two chips, one with wire sink and one with ring sink, the one with wire sink requires a ten times thicker current collector than that set up with the ring sink. This impressively demonstrates the inefficiency of the wire current sink when it comes to parallel operation of the cells in the chip. The current collector geometry influences the chip performance way stronger than its absolute resistance.

We now discuss the limits of the investigated chip layout. Let the thickness of the current collector be fixed to its standard value of $d = 126 \text{ nm}$ corresponding to a bi-layer of 30 nm chromium plus 100 nm of platinum. If the thickness of the wafer is reduced to some tens of micrometers, the active cell area could be increased to about $800 \times 800 \mu\text{m}^2$. Assuming realistic improvements in cell preparation a power density of 1 W/cm^2 can be achieved. Indeed power densities exceeding this value have been demonstrated during short term operation [18]. Combining these two improvements yields cells

that can deliver 6.4 mW. This corresponds to the highest cell power shown in our results, i.e., obtained from the simulations with $\sigma_{CL} = 4.89 \text{ mS}$. In this regime the interaction of the individual cells at parallel operation results in a significant reduction of chip power with respect to the theoretical maximum. Using the values shown in the last column of Tab. 4.2 we present the calculation explicitly. Based on the power output at operation of a single cell, the theoretically possible chip power output is $P_{th,S} = 30P'_{30,S}$. We obtain $P_{th,WS} = 197 \text{ mW}$ and $P_{th,RS} = 208 \text{ mW}$ for the wire and ring sink respectively. The corresponding chip power outputs obtained from simulation are $P_{WS} = 54 \text{ mW}$ and $P_{RS} = 151 \text{ mW}$. Thus for the wire sink the chip delivers only 27 % of the theoretically possible power. For the ring sink sink anyhow the chip can deliver 73 % of the theoretical maximum.

4.5 Conclusions

The influence on power output of a thin film current collector employed in a chip integrating 30 micro-SOFCs was investigated by simulation of electrostatics. The current voltage characteristic of the fuel cells was linearized and included individually for each cell. Although all cells have identical current voltage characteristic, the simulations show that the power output of the chip is lower than the theoretical maximum. This result is a consequence of the coupling of the cell voltages through the current collector. It creates a variation of the working points of the individual cells and thereby lowers the performance of the cells in the chip. The dependence of this effect on both the power output of the individual cells and the thickness of the current collector was studied. The performance of the chip decreases progressively with increasing power delivered by the individual cells, as well as for lowering of the film thickness of the current collector. The higher the power a single cell can deliver the more sensitive its power output responds to a variation of the working point. The lower the conductivity of the current collector, the higher is the associated modulation of the working points of the cells at parallel operation.

Two geometries for the current sink were considered. In the first one the planar current collector is attached to outer circuitry by a wire bonded to it in one corner. In the second geometry all four outer edges of the current collector are connected to outer circuitry. The geometry of the current sink has a major influence on chip performance. For the investigated geometries their difference in performance is equivalent to that obtained by changing the resistance of the current collector by an order of magnitude. When going for optimal chip performance it is thus more rewarding to tune the geometry of the current collector rather than to lower its resistance.

To optimize the geometry of the current collector and current sink we suggest that the cells be positioned well separated and as close as possible to the current sink. This could for example be achieved by a disk like current collector with the individual cells located close to its boundary and the current sink ideally along all the boundary of the disk. Alternatively the current sink could be realized by a wire attached to the center of the disk. Since the absolute resistance of the current collector is of minor importance, micro-patterned current collectors could be used to defeat performance lowering coupling of the fuel cells if they are arranged in an array type structure. The width of the individual paths should be adjusted to compensate for the difference in distance from the cells up to the point where all paths are joined.

For fuel cells with state of the art power density and cell area, the studied current collector layout in case of the wire current sink results in 3 % less chip power output as compared to the theoretical maximum achieved by non interacting cells. Assuming that in future individual fuel cells achieve two orders of magnitude higher power output, the situation changes: A chip with the here studied layout, employing a 126 nm platinum thin film current collector would yield 73 % less power than the theoretical maximum in case of the wire sink. For the case of the ring sink the reduction is still 27 %. We anticipate that the simulation scheme presented here will help to design efficient chips integrating micro-SOFCs for the next generation of portable power sources.

Acknowledgements

The author thanks his colleague René Tölke for discussions that initiated this study. The chip layout studied here is actually also due to him. Furthermore discussion of preliminary results at an internal meeting with members of the SOFC group at the institute for Nonmetallic Inorganic Materials is acknowledged. Finally the author thanks his colleague Meike Schlupp for valuable input that helped to improve the manuscript.

Bibliography

- [1] S. W. Jordan, "Technology forecasting with scientific indicators: The case of laptop batteries futures," *PICMET 07 Proceedings*, vol. 1-6, pp. 1643–1650, 2007.
- [2] R. O'Hayre, S.-W. Cha, W. Collela, and F. B. Prinz, *Fuel cell fundamentals*. Wiley, 2nd ed., 2009.

- [3] L. J. Gauckler, D. Beckel, B. E. Buegler, E. Jud, U. P. Muecke, M. Prestat, J. L. M. Rupp, and J. Richter, "Solid oxide fuel cells: Systems and materials," *Chimia*, vol. 58, no. 12, pp. 837–850, 2004.
- [4] A. Evans, A. Bieberle-Hütter, H. Galinski, J. L. M. Rupp, T. Ryll, B. Scherrer, R. Tölke, and L. J. Gauckler, "Micro-solid oxide fuel cells: status, challenges and chances," *Monatsh. Chem.*, vol. 140, pp. 975–983, 2009.
- [5] A. Evans, A. and Bieberle-Hütter, J. L. M. Rupp, and L. J. Gauckler, "Review on microfabricated micro-solid oxide fuel cell membranes," *J. Power Sources*, vol. 194, pp. 119–129, 2009.
- [6] H. Huang, M. Nakamura, P. Su, R. Fasching, Y. Saito, and F. B. Prinz, "High-performance ultrathin solid oxide fuel cells for low-temperature operation," *J. Electrochem. Soc.*, vol. 154, no. 1, pp. B20–B24, 2007.
- [7] J. H. Shim, C.-C. Chao, H. Huang, and F. B. Prinz, "Atomic layer deposition of yttria-stabilized zirconia for solid oxide fuel cells," *Chem. Mater.*, vol. 19, pp. 3850–3854, 2007.
- [8] U. P. Muecke, D. Beckel, A. Bernard, A. Bieberle-Hütter, S. Graf, A. Infortuna, P. Müller, J. L. M. Rupp, J. Schneider, and L. J. Gauckler, "Micro solid oxide fuel cells on glass ceramic substrates," *Adv. Funct. Mater.*, vol. 18, pp. 3158–3168, 2008.
- [9] P.-C. Su, C.-C. Chao, J. H. Shim, R. Fasching, and F. B. Prinz, "Solid oxide fuel cell with corrugated thin film electrolyte," *Nano Lett.*, vol. 8, pp. 2289–2292, 2008.
- [10] C. Ding, H. Lin, K. Sato, and T. Hashida, "A simple, rapid spray method for preparing anode-supported solid oxide fuel cells with gdc electrolyte thin films," *J. Membr. Sci.*, vol. 350, pp. 1–4, 2010.
- [11] I. Buchmann, *Batteries in a portable world: A handbook on rechargeable batteries for non-engineers*. Cadex Electronics, 2011.
- [12] W. M. Haynes, ed., *CRC Handbook of Chemistry and Physics*. Taylor&Francis, 91st ed., 2010. Internet Version 2011.
- [13] H. Galinski, T. Ryll, P. Elser, J. L. M. Rupp, A. Bieberle-Hütter, and L. J. Gauckler, "Agglomeration of pt thin films on dielectric substrates," *Phy. Rev. B*, vol. 82, p. 235415, 2010.
- [14] J. D. Jackson, *Classical Electrodynamics*. Wiley, 1990.

- [15] J. Reuteler, M. Hütter, and L. J. Gauckler, “Backbone of conductivity in two-dimensional metal-insulator composites,” *J. Appl. Phys.*, vol. 110, p. 024909, 2011.
- [16] J. Rutman and I. Riess, “Placement of reference electrode in solid electrolyte cells,” *Electrochim. Acta*, vol. 52, pp. 6073–6083, 2007.
- [17] P. Horowitz and W. Hill, *The art of electronics*. Cambridge University press, 2nd ed., 2001-2006.
- [18] C.-C. Chao, C.-M. Hsu, Y. Cui, and F. B. Prinz, “Improved solid oxide fuel cell performance with nanostructured electrolytes,” *ACS nano*, vol. 5, pp. 5692–5696, 2011.

Chapter 5

Focused ion beam scanning electron microscope

Abstract

This chapter gives an overview of the current state of technology of the Focused Ion Beam Scanning Electron Microscope (FIB-SEM) and its use for analyzing materials' microstructures. In the first section the technological aspects of the FIB-SEM are treated after a brief review of history and literature. The ion source is discussed in detail. The properties of a typical ion column are summarized. Then the FIB milling and deposition mechanisms are explained. In the second section the use of the FIB-SEM in material science is described. Four applications are presented in more detail, including recipes for the basic technique. The third section is devoted to examples of investigations conducted with the help of a FIB-SEM. The chapter ends with a summary and outlook.

5.1 Technological aspects of the FIB-SEM

In December 1959 the physicist Richard Feynman presented ideas on exploiting the manipulation of matter in small dimensions for information storage [1]. His talk entitled "There's plenty room at the bottom" can be seen as the beginning of what is called nanotechnology. In order to write in very small dimensions Feynman proposed to send an ion beam in reverse direction through the lenses of an electron microscope. This exactly describes what nowadays is known as Focused Ion Beam (FIB) column. In the mid 1980ies first commercial FIB systems were brought to the market. They

were used in the semiconductor industry for mask repair and microsurgery of chips. Focused ion beam technology underwent a movement that could be called “from fab to lab”: the use of FIB-SEM systems for materials characterization and rapid prototyping brought it back into the realm of academia. Several monographs about focused ion beams systems exist. The earlier ones are mainly concerned with the history and physics of ion sources [2, 3]. Whereas the more recent ones treat a vast number of applications after brief introductions to the technology [4, 5]. There are also numerous reviews available covering the topic [6, 7, 8, 9, 10].

5.1.1 Imaging cutting and writing at the nanoscale

The FIB-SEM is a microscope combining imaging, cutting and writing of materials at the nanometer scale. In Fig. 5.1 the cross-section of a FIB-SEM is shown schematically. Mounted on a large vacuum chamber are two columns, one producing a focused electron beam and one producing a focused ion beam. The electron beam serves mainly for imaging and the ion beam serves mainly for cutting and writing. The crucial feature of the FIB-SEM

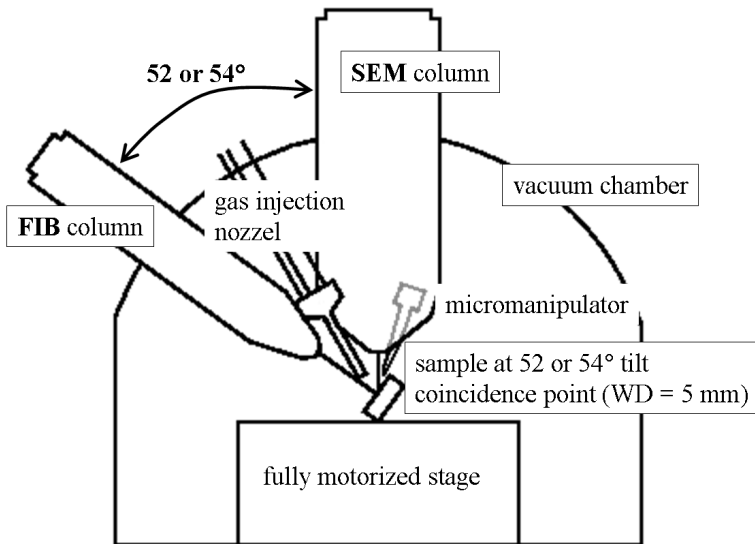


Figure 5.1: Schematic of a modern FIB-SEM system. The electron and ion column are mounted on a large vacuum chamber such that the electron and ion beam meet in a point about 5 mm below the pole piece of the electron column, this is called the coincidence point.

is that the two columns are aligned such that the beams meet in a point: the coincidence point. A sample located at the coincidence point can be modified locally by the focused ion beam and at the same time it can be imaged with high resolution by SEM. The synergy of the two columns is what makes the FIB-SEM a powerful instrument.

To become a FIB-SEM operator understanding the geometry is essential [11]. Indeed the importance of the spatial arrangement of the different components of a FIB-SEM cannot be overstated, since the possible applications are tightly bound to the geometry in the FIB-SEM. There exist some highly specialized instruments where the positioning of the two columns is optimized for a specific application, see Sec. 5.2.6. Here only the standard FIB-SEM geometry will be discussed. The angle between electron and ion column is 52° for instruments from FEI and 54° for instruments from Zeiss SMT. Typically the coincidence point is located at 5 mm below the pole piece of the electron column. The distance to the pole piece of the ion column is around 15 mm, see Fig. 5.1. The high mass of the ions makes the focused ion beam quite stiff, so there is no need to reduce this distance. For the latest generation of FIB-SEMs the coincidence point has moved to 4 mm below the pole piece of the electron column in order to push the resolution limit further down. The pay off is an even more tight arrangement of all components. The limitation of space can only be fully appreciated when taking into account that for many applications both a gas injection nozzle, supplying a precursor gas for writing lines of material on the surface of the specimen, and a micromanipulator to move small sample pieces around, have to reach the coincidence point, see Fig. 5.1.

Fig. 5.2 shows an image of the Zeiss NVision 40 located at the Electron Microscopy center of ETH Zurich (EMEZ). Students are trained to operate FIB-SEM systems on a regular basis at EMEZ. A tutorial for teaching how to operate a FIB-SEM can be found in [12].

Next we discuss which kind of samples can be investigated in a FIB-SEM. In semiconductor factories the samples are whole wafers, requiring large holders and huge vacuum chambers. For most investigations concerning basic research the standard sample holder, a mushroom shaped metal piece with a flat top area of about 1 cm^2 will offer sufficient space to glue a piece of the solid material of interest to it. It is beneficial if the surface of the sample is rather flat on the length scale of millimeters. Highly elevated parts increase the risk of crashing the sample into the SEM pole piece or hitting it by the gas injection nozzle. Beams of charged particles interact with all atoms, thus also with gases. Therefore a sample has to be held under high vacuum for investigation by a focused electron or ion beam. For standard FIB systems the working pressure in the sample chamber is in the range of 10^{-6} to 10^{-5} mbar (high vacuum). Since both probing beams deliver charge

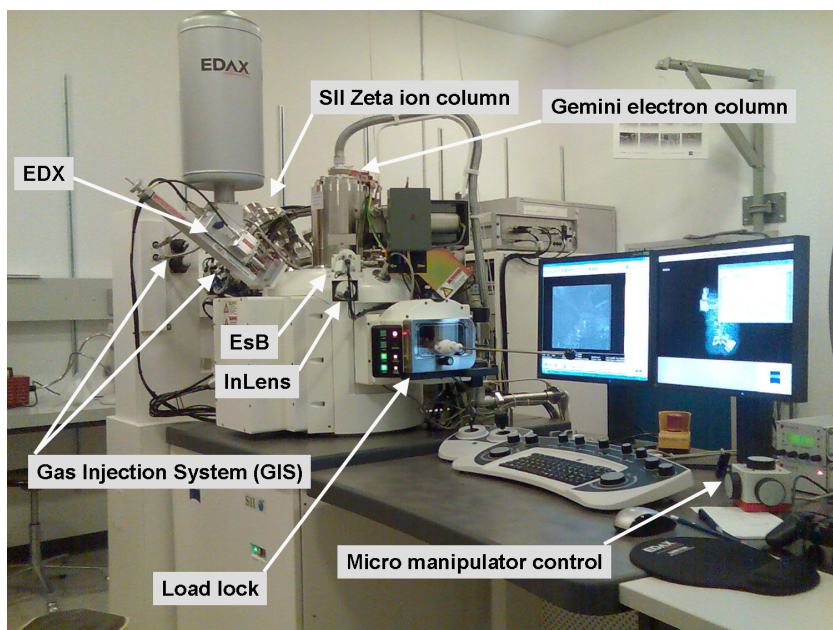


Figure 5.2: Zeiss NVision40, the FIB-SEM system located at the electron microscopy center of ETH Zurich.

to the sample it is furthermore necessary to ensure that the charge can leave the sample. For conducting samples it is sufficient to use a conducting glue when attaching it to the sample holder. If the sample is insulating one has to coat it with a thin conducting film, e.g. by sputtering with a noble metal or carbon to it. Another solution is to use a so called environmental pressure system. Such systems are designed to be operated at a chamber pressure of 10^{-3} mbar. At such pressure the gas in the chamber will continuously discharge the sample in case it is insulating and accumulates charge when probed. However the resolution in such systems is lower than for systems operated at high vacuum since the probing beams are scattered by the gas atoms on their way from the pole piece to the sample.

5.1.2 The Liquid Metal Ion Source (LMIS)

An excellent review with some tutorial content covering the relevant aspects of liquid metal ion sources was given by Forbes [13]. Following his description we first describe the discovery of the Taylor-Gilbert cone. Then the basic physics of the Liquid Metal Ion Source (LMIS) is discussed. At the end of

this subsection the build-up and properties of modern Ga LMISs as used in nowadays FIB systems are discussed.

In 1600 Gilbert reported that the surface of a drop of water sitting on a dry support will be pulled up forming a cone when a rubbed piece of amber is held at suitable distance to it [14]. In 1882 Lord Rayleigh predicted that a droplet with a surface charge exceeding a certain threshold value will eject two fine jets [15]. This was confirmed experimentally more than 100 years later [16]. Early in the 20th century Zeleny reported his experiments where he exposed alcohol and glycerine contained in glass capillaries to some thousands of volts [17, 18]. He observed various modes of electrospraying: for sufficiently strong electric fields a narrow beam of fluid is ejected from the apex of the cone. He published images showing jets emerging at the apex of liquid cones, see Fig. 5.3. At some distance from the cusp the fluid thread disintegrates and forms droplets. He noted that no light is emitted by the fluid cones and concluded that all charge transfer must be due to charged droplets and that no gaseous ions are produced. Fifty years later the first adequate theory to describe the phenomenon was put forward by Taylor [19]. His analysis is based on the assumption that local pressure balance at the

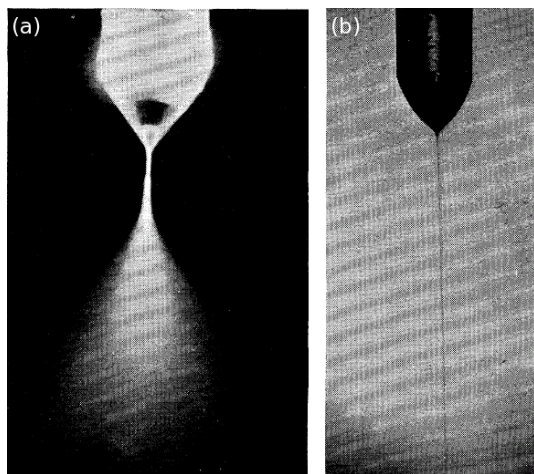


Figure 5.3: Photographs of fluid drops at the end of a capillary in a strong electric field. The drops are deformed into cones. At the tip the fluid is ejected, the effect is called electrospraying. (a) Water alcohol mixture. The narrow beam disintegrates and forms droplets after a short distance. (b) Glycerine yields a relatively long thread before disintegration. Images taken from reference [17]. Copyright (1917) by The American Physical Society.

surface of the fluid must hold. He showed that under special circumstances a fluid in an electric field takes on a cone shape with an opening angle of 98.6° in equilibrium. Following Forbes the mathematical cone should be called Taylor cone, whereas the physical cone observed in experiments should be called Taylor-Gilbert cone.

In the 1960ies interest in metal ion sources was fueled by their possible application for spacecraft thrusters. At that time Krohn sprayed Wood's metal from a small capillary and observed that most of the current was carried by ions rather than by charged droplets [2]. In 1975 Krohn and Ringo reported the high brightness found for their ion source [20]. They exposed a capillary containing fluid metal to a voltage of 20 kV causing a current of about 10 μ A. An alternative setup using a tungsten needle placed in a pool of the liquid metal was investigated at the same time by Clampitt and coworkers [21]. Without the needle an array of emitting cones is obtained, the spacing being determined by the strength of the electric field. The tungsten needle anchors one emitting cone and suppresses the formation of others. The advantages of this setup are the ease and stability of operation [22]. By the end of the 1970ies the application of ion beams was mainly envisaged in the range from atom physics to microprobes [23, 24]. In contrast to the early experiments done with non conducting fluids, the emission at the cusp of liquid metals is accompanied by intense luminosity. For low currents the massive emission products are mostly ions and only few neutrals in form of droplets are ejected from the cusp. Numerous metals were investigated, among them are Au, In, Cs and Ga. The later was found to have most favorable properties: the melting point is slightly above room temperature, the liquid Ga has an exceptionally low vapor pressure and the emitted ions are dominantly single charged. Based on measurements of the onset of emission Swanson showed that for many elements and surely for Ga the emission mode is field evaporation, i.e., the charging and emission of the ion occur in one step [25]. Thus the liquid metal takes on a more and more conical shape for increasing electrical field. Above the threshold voltage emission occurs at the apex where the electric field is highest. The transition region is relatively narrow. Several investigations of the liquid metal cone during operation were made by in-situ TEM, see Fig. 5.4. Using a 2.5 MV TEM detailed images of the cone in a Ga LMIS could be obtained [26]. This allowed to observe the dynamics of the source during onset of ion emission. At a voltage below emission the liquid metal wetting the tip is elongated giving it an ellipsoidal shape. Just below the threshold the liquid metal oscillates from ellipsoidal shape to cone shape. About 10 V below the threshold the frequency of the oscillation increases and an oscillating ion current can be measured. Right above the threshold continuous emission from the cone is observed with a minimal current of about 1 μ A. Increasing

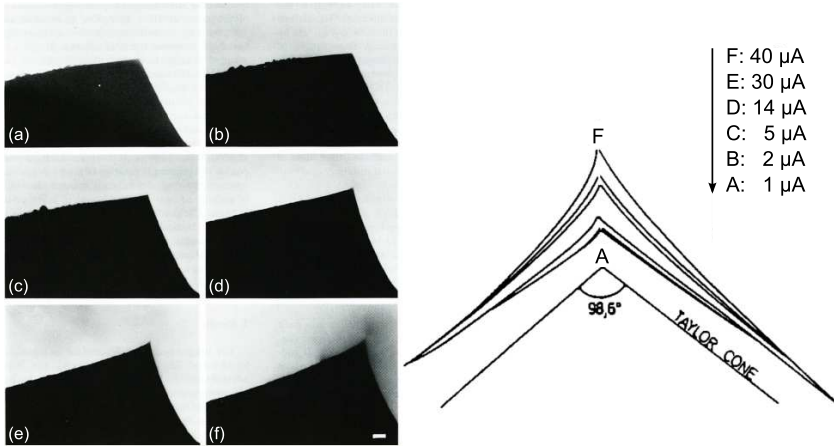


Figure 5.4: 2.5 MV TEM images of the Gilbert-Taylor cone. (a) onset of emission, $I < 1 \mu\text{A}$, $U = 4.63 \text{ kV}$, (b) $I = 2 \mu\text{A}$, $U = 4.63 \text{ kV}$, (c) $I = 5 \mu\text{A}$, $U = 4.7 \text{ kV}$, (d) $I = 14 \mu\text{A}$, $U = 5 \text{ kV}$, (e) $I = 30 \mu\text{A}$, $U = 5.5 \text{ kV}$, (f) $I = 40 \mu\text{A}$, $U = 6.2 \text{ kV}$. The marker represents 100 nm. On the right side the different silhouettes are compared to each other and to the Taylor cone. Images taken from [26] with permission of Elsevier.

the voltage further leads to a higher emission current. Along with the onset of continuous emission a cusp occurs at the apex of the cone. It grows with increasing current, see Fig. 5.4. Furthermore the sidewalls become more and more concave. At the end of the cusp ions are pulled out of the liquid by the intense electric field. The ions then fly towards the apertured cathode and form the ion beam. Measurements of the energy distribution for a Ga liquid metal source yields a value of about 5 eV FWHM for emission currents around $1 \mu\text{A}$ [13]. The energy spread increases with the current, reaching 30 eV at $20 \mu\text{A}$. There is consensus that the energy broadening is due to repulsive coulombic particle particle interactions of the ions close to the point of emission (Boersch effect). Using a Ga LMIS and a single-lens column Seliger *et. al.* investigated the attainable spot size of the ion beam [27]. They determined the spot sizes from the width of grooves sputtered into a Au thin film on a Si substrate. Using the dependence of the spot size on the source current they concluded that chromatic aberration limited their spot size.

The main application of LMIS is now in the field of microprobes and micropatterning. Practically all FIB systems are based on a Ga-LMIS operated at a current of $2 \mu\text{A}$ to obtain minimal energy spread. Fig. 5.5 shows

an image of a modern Ga-LMIS from FEI. A coil of tungsten wire serves as reservoir for the gallium. From the coil a tungsten needle points out. The shaft of this needle is rough and has grooves. These grooves assist the flow of liquid gallium by capillary action, therefore such sources are called “viscous-drag-free” [13]. Initially very sharp needles were used. An undergraduate student supervised by Clampitt discovered by accident the superiority of blunt needles. She blew the tip off a sharp needle by too high a voltage and obtained much higher currents thereafter. The explanation is that on a tip with a radius of few microns a Taylor-Gilbert cone can form. The coil holding the Ga also serves to heat in order to keep the Ga liquid under operation. Every hundred hours or so it is necessary to heat the reservoir strongly in order to wet the whole needle again properly. The typical lifetime of commercial Ga-LMISs is about 4000 μAh , this corresponds roughly to half a year of operation.

The physics of liquid metal ion sources is an interesting topic by itself. The understanding of the working principles of LMIS was developed in the 1970ies. In summary we can state that due to the formation of a Taylor-Gilbert cone the emission of ions in LMIS occurs in a region of only few nanometers of diameter. The minimal energy spread is obtained at an emission current of 2 μA .

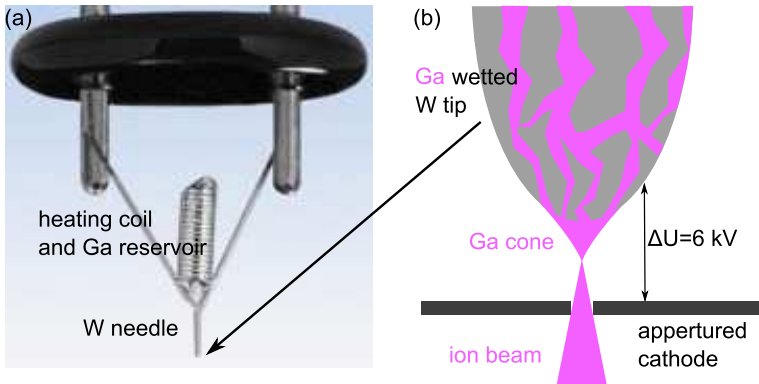


Figure 5.5: (a) Photograph of a Ga LMIS (courtesy of FEI company). (b) Sketch of situation at the tip of the tungsten wire. The apex radius is on the order of few μm . Flow of liquid Ga is facilitated by grooves along the shaft of the W wire.

5.1.3 Characteristics of FIB columns

The ion beam obtained right after extraction from the source is divergent. To make use of the ion beam as a microprobe it has to be focused into a spot and its current has to be adjusted according to need. A modern FIB column contains various lenses and apertures for this purpose, see Fig. 5.6. To allow the ion beam to travel unaffected by collisions the whole column has to be pumped to ultra high vacuum, i.e., a pressure of 10^{-9} mbar or less. The condenser lens together with a motorized aperture strip serves to adjust the landing current. Typically there are more than a dozen discrete current settings covering the range from 0.1 pA to 40 nA. The current sequence is adjusted such that for each step the current roughly doubles. The standard currents of the SII Zeta column employed in the Zeiss NVision 40 are listed together with their spot size in Tab. 5.1.

Assuming that all current lies in a disk with a diameter given by the spot size, the current density can be estimated. In Fig. 5.7 the spot size

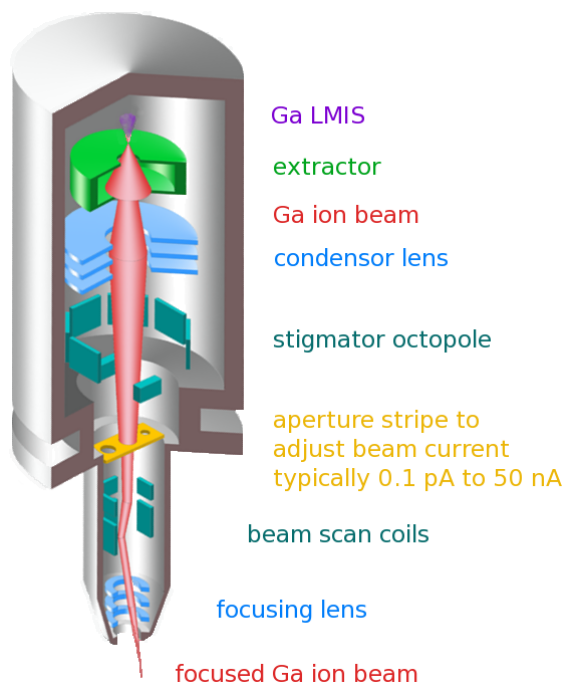


Figure 5.6: Schematic depicting components and build-up of a modern FIB column. (Courtesy of Zeiss)

current (pA)	0.1	0.3	1	10	40	80	150	300	700	...
spot size (nm)	4	5	7	13	19	22	29	38	59	...

...	1500	3000	6500	13000	27000	45000
...	107	170	300	900	2500	5100

Table 5.1: Performance of SII Zeta FIB column: spot size at all current steps.

and estimated current density are plotted versus the current. The current density is highest for currents around 3 nA. The real current density follows a Gaussian curve in the middle and then exponential beam tails follow [6]. The current density profile furthermore changes when moving up or down from the focus point. In the focus point, i.e., when optimal image resolution is obtained, the beam has a very narrow maximum with extended side wings. Slightly above the focus point the beam shows a more broad maximum and virtually no side wings, this is the optimal situation for milling [10].

The ions are extracted by a voltage of about 6 kV. The precise value depends on the wetting state of the tungsten tip in the Ga-LMIS. In standard operation the ions are then accelerated at 30 kV. This allows to focus the beam well into a small spot and yields a rather robust beam which can travel tens of millimeters in vacuum without degrading. More recently the beam quality for smaller acceleration voltages has been improved. Acceleration

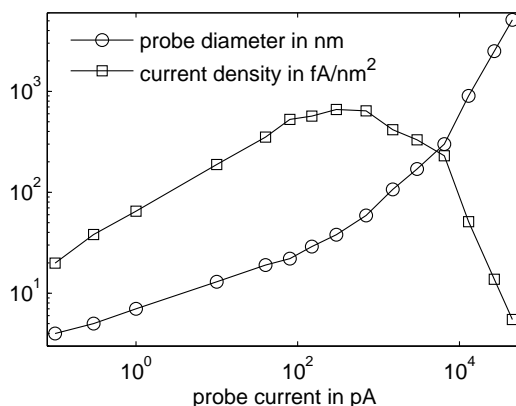


Figure 5.7: Performance of SII Zeta FIB column. Spot size, shown by open circles, in nm and current density, shown by squares, in fA/nm² versus beam current. Lines are a guide to the eye.

voltage of 5 and 2 kV are provided now by most FIB columns. FEI has managed to tune a FIB column such that acceptable focused beams are obtained at 1 kV and even as low as 500 V. Such low acceleration voltages result in beams with spot sizes in the range of micrometers and are primarily used to remove surface damage on TEM samples, see Sec. 5.2.7. As explained in Sec. 5.1.2 the minimal spot size achievable with a Ga-LMIS is limited by chromatic aberration. At best spot sizes of about 10 nm can be expected. Lower values are obtained when the side wings of the beam are neglected which is meaningful when considering image resolution only.

5.1.4 Interaction of Ga ions with solids

An ion impinging on the surface of a solid sample penetrates into the sample only some tens of nanometers. Along its way through the solid the ion collides several times with the atoms, leading to displacement and transfer of energy to them. Finally after some tens of picoseconds the primary ion comes to rest and remains in the solid [9]. As a result of the displacements and energy transfer, some atoms near the surface may leave the solid. This effect is called sputtering. The number of sputtered atoms per incident ion is the sputter yield. It varies from one to ten depending on the material and its crystallographic orientation. On average the sputter yield is about two. For normal incidence of the ions the sputter yield as a function of ion energy increases strongly up to 5 kV and then remains almost constant to 50 kV. For grazing incidence the sputter yield still increases above 5 kV [4]. Only a small fraction of the sputtered material leaves the sample in form of ions. The signal can be used for imaging. This technique is called Scanning Ion Microscopy (SIM). Simultaneously to the ejection of atoms and ions also electrons are knocked out of the solid, so called secondary electrons. Furthermore lattice vibrations as well as x-rays and visible light are generated. Fig. 5.8 summarizes the interaction products and illustrates the concept of the collision cascade.

In practice a current of about 100 pA is used to raster a sample by the focused Ga beam in order to obtain an image using either the secondary electron or the secondary ion signal. The penetration depth of the primary ions and therewith the depth in which most of the energy transfer occurs depends on the crystallographic orientation of the solid with respect to the incident ion beam. Seen from certain low index directions the atoms in the solid line up in rows forming channels through which the impinging ions can penetrate deep into the solid. The generated electrons and ions hardly can escape thus only a weak signal is produced. Conversely, if the atoms in the solid are seen from an odd angle showing no channels the ion will get stuck closer to the surface resulting in a strong electron and secondary ion

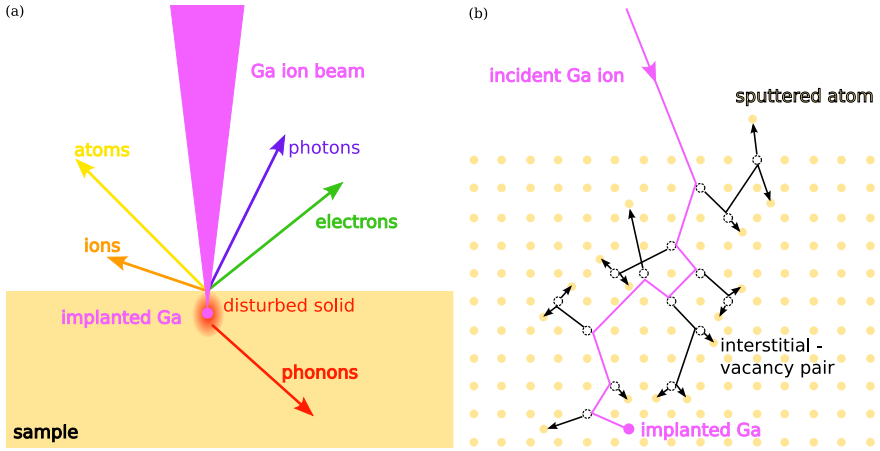


Figure 5.8: Schematic of the interaction of a Ga ion beam with a solid sample. (a) The impinging ions cause ejection of secondary electrons, atoms (sputtering), few secondary ions and photons (x-rays and visible light). Within the sample the crystal structure is disturbed in a region of some tens of nanometers in diameter. Furthermore phonons (lattice vibrations) are generated and Ga is implanted. (b) The current model for the ion-solid interaction is that the initial energy of the impinging ion is transferred in a cascade of collisions to the sample. The collisions lead to displacement of atoms thereby generating defects. Typically interstitial-vacancy pairs are formed. Atoms near the surface to which an energy greater than the displacement energy of the solid (≈ 20 eV) is transferred may leave the solid, this is the sputtering process. (Schematic (b) is adopted from [9].)

signal. This effect is called channeling contrast and is typically observed for polycrystalline metals. If the sample is scanned over and over repeatedly one can follow the changes induced by the ion irradiation. In most cases an irregularly corrugated surface will be created, obscuring the initial structure of the sample. Such removal of surface layers is beneficial in case a surface contamination needs to be removed before investigation.

The local removal of material from the sample using a focused ion beam is called milling. In practice typically a map of the area to be milled, called milling pattern, is created through a graphical user interface. Simple geometric shapes like rectangles or trapezoids are drawn as overlay on an image of the sample that was previously acquired by scanning with the FIB. For every milling object the milling current and scan strategy has to be defined. A large milling current will remove material very fast and realize the pre-

scribed shape with low precision. Milling with a small current takes more time but the result will be closer to the prescribed shape. The term “milling strategy” refers to the way in which the ion beam is scanned over the prescribed shape. A rectangle scanned once line by line from bottom to top will yield a trench that is deepest at the top and rather shallow towards the bottom line. This is a consequence of both redeposition and enhanced milling for shallow incidence angles. Redeposition refers to the effect that sputtered material can condense again to the sample surface, in general at a different location than it was sputtered from. Redeposition tends to fill up holes on the surface of the sample. The sputter yield for grazing incidence is larger than for normal incidence. This is simply due to the fact that at grazing incidence the energy and momentum from the primary ions is mostly transferred to atoms in the vicinity of the surface, thus leading to a higher probability for the atoms to escape from the solid. Milling of the first line yields a groove in the sample. When the second line is milled the beam hits the edge of the groove, i.e., part of the beam is incident at grazing angle. Therefore more and more material is removed for every further line. At the same time redeposition fills up the previously milled area continuously. To obtain an even depth over the whole milling shape the ion beam needs to be scanned in several layers over the whole milling area. This removes continuously the redeposited material and decreases the influence of the edge effect. In order to combine efficient milling with accurate milling, a step by step strategy is employed. First one mills with a large current the rough shape and then refines it with a small current where necessary. The surface roughness on a FIB cut wall can be reduced to the sub nanometer range using small milling currents.

Employing a local gas atmosphere at the location where the ion beam hits the sample it is possible to achieve enhanced milling (increased sputter rates) or deposition of a solid. The local atmosphere is created by delivery of gas through a nozzle positioned about 200 μm above the sample surface.

In order to enhance the milling rates, gases forming volatile compounds with the sputtered solid are employed. Examples of such etching gases for use in FIB systems are Cl_2 , I_2 , H_2O and XeF_2 . For well working combinations of solid and etching gas the enhancement of the sputter yield is on the order of a factor of ten. In Tab. 5.2 the enhancement factors for sputter yields for some combinations of solid and etching gas are given. The selectivity of the enhancement of the milling rates can also be exploited: instead of milling free an Al wire embedded in Si using several precisely positioned boxes one may apply a XeF_2 atmosphere and mill all over. Due to the very different sputter rates the Si surrounding the Al will be gone quickly, whereas the Al remains mostly intact.

For deposition of material precursor gases are delivered to the sample

	Si	SiO ₂	Al	W	GaAs	InP	PMMA
Cl ₂	7-10	1	7-10	1	50	4	-
Br ₂	5-6	1	8-16	1	-	-	-
I ₂	5-10	1	5-15	-	-	11-13	2
XeF ₂	7-12	7-10	1	7-10	-	-	4
H ₂ O	0.05-0.1	0.1-0.15	0.02-0.05	-	-	-	18

Table 5.2: FIB milling rate enhancement in presence of etching gases. Values taken from [4].

surface where they adsorb. If such an adsorbed precursor molecule is hit by the ion beam it decomposes. The volatile carrier escapes to the vacuum and the solid compound remains on the sample surface, see Fig. 5.9. This process is called Focused Ion Beam induced Chemical Vapor Deposition (FIB-CVD). Using for example W(CO)₆ an electrically conducting solid composed of 75 % nanocrystalline tungsten, 10 % carbon, 10 % gallium and 5 % oxygen can be grown [4]. Under the deposited material the surface of the sample is disturbed by the ion dose delivered by the first few scanning passes. There are precursors for deposition of various metals such as W, Al, Pt and Pd, as well as carbon. They all yield electrically conducting deposits. A combination of a Si containing precursor with H₂O gas yields deposition of insulating SiO₂.

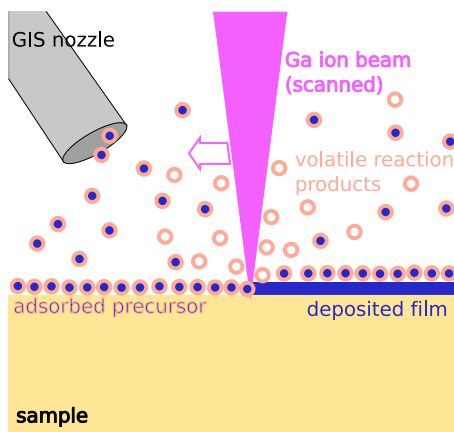


Figure 5.9: Material deposition by FIB: capillary supplies precursor gas (e.g. metal-organic compound), at the site of ion bombardment the precursor is cracked, the solid products (metal) remain on the sample and the volatile products (organic) escape into the vacuum and are pumped away.

The water serves to remove carbon from the deposit. Deposition of insulating material is used to alter circuits in microchips. Though it is possible to deposit patches of material smaller than a square micron one has to be aware of an effect called overspraying. It has been observed that within a distance of some microns from the FIB scanned region the sample surface is contaminated with a solid residue from the precursor. This shadow can even be conducting, therefore a spacing on the order of 10 μm is required to produce mutually isolated individual lines [28, 29].

5.2 Application of the FIB-SEM

The different tasks performed with FIB-SEM systems nowadays are extremely diverse. They cover the range from highly specific applications carried out only in one place on the whole world to completely standardized routine work done on a regular basis pretty much all over the world. Overviews can be found in [4, 5, 10]. The impressive number of applications that have been developed using FIB-SEM systems is direct evidence of the synergy of imaging and machining at the nanoscale. Besides the electrons and the ions there is a third ingredient that contributes to the versatile operation capabilities of a FIB-SEM system and that are micromanipulators. They “give your microscope a hand” as formulated by micromanipulator manufacturer Kleindiek. As in our daily experience with solid matter on the macro scale we can control the position of our specimens in the micro- and nanoscale. Physics is quite different in those dimensions so we need to train our intuition if we want to take advantage of the micro world. Coulombic and Van der Waals forces dominate and gravity becomes virtually irrelevant. So actually the synergy of imaging, machining and moving matter on the micro- and nanoscale brought about the multitude of applications of a FIB-SEM.

The following discusses several examples of applications and is intended to convey a feeling for the possibilities of FIB-SEM systems equipped with micromanipulator. It is not a comprehensive list of all possible applications of a FIB-SEM system. The first two applications concern the physical characterization of materials that have small length scales, such as carbon nanotubes, whiskers, nanowires and nanorods. The aim is to set up a measurement or to produce a device containing a sample with extremely small dimensions. Then two examples follow with samples that are exposed to the ion beam in order to modify their structure or geometry. The fifth and sixth subsection describe how the FIB-SEM is employed in order to obtain two and three-dimensional images of the microstructure of materials. The last two subsections treat FIB based preparations of samples for producing im-

ages with atomic resolution. The degree of detail in which the applications are presented reflects the authors experience as FIB-SEM operator. Some hints relevant for FIB-SEM operators are given where this appears valuable.

Since FIB-SEM systems constitute a major investment the operator has to find a balance between working fast to save time and working carefully to avoid braking the machine. The best strategy is leaving out unnecessary steps and following established control procedures to avoid crashing samples into the GIS, the micromanipulator needle or the SEM pole piece.

5.2.1 Microcontacting

To characterize electrical properties of a material usually one sets up a four point probe measurement. Typically the microscopic sample is placed on an insulating substrate on which micropatterned thin film electrodes have been applied. To complete the wiring the sample, which ideally should have a rod like shape, is contacted by deposition of conducting material, e.g. W or Pt by FIB-CVD. Fig. 5.10 shows a SEM micrograph of such a setup. The sample is a Bi nanowire oriented vertically. The micropatterned thin film electrodes lead out towards the four corners of the image. Due to the overspray effect mentioned earlier it is necessary to separate the contacts by several microns to avoid short cuts [29]. In the case of carbon nanotubes the work function of the material used for contacting affects the behavior of the contact. Pd is believed to be suitable for obtaining ohmic contacts. The situation is different for Bi nanowires, which are covered by a naturally

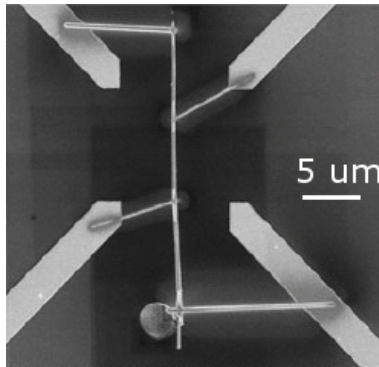


Figure 5.10: SEM micrograph of a vertically oriented Bi nanowire connected to four microstructured thin film electrodes by FIB deposited Pt wires. The overspray appears as bright halos around the deposited Pt wires. (Reproduced from [28] by permission of the Institute of Physics Publishing.)

occurring insulating oxide layer. To obtain ohmic contacts small holes can be milled through the nanowire and subsequently filled with conducting material [28]. For measurement of small irregularly shaped crystals it is also useful to mill the crystal into a well defined geometry before contacting. With a clever geometry it is even possible to assess the crystallographically induced anisotropy of the conductivity on one small single crystal [30].

5.2.2 Micromechanical testing

In order to measure mechanical properties of small samples usually tensile testing is performed. The sample is picked up with a micromanipulator and brought into contact with an unmovable wall at one end. using FIB-CVD the sample is soldered to the fixed wall. The other end can then be soldered to a micromanipulator coupled with a force sensor. With such a setup the stress-strain curve of tiny samples can be recorded [31].

For compressive testing pillars with a diameter down to some 100 nm are cut out at the surface of a smooth sample and punched with a flattened nanoindenter or AFM tip [32]. To prepare the sample a ring is milled into the surface by scanning the ion beam in a series of circles lying one inside the other. The outer diameter has to be large enough to ensure that the punch will only touch the pillar which is left in the center.

5.2.3 Holes for various purposes

By FIB milling holes with dimensions from about 100 nm up to some tens of μm in diameter can be drilled into practically any material. Large holes may serve as microcavity in an Anvil cell, whereas small holes with a diameter of some 100 nm can serve for a mask to generate a diffraction pattern of rings from an x-ray source. Arrays of thousands of holes act as photonic crystals and can be used as waveguides in optoelectronic devices [33].

The smallest hole diameter is obtained by letting the ion beam irradiate a single spot for some time. The resulting hole will look like the root of a tooth: widest at the top and thinner and thinner down to the tip. Often it will even be curved at the lower part. To obtaining holes with close to cylindrical shape the ion beam has to be scanned in several layers in a spiral starting at the center and ending in a circle with the desired hole diameter.

5.2.4 Ion irradiation

Scanning the ion beam over a sample leads to irradiation of the surface with a specific ion dose. Due to the ion bombardment the sample surface layer is altered permanently down to the penetration depth of the impinging ions.

Typically this is some tens of nanometers. For most materials the disturbed layer turns amorphous. In some cases grains with a specific orientation grow, thereby turning the “disturbed” layer virtually single crystalline. Changing the direction of irradiation allows to “switch” the crystal orientation back and forth several times [34].

Thin multilayers are mixed upon ion irradiation. This has been exploited to generate an array of small islands in a ferromagnetic multilayer. The irradiated lines loose ferromagnetism more or less depending on the ion dose. This allows to tune the behavior of the array from more collective to more individual [10].

Since practically all of the incident ions get stuck in the sample, ion irradiation can be used for local doping of samples. Thermal treatment may be required to heal the crystal damage after this doping procedure.

5.2.5 Cross Section

At its heart material science and engineering is the art of controlling properties of a material by tuning the microstructure. To accomplish this, visualization of the internal structure of materials is very helpful. On the one hand a magnification mechanism is needed, and on the other hand samples have to be cut to expose the interior. Conventionally materialographic cross sections are prepared by mechanical means. For many purposes this is a well suited method. However, there are cases where problems due to surface roughness and surface modification by the mechanical polishing have made the investigation of the undisturbed internal microstructure impossible. This is where the FIB-SEM steps in.

The procedure to prepare a FIB polished cross section is schematically shown in Fig. 5.11. First a stripe for surface smoothing and protection is deposited. If the topmost layer of the sample is of interest, as in the case of a thin film on a substrate, the stripe is deposited in two steps: first by electron beam induced CVD and then by FIB-CVD to achieve a reasonable thickness quickly. Then a trapezoidal trench of roughly the same height as the target depth of the cross section is milled with a large ion current at about one micrometer distance from the deposited stripe. Using a sequence of thin rectangles with slightly decreasing width the exposed section is made steeper and smoother. During milling it is possible to monitor the progress by SEM. Decreasing the width of subsequent milling boxes helps to see where the ion beam starts scanning for each milling box. This facilitates to adjust the position during milling in case a certain current has a spatial offset with respect to the one used beforehand. A significant gain of contrast in SEM images is observed when a milling current giving a good quality of the cross section is reached. Depending on the sample this is the case with milling

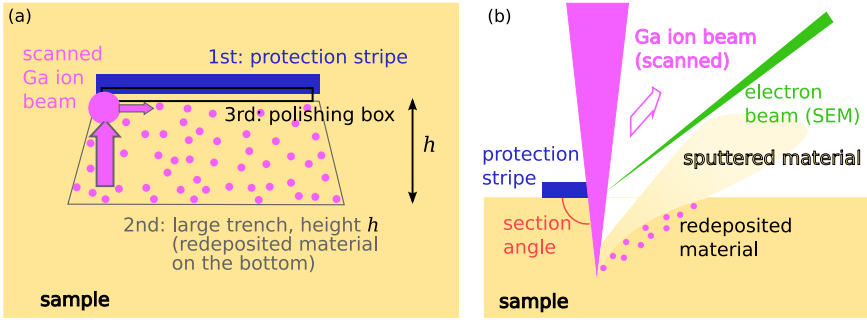


Figure 5.11: Preparation of a FIB cut cross section. (a) Top view showing the arrangement of milling boxes. The ion beam scans line by line towards the protection stripe. (b) Side view showing the trench milled and partially filled with redeposited material. The section angle approaches 90° with decreasing milling current.

currents of 50 pA or less. The final milling is referred to as polishing.

After polishing the cross section is ready for imaging by the SEM. Assuming that the normal of the sample surface is tilted by 54° (typical for a Zeiss FIB-SEM) away from the electron column, the cross section normal is tilted by 36° to the axis of the electron column. It is convenient to acquire the SEM images with an equalized y-axis. Thus in the y-direction the electron beam has to be scanned in steps reduced by a factor of $1/\cos(36^\circ)$ with respect to the spacing in x-direction. Images acquired without such equalization yield a compressed representation of the height of the cross section. If a porous structure is cut, one can deposit a carbon layer by electron beam induced CVD onto the cross section prior to the final polishing step. The benefit of filling the pores this way prior to polishing are twofold. First the cross section is less prone to becoming wiggly (water fall effect, see below). Second the resulting images are easier to segment since they exhibit proper gray level contrast between solid and pore space. In general is advantageous to infiltrate porous samples with some resin prior to investigation in the FIB-SEM. The technique to do so is the same as practiced in conventional materialography.

FIB cut cross sections can be prepared with areas ranging from less than one μm^2 up to $10^3 \mu\text{m}^2$. They can be placed at sites of interest with a precision in the range of some tens of nanometers. The roughness of the polished cross section is typically in the sub nanometer range for dense samples. For porous samples however, it can reach tens of nanometers due to the so called waterfall effect. The incident ion beam is deflected by surfaces at grazing

angles. Thus the surface topography of the sample can cause a wiggly cross section surface (see images shown in Sec. 5.3.4). In general it takes about an hour to prepare and image a cross section. For investigation of thin films it is absolutely sufficient to cut long but shallow cross sections. This allows to prepare and image a cross section in about half an hour. Once a cross section has been prepared it can be imaged or repolished easily at a later stage. Qualitative analysis of the elemental composition of the exposed internal of the sample is possible by Energy Dispersive X-ray spectroscopy (EDX). Quantitative analysis is complicated by shadowing and scattering effects. Crystallographic information can be gathered by the Electron BackScatter Diffraction (EBSD) method. Also here the geometrical constraints lead to some loss of accuracy. To circumvent this problem a chunk of material at the region of interest can be cut out and mounted to a free surface for investigation.

5.2.6 Three-dimensional imaging

The microstructure of materials in general is three-dimensional. In order to be able to characterize microstructures comprehensively it is therefore necessary to acquire three-dimensional images of them. The generation of a three-dimensional image always relies on some reconstruction step where information from many two-dimensional images is combined to create a three-dimensional (3d) representation. As explained in the previous subsection the FIB-SEM allows to expose a perfectly flat section from the interior of a material. Here we describe how a series of such images with a small fixed spacing can be acquired and processed into a 3d image of the microstructure.

Already in 1998 the development of a “dual focused beam apparatus” for this procedure was reported [35]. The apparatus was a FIB-SEM with a right angle between the two columns. This has the advantage that the SEM image of the freshly cut section will not be distorted as is the case in nowadays standard FIB-SEM systems.

The crucial steps of the procedure for acquisition of 3d data by FIB-SEM serial sectioning is illustrated in Fig. 5.12. First the region of interest is covered with a protection layer. Then three big trenches are cut to set free three sides of the cube to be imaged. The trenches on the sides act as sinks for sputtered material during the repeated sectioning of the cube. This helps to get clean section planes free from redeposited material. To minimize the occurrence of the waterfall effect within the imaged part of the sections rather deep cutting is helpful. After properly adjusting the focus of both electron and ion beam an automated procedure for the actual data acquisition is started. Repeatedly the ion beam removes a thin slice from the cube and then images the surface of the new section. Within

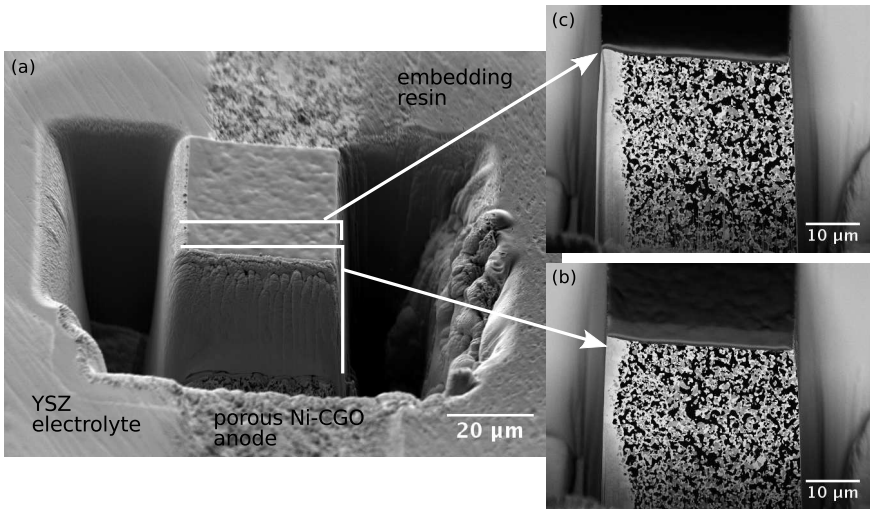


Figure 5.12: Procedure to acquire 3d data by FIB-SEM: (a) Cube is milled free by three trenches forming a U-shaped hole. Then a large milling box is placed to cut off thin sections from the cube. (b) After each milling step the fresh cut section is imaged. (c) More than 200 slices later, the section has moved upward within the fixed SEM image window.

8 hours one can easily produce large data sets, e.g. thousand 8bit grey level images with a resolution of one million pixels amount to a data set of 1 GB. The challenges that have to be mastered in order to acquire such data sets are multiple. The microscope stage has to be mechanically very stable to ensure that the region of interest doesn't drift away dozens of micrometers. There are systems that provide software, employing pattern recognition of a marker milled besides the region of interest, for automated drift correction. The section surface to be imaged by the SEM moves out stepwise from the electron column for each milled slice. Furthermore the section normal is not parallel to the electron beam. To obtain sharp images it is therefore necessary to increment the working distance of the electron beam after each slicing step and after completion of every scan-line within an image. Furthermore the section surface moves towards the top of the view field of the SEM, see Fig. 5.12(b) and (c). This can be compensated by shifting the area scanned by the SEM slightly upwards after each milling step. Ideally the spacing of the sections is set equal to the pixel size of the SEM images. As discussed in Sec. 5.2.5 the distortion along the y-axis should also be corrected already at the point of data acquisition. The

data set resulting for such settings has cubic voxels. Besides being utmost convenient for subsequent data processing this introduces only a minimal amount of anisotropy in the data set.

After acquisition of the raw data the stack of cross section images has to be processed in order to reconstruct the three-dimensional microstructure of the sample. For this purpose several commercial and open source programs are available. ImageJ is an open source software for which various plugins dedicated to 3d reconstruction exist [36]. A complete 3d image processing suite based on ImageJ and its plugins is available under the name Fiji [37]. The standard procedure is to crop the data set first such that as much image area as possible is filled with the cut sections in each image. Then the individual slices are aligned by maximizing the cross correlation between adjacent images. To check the result of this procedure a virtual section lying perpendicular to the physical section can be computed. Fig. 5.13(a) shows such an image before and Fig. 5.13(b) after alignment. For this example the StackReg plugin for ImageJ was used [38, 39]. The heavy distortion seen in Fig. 5.13(a) is due to the upward movement of the section during the process. The aligned stack shows no obvious distortion. Next the data is cropped again to get rid of the boundary regions where illumination is poor or redeposition or waterfall effect corrupt the data. Thereafter the image stack is ready for segmentation and quantitative analysis. The whole procedure described above has been termed FIB-nanotomography (FIB-nt) [40]. Volumes of some μm^3 to $10^4 \mu\text{m}^3$ can be imaged.

To get an impression of the spatial arrangement of the phases in a microstructure, inspection by eye of 3d visualizations can be used. Fig. 5.14 shows three different variants of visualization for one 3d data set. The simplest visualization shows three orthogonal slices through the set, see (a). Rendering of a properly illuminated surface mesh is quite expensive from the computational view point and requires accelerated graphics if real time

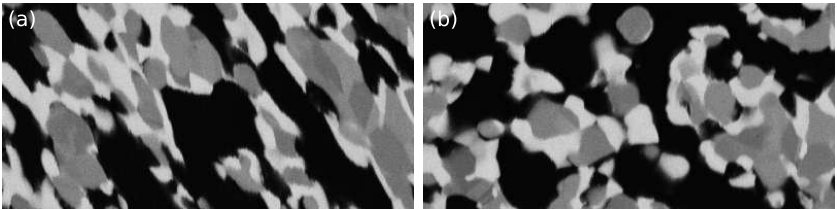


Figure 5.13: Images of computed sections perpendicular to actual slicing direction. (a) Before aligning of images, showing heavy distortion. (b) After alignment using StackReg plugin for ImageJ. The grains look isotropic and only slight jaggedness is present.

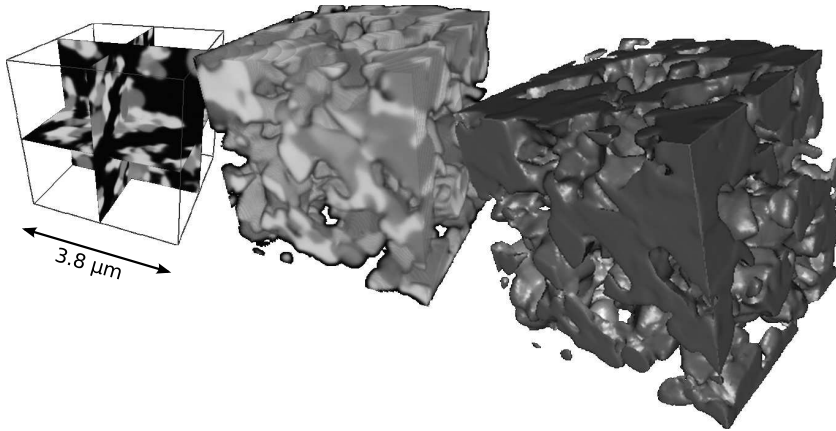


Figure 5.14: Three different types of visualization of one 3d data set: (a) orthoslices, (b) volume rendering and (c) mesh based surface rendering. Side length of the data cube is 400 voxels corresponding to $3.8\ \mu\text{m}$.

rotation of the object is desired, see (c). A good compromise is obtained by rendering a visualization from the voxels directly, see (b).

5.2.7 TEM lamella preparation

The maximal resolution achievable with a SEM is on the order of few nanometers at best. In a Transmission Electron Microscope (TEM) it is actually possible to reach atomic resolution. Furthermore the analytical possibilities are both more diverse and more accurate as compared to those at hand in a SEM. So there are good reasons to image samples in TEMs. Unfortunately in general the preparation of a suitable sample, called TEM lamella, is difficult and time consuming. The reason is that the sample thickness has to be 10 to 100 nm thin depending on the material. In TEM an electron wave is passed through the sample and the transmitted part of the wave is utilized for imaging and analysis. The classical methods of TEM lamella preparation rely on macroscopic methods: mechanical polishing and Ar ion milling with an unfocused beam. The work is tedious and the yield is low. Even worse it may not work at all, as in the case of composite materials with high contrast in hardness of the constituent phases. Another big drawback is that the site on the sample that finally can be inspected in the TEM cannot be chosen precisely. This problem is readily solved by FIB-based TEM lamella preparation. Fig. 5.15 shows the steps necessary to prepare a TEM lamella by the in-situ lift-out technique in a FIB-SEM equipped with a microma-

nipulator. First one locates a region of interest on the sample surface. Next a protection stripe of e.g. carbon is deposited. Two big trenches are milled such that a wall with a thickness of about $1\ \mu\text{m}$ separates them. Then the sample is tilted such that the FIB sees onto one side of the wall. One side

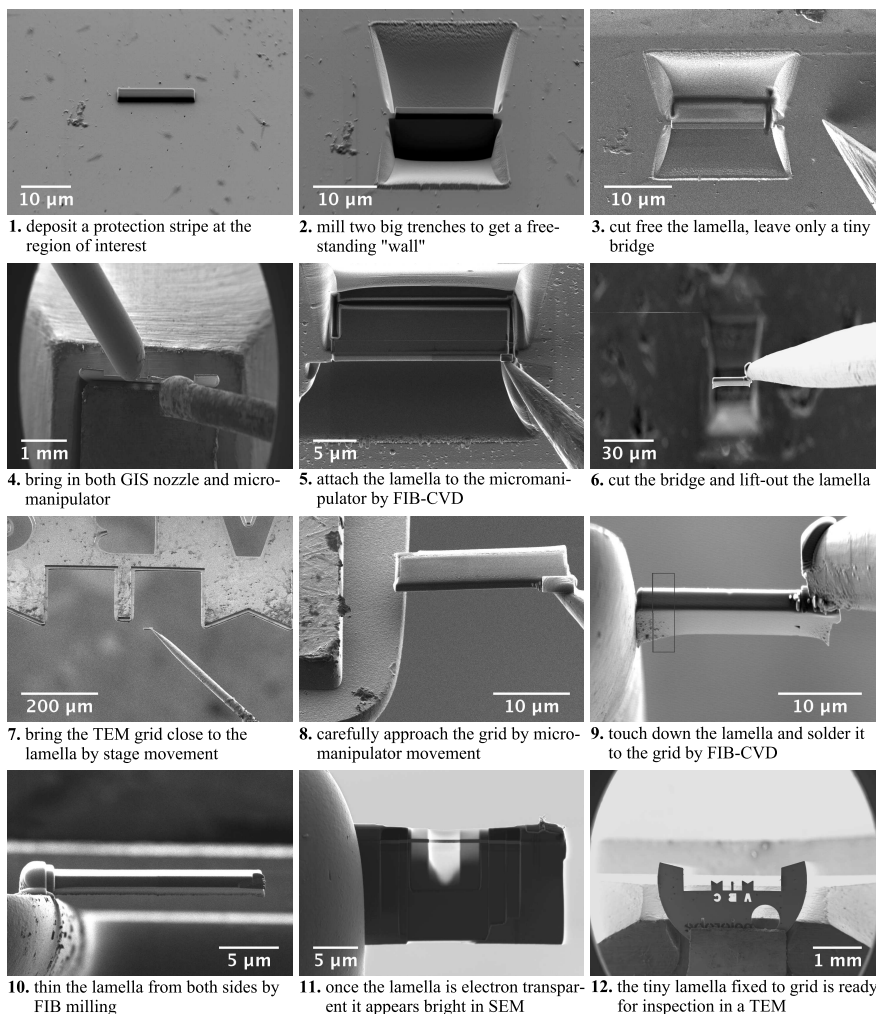


Figure 5.15: Step by step recipe for preparation of a TEM lamella by FIB in-situ lift-out technique. Detailed description of each step is given in the text. Note that the sample is kept in the coincidence point, micromanipulator and TEM grid are brought to it with micrometer precision.

and the bottom are cut completely through and on the other side a tiny bridge holding the lamella is left. Next the tip of a micromanipulator is brought into touch with the lamella. Then the GIS nozzle is injected to solder the tip to the lamella. At this moment four devices are positioned with micrometer accuracy to point exactly to the small piece of matter to be extracted and subsequently analyzed. Once the lamella is attached to the micromanipulator the bridge connecting the other side of the lamella to the sample is chopped. Rather than pulling out the lamella, the sample is moving away from the lamella in practice, because in order to be able to continue with the sample preparation procedure the lamella has to remain in the coincidence point. Next an appropriate TEM grid is brought in the vicinity of the TEM lamella. Using careful movement and the complementary information from the SEM and FIB images, the TEM lamella is placed on the grid and soldered to it by FIB-CVD. Then the manipulator tip is cut free, sharpened and retracted. At this point the lamella is still one micron thick. Mounted to the TEM grid it is now ready to be thinned down to a foil by FIB milling. The procedure is similar to that employed for preparation of a cross section. However, in this case the final polishing is even more important, as will be discussed below. Using the SEM it is possible to monitor the thinness of the foil. Regions of the foil that are electron transparent appear brighter than the rest when imaged using the Everhart-Thornley detector. This effect is due to the signal contribution of secondary electrons leaving the sample at the backside. They are produced by transmitted primary electrons. By careful milling it is possible to reach foil thickness below 50 nm on areas of about $1\ \mu\text{m}^2$. Thinner parts can be found in holey lamellae at the edges where the sample nearly has been milled away. Such lamellae do not look nice but may lead to superior results in TEM. As was mentioned earlier, irradiation of a solid by accelerated ions causes damage in the surface layer. This is also true when the ions hit the solid at grazing angle. The case of single crystalline silicon has been studied especially well. For Ga ions with an energy of 30 kV an amorphous surface layer with a thickness of 21 nm is observed [5]. Lowering the ion energy leads to a proportionate decrease of the thickness of the damage layer. Again for Si, 10 kV Ga ions produce an amorphous layer merely 8 nm thin. Therefore after a lamella has been thinned to transparency it is rewarding to carry out a so called “low kV showering”. The side wall of the lamella has to be tilted into the ion beam few degrees, since a low kV ion beam is less focused. Scanning from top to bottom a couple of times sputters the whole side wall gently. Thereby the damage layer produced during thinning is replaced by a new thinner one. Striving for better sample quality, ion columns are being tuned to provide focused ion beams of ever lower energy. High quality ion columns readily provide a setting for 1 kV Ga ions. Due to the larger incidence angle nec-

essary for showering the roughness of the sample surface is increased during low kV showering. Sample material and scientific question determine how much and which effort to enhance the quality of a TEM lamella is worth making. In case the inspection by TEM reveals that a lamella is too thick or covered by an unacceptably thick damage layer, it is possible to bring it back into the FIB and to do some extra polishing or low kV showering.

Preparation of TEM lamellae by FIB started in 1989 [8]. Since then many techniques to prepare a thin foil for TEM inspection have been developed. Prior to the introduction of the in-situ lift-out technique, described above, it was customary to actually pluck completely thinned and cut free lamellae with a glass capillary ex-situ. The lamella would jump to the shaft of the capillary and then be placed on a TEM grid with carbon foil. This technique has the drawback that the lamella cannot be repolished. Furthermore the yield of this technique depends heavily on the experience of the operator, whereas the in-situ lift-out technique seldom fails.

5.2.8 Preparation of samples for APT

The basic idea of Atom Probe Tomography (APT) is to exploit the highly curved electric field at a very sharp tip in order to create a magnified image of the tip. In modern APTs a pulsed laser is used to gate the field-evaporation of the tip. This makes sure that only one atom is evaporated at a time. Combined use of a position detector and a mass spectrometer yields a list with position and species for practically all atoms that were in the tip before evaporation. From this information a 3d image with atomic resolution and chemical information of the tip can be reconstructed. The volumes that can be investigated by APT are in the range of 10^4 to 10^6 nm³. The tips should have a diameter smaller than 100 nm. The traditional method to prepare such sharp tips is by electroetching. This method does not give control over the actual site where the tip is produced from. With the help of a FIB-SEM site specific tips for APT can be produced. Roughly one proceeds by cutting a prism of material from the desired location of the sample. Next this volume is transferred to a special sample holder with conical shape and a small area at the top. Using a micromanipulator and FIB-CVD the sample volume is mounted to the sample holder. The final preparation step is to shape the sample volume into a sharp tip suitable for evaporation in the APT.

5.3 Examples

We present four examples from materials science where the FIB-SEM is used. For each example the context is briefly introduced and then the experimental procedure and the findings are presented.

All FIB-SEM work presented in this section was performed on the Zeiss NVision 40 FIB-SEM workstation located at the Electron Microscopy Centre of ETH Zurich (EMEZ).

5.3.1 Inner surface of porous ceramic

Solid oxide fuel cells (SOFCs) are devices that convert chemical energy directly into electrical energy [41]. The fuel may be pure hydrogen or some small hydrocarbon such as methane or propane. The oxidant typically is air. The principle of fuel cells is that a gradient in oxygen partial pressure drives an ionic current through a solid electrolyte. The charge transfer caused by the ion current is compensated for by an electronical current. The electrical current provides the external consumer with power. Conventional SOFCs are built with two compartments: one for the fuel gas and one for the air. Placed between the compartments the electrolyte allows exchange of oxygen ions only. The weak point in such a design is the sealing of the gas compartments to prevent mixing of fuel and air. The most radical way to circumvent this issue surely is to employ one single compartment for both gases. Such a design is called single chamber SOFC. Experimentally it is found that single chamber SOFCs with conventional electrode materials have reasonable power output when running on fuel rich gas mixtures. The operation of such fuel cells relies on the selectivity of the cathode material employed [42]. At present no selective anode material is at hand.

A key step to improve the performance of single chamber SOFCs is the optimization of the electrode materials. The performance of a cathode depends on both its composition and its microstructure. The oxygen reduction reaction takes place at the gas-solid interface, thus the catalytic activity of a cathode is proportional to its surface area S . When comparing cathodes made from different compounds and showing varying microstructure it is necessary to normalize results by the respective surface areas. We here detail a procedure to determine the total surface area S of a porous $\text{Sm}_{0.5}\text{Sr}_{0.5}\text{CoO}_{3-\delta}$ (SSC) cathode sample. Details on the preparation and the electrochemical characterization of the sample are found in [43].

The sample consists of a porous thick film of SSC with a thickness $h = 50\text{ }\mu\text{m}$ and an area $A = 1\text{ cm}^2$ applied on top of a dense pellet of an oxygen ion conducting electrolyte ($\text{Zr}_{0.92}\text{Y}_{0.08}\text{O}_{1.96}$). The pore size is on the order of micrometers. Assuming that the microstructure of the sample is the same throughout the whole sample, the total surface area S can be estimated by

$$S = S_V V, \quad (5.1)$$

where $V = hA$ is the total volume of the sample and S_V is the specific surface area.

Fig. 5.16 shows a FIB cut cross section of the sample. By FIB-CVD a carbon stripe of $30 \times 4 \times 1 \mu\text{m}^3$ was deposited, then a large trench was milled with a current of 20 nA to a target depth of $20 \mu\text{m}$. The cross section was polished at a current of 2 nA yielding a reasonably flat surface. By eye it is easy to distinguish pores from the cut solid in this SEM image. In order to estimate the inner surface area we apply the *lineal intercept method* [44]. Generally information on microstructural quantities can be obtained by interceptions. These are lines where a test line is cut by a phase boundary. The total length L of the test lines is measured and the number of interceptions N is counted. In Fig. 5.16 the test lines are shown in black and the crossings from pore to solid or vice versa are indicated by white ticks. The unbiased estimator \hat{S}_V of the specific surface including an estimator for its standard deviation $\hat{\sigma}_{S_V}$ is given by the following expression

$$\hat{S}_V \pm \hat{\sigma}_{S_V} = \frac{2N}{L} \pm 4\sqrt{\frac{N}{2L^2}}. \quad (5.2)$$

For the image shown in Fig. 5.16 the total length of the test lines is $L = 23.4 \mu\text{m}$ and the number of crossings is $N = 45$. Thus we estimate that the

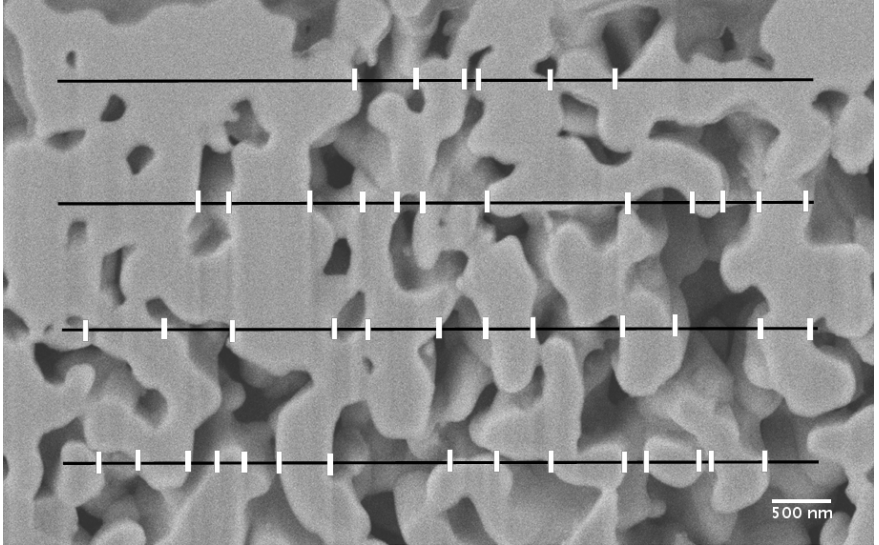


Figure 5.16: SEM image of a FIB cut cross section through a porous ceramic thick film used as cathode in single chamber solid oxide fuel cells. The crossings from solid to pore space encountered when following the lines are indicated by white ticks.

specific surface is $\hat{S}_V = 3.85 \pm 0.81 \mu\text{m}^{-1}$. Therefrom we get an estimate of $S = 19.2 \pm 0.4 \text{ mm}^2$ for the total surface area of the studied cathode sample.

In principle it would be possible to prepare materialographic sections of these samples by traditional means. Such a procedure is however much more time consuming than preparing FIB-cut cross sections on a not infiltrated sample as was done here. For detection of the pore surface by a computer program the present image quality would not be sufficient though. Filling of pore space with a resin would be needed in order to obtain properly segmentable images. From these the surface area could then be quantified by an image analysis program.

We here have demonstrated that FIB prepared sections of a porous solid yield images of sufficient quality for manual processing. This allows for instance to obtain a fairly accurate estimate of the specific surface of such samples at reasonable effort.

5.3.2 Spatially resolved chemical analysis of grain boundaries in alumina

Production of high purity alumina powder is a cost intensive process. Therefore new processing routes employing low cost raw materials are searched for. If such a new process shall be established on industrial scale it is necessary to prove that the product has the required quality. In case of alumina powder a crucial property is the sintering behavior and the resulting microstructure. In order to obtain high strength ceramics the material should be pore free and the grain size should be small and their size distribution should be narrow. In case such a powder does not densify at high sintering temperatures and e.g. develops anisotropic grain shapes then grain boundary analysis is helpful to find the reason. From literature it is known that silica (SiO_2) impurities may cause such effects. In order to prove that Si traces are present at grain boundaries high resolution chemical information across a representative grain boundary is required. TEM in combination with EDX can provide such information.

After localization of a suitable region with an elongated grain the sample was rotated such that the two grain boundaries became parallel to the y-axis in the FIB image, see Fig. 5.17(a). Comparing the SEM image (b) with the FIB image (a) one notices that the deposition stripe appears slightly rotated with respect to the horizontal direction in the SEM image (b). This is due to the slightly tilted sample surface. In the FIB image this cannot be seen since the sample is at right angles with the ion beam. Lift-out and mounting of the lamella was performed as described in Sec. 5.2.7. Since alumina has a very low sputter yield and the slope of FIB milled walls are rather shallow, the lamella was tilted into the beam by an angle of 1° .

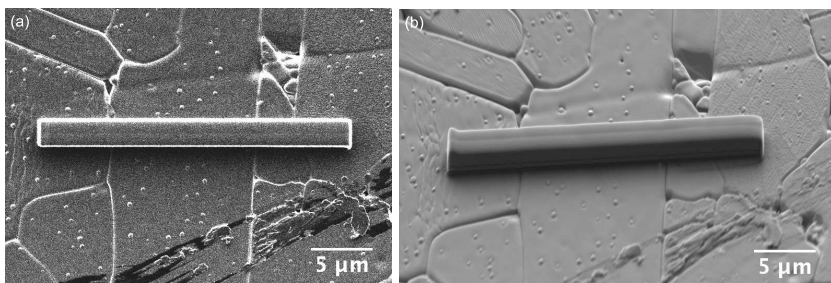


Figure 5.17: Surface of mechanically polished alumina sample. Images of protection stripe for preparation of a TEM lamella containing two particular grain boundaries. (a) SEM image, secondary electron signal. (b) FIB image, secondary electron signal. Both location and orientation of the lamella were tuned in order to have two grain boundaries within the lamella that are oriented perpendicular to the plane spanned by the lamella.

This allows to obtain approximately parallel FIB cut section planes on the front and back side. The final polishing was done with a current of 40 pA. Fig. 5.18 shows the mounted lamella as imaged by SEM with an electron beam accelerated at 5 keV for the primary electrons. Image (a) shows the secondary electron signal. The bright window in the left half of the lamella is electron transparent. It has an area of about $40 \mu\text{m}^2$, the thickness is estimated to be 150 nm. Image (b) shows the EsB signal. The dark grey region at the top end of the lamella is the remainder of the carbon deposit

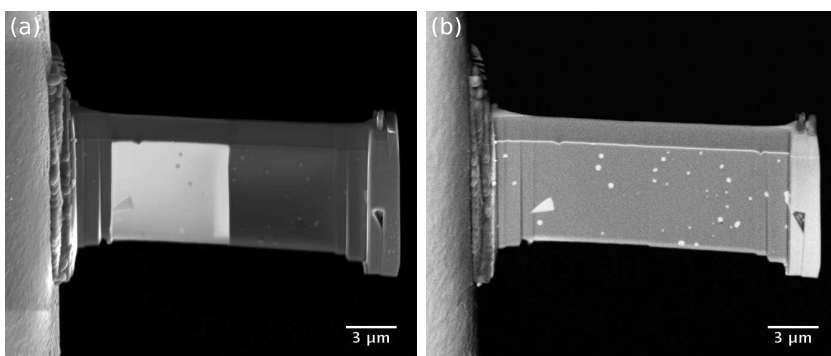


Figure 5.18: SEM micrographs of TEM lamella of Al_2O_3 sample mounted on grid. (a) SE2 signal, the bright area is the electron transparent region. (b) EsB signal, inclusions appear as bright phase.

serving as protection stripe. The thin bright line right below the protection stripe is platinum that was sputtered to the sample to make it conducting. The region with bright spots (inclusions) stems from the alumina sample.

Fig. 5.19(a) shows a High Angle Annular Dark Field (HAADF) Scanning Transmission Electron Microscopy image of the region at the grain boundary contained in the electron transparent window of the prepared lamella. The upper left corner, shown in black, is a part of the carbon protection stripe. The white line adjacent to it is the Pt coating. Three alumina grains and two of the inclusions are shown in the rest of the image. The inclusions displayed a massive Zr peak in their EDX spectrum taken from a spot analysis.

Fig. 5.19(b) shows a high resolution TEM image of a grain boundary between two alumina grains. Both grains show lattice fringes. The grain boundary was investigated further by two EDX line scans. One line is oriented perpendicular to the grain boundary and one aligned parallel to the grain boundary, see Fig. 5.20(a). The cumulative EDX spectrum from the line scan along the grain boundary shown in (b) displays a Si peak. In order to determine whether the Si is preferentially located at the grain boundary the elemental signal obtained for the line scan perpendicular to the grain boundary was computed, see (c). Interestingly the Al concentration drastically drops at the grain boundary. This behavior is also seen for the O signal. Both results give evidence for silica being segregated in the alumina grain boundaries.

We have shown that FIB preparation of a TEM lamella allows to precisely

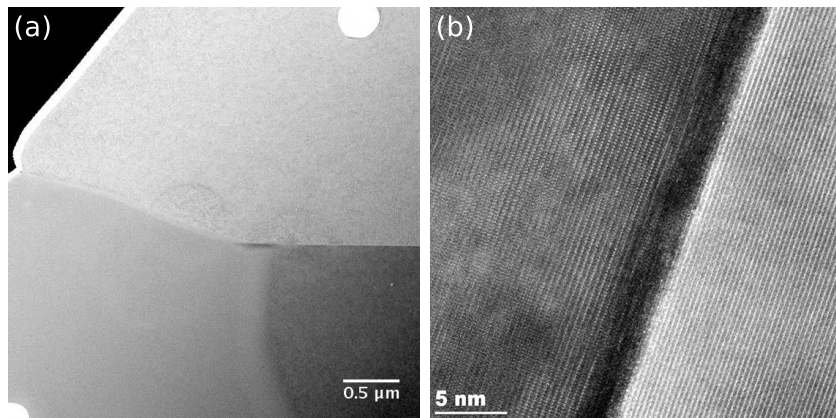


Figure 5.19: TEM micrographs of Al_2O_3 sample. (a) HAADF STEM image showing three adjacent grains and an inclusion on the upper right and bottom left partially. (b) High resolution TEM image of a grain boundary.

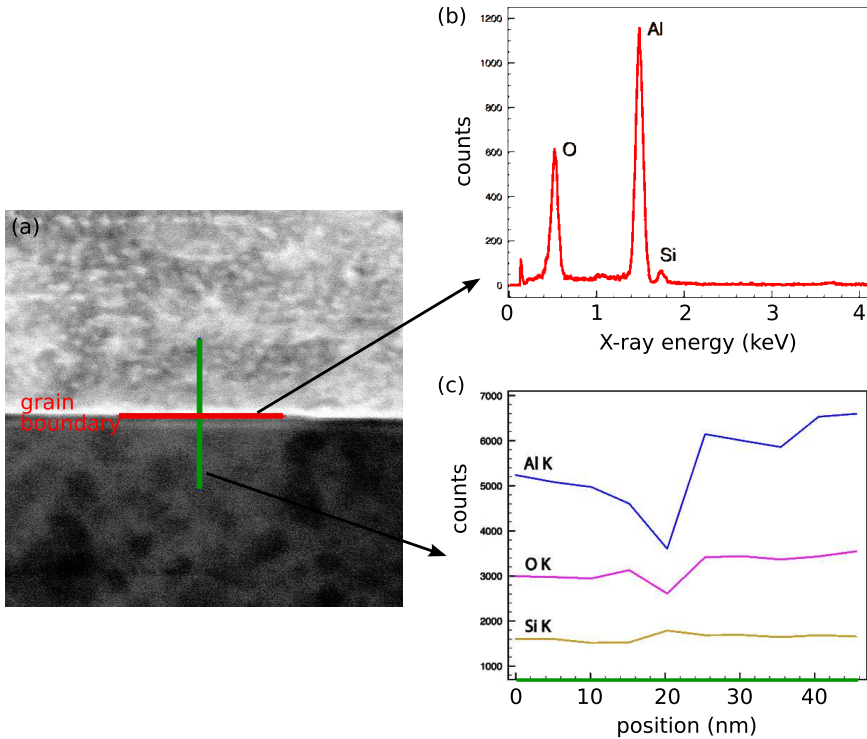


Figure 5.20: Results of EDX analysis of a grain boundary in an Al_2O_3 sample. (a) placement of two line scans, one parallel to the grain boundary, shown in red, and one across the grain boundary, shown in green. (b) Cumulative spectrum obtained from a line scan along the grain boundary. (c) Elemental signal obtained for line scan across the grain boundary.

choose a region of interest suitable for analyzing the distribution of chemical elements in the vicinity of grain boundaries by EDX analysis in a TEM. This is a prerequisite that cannot be met by conventional preparation techniques. The lateral resolution of the method is on the order of few nanometers and depends on the scattering cross section of the material and the thickness of the lamella.

5.3.3 Chemical analysis of impurity phase in TZP

The classical material for use as electrolyte in Solid Oxide Fuel Cells (SOFCs) is zirconia (ZrO_2) doped with varying amounts of yttria (Y_2O_3). The ad-

dition of yttria affects both the crystal structure and the concentration of oxygen vacancies. At a doping level of 8 mol % the oxygen ion conductivity is maximal. For a doping concentration of 3 mol % the best mechanical properties of the material are obtained. At this doping concentration the material is fully tetragonal, hence the name Tetragonal Zirconia Polycrystal (TZP). The grains have a size of about $0.3\text{ }\mu\text{m}$.

In connection with a study on the electromechanical properties of platinum thin films on various zirconia substrates, mechanically polished cross sections of commercial TZP tape were prepared. Unexpected dark spots were present on SEM micrographs of the TZP. Furthermore also some large pore clusters were found, see Fig. 5.21(a) and (b). The dark spots are seen especially well in images made using the EsB detector, see Fig. 5.21(b) and (c). A priori it is unclear whether the dark spots are due to some remainder from the mechanical polishing, i.e., SiC grains that get stuck in the TZP. To rule out this explanation a FIB cut cross section was prepared, see Fig. 5.21(c). Indeed the dark phase can be found below the polished surface, hence the SiC hypothesis cannot hold true. Consequently the TZP tape must contain a minor amount of a foreign phase that is well distributed and occurs in form of small inclusions.

In order to gather information that might reveal the origin of the inclusions, the chemical composition of the inclusions was inferred by an EDX analysis. A strong difference in the x-ray spectra from the inclusions and the matrix was found for a landing energy of 3 keV of the electron beam.

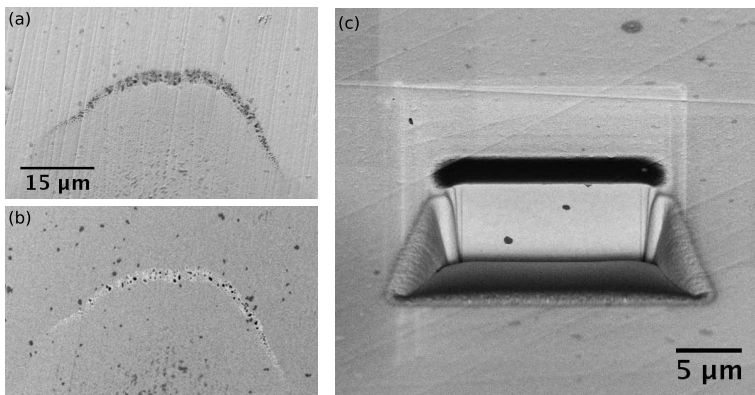


Figure 5.21: SEM images of mechanically polished cross section of TZP substrate. Surface with a large defect and inclusions. (a) Secondary electron image. (b) EsB image. (c) EsB image of FIB cut cross section, inclusions also occur below the mechanically polished surface, image shows EsB signal.

Fig. 5.22(a) shows the spectrum obtained from holding the electron beam on the matrix of the sample on the mechanically polished surface. The Zr $L\alpha$ and Y $L\alpha$ lines overlap strongly. The sample was coated with Pt to avoid charging. Unfortunately the Pt $M\alpha$ line overlaps exactly with the Zr $L\alpha$ peak. Only the Zr $L\alpha$ line could therefore be used to index the peak at 2 kV, thus the signal at 2 kV is composed of three signals due to the presence of Zr, Y and Pt. Fig. 5.22(b) shows the the spectrum obtained when holding the beam on an inclusion on the mechanically polished surface. A

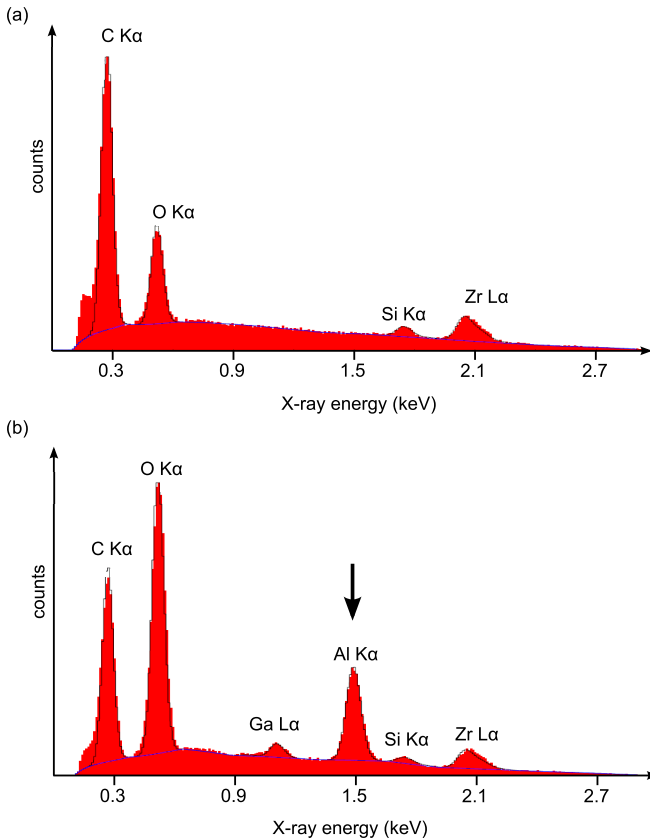


Figure 5.22: Spectra from EDX analysis obtained from two spots on TZP sample. (a) Spectrum from point analysis taken on the mechanically polished surface of the matrix phase (TZP). (b) Spectrum from point analysis taken on an inclusion. The arrow indicates the Al peak which is only present when collecting a spectrum on an inclusion.

very high new peak occurs at an energy of about 1.5 keV. This peak can be attributed to the presence of Al at the irradiated location. Furthermore the presence of Ga due to FIB scanning on this region is detected, see the peak at 1.1 keV. Surprisingly the peak at 2 keV, indexed by Zr $L\alpha$, is still present. This signal is therefore due to the Pt coating on the sample surface. An alternative hypothesis is that it is generated because the interaction volume of the electron beam exceeds the size of the inclusion. We remark that the relative intensity of the O $K\alpha$ and C $K\alpha$ peak is inverted with respect to the spectrum obtained on the matrix.

To prove that the inclusion seen in the cross section shown in Fig. 5.21(c) also contains Al an elemental mapping was performed on the portion of the cross section shown in Fig. 5.23(a). Image (b) shows the intensity of the Al $K\alpha$ signal, image (c) shows the intensity of the O $K\alpha$ signal and image (d) shows the intensity of the Zr $L\alpha$ signal. Apparently the inclusions contain a significant amount of Al compared to the matrix and are richer in O. The deficiency in the Zr $L\alpha$ signal indicates that the inclusions probably are composed of alumina (Al_2O_3). This is supported by the fact that the solubility of zirconia is very limited in alumina even in presence of yttria doping [45]. We conclude that the TZP contains few percent alumina in the microstructure as isolated inclusions.

We have shown that using EDX analysis with a low voltage accelerated

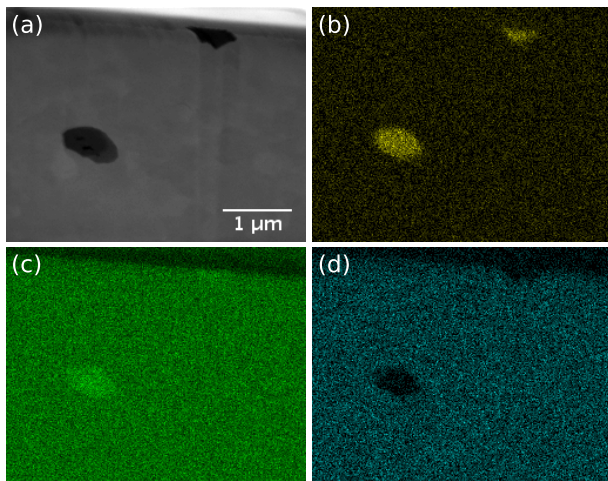


Figure 5.23: SEM micrographs of FIB polished cross section of TZP sample from Hexis. (a) Secondary electron signal. (b) Signal from Al $K\alpha$ -line, (c) O $K\alpha$ -line and (d) Zr $L\alpha$ -line.

beam in combination with a perfectly cut FIB cross section it is possible to determine the composition of a small amount of inclusions in a known matrix without other a priori knowledge. For the present case the spatial resolution of the EDX maps is extraordinarily good due to the low primary energy of the electrons used to excite the x-rays. For primary energies in the range of some tens of keV one cannot expect a resolution better than about one micrometer.

5.3.4 TiO_2 nanotubes with coatings

Titania (TiO_2) is a transparent oxide. Due to its high refractive index titania powder serves as white pigment in paint and sunscreen. Under UV light titania is a photocatalyst. The strong oxidative potential creates hydroxyl radicals in water, which gives titania its sterilizing and anti-fouling properties. Furthermore titania is a candidate for use in photovoltaic devices.

Titania nanotubes have a very large surface to volume ratio. This makes them interesting for photocatalytic application. In a collaboration with the Materials Chemistry group at Université de la Provence (Prof. Philippe Knauth) a series of different samples based on titania nanotubes produced by anodization in a dilute aqueous HF solution were investigated. Details of preparation of such titania nanotubes can be found in [46]. Three different types of samples were considered: a reference sample of titania nanotubes, titania nanotubes covered with CuInS_2 and titania nanotubes covered with Sn. The aim was to characterize the microstructure of the samples with topping in detail.

Fig. 5.24 shows micrographs of the reference sample. Image (a) shows a fractured cross section of the sample at a tilt angle of 54° to the surface. The lower half shows the Ti thin film and the upper half shows the titania nanotubes. The nanotubes have an outer diameter of 50 to 100 nm and a height of about 500 nm. The outer walls of the nanotubes are decorated with eight to ten brims each. Fig. 5.24(b) shows an SEM image of a FIB cut cross section. To protect the sensitive surface of the titania nanotubes the surface protection was applied in two steps. First a layer of carbon was deposited by electron beam induced CVD. This layer appears as dark cloud at the top of the titania nanotubes. Second a thick carbon layer was deposited by FIB-CVD. This layer appears as uniform gray square on top of the nanotubes. The cross section was polished with a gallium ion current of 20 pA. The strong corrugation of the cross section is due to the waterfall effect. The gallium ions are deflected by the tubes resulting in virtually no Ga ion flux below the walls of the tubes. Therefore these regions are hardly milled, whereas the other parts are milled strongly. The FIB cut cross section evidences that the nanotubes have a smooth inner surface. Note that the

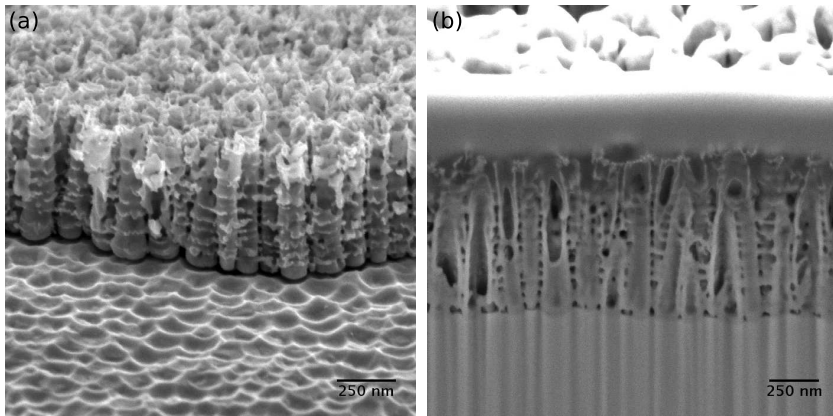


Figure 5.24: Reference sample: TiO₂ nanotubes grown from a Ti thin film on a Si substrate. The sample was coated with a sputtered Pt layer. (a) SEM image at 54° tilt of a rupture surface, secondary electron signal. (b) FIB milled cross section. The surface was covered with two layers of carbon, first electron beam, dark grey deposited then FIB deposited.

bright line at the top of the nanotubes is due to a Pt coating sputtered to the sample to prevent charging.

Micrographs from a cross section of the titania nanotube sample onto which CuInS₂ was sputtered are shown in Fig. 5.25. The protective coating was made the same way as described above for the reference sample, the final milling was also performed with a current of 20 pA. Image (a) was obtained using the secondary electron signal. The lower part of the nanotubes exhibits the same microstructure as the reference sample. At the top of the nanotubes a partially discontinuous layer is present. From the EsB signal an image with a stronger phase contrast is obtained, see Fig. 5.25(b). The bright phase at the top of the nanotubes is attributed to the CuInS₂. Apparently the nanotubes are not filled by the CuInS₂. It rather looks like the openings of the nanotubes are bridged by the sputtered material. The CuInS₂ forms a porous top layer with a grain size of some 10 to 20 nm.

The sample of TiO₂ nanotubes with Sn topping was produced by electrodeposition. Fig. 5.26 shows two overview micrographs of the resulting microstructure. Image (a) was obtained from the secondary electron signal. Micrometer sized pillars and blocks are attached on top a finely corrugated bottom layer. Image (b) was recorded from the EsB signal. The white phase is attributed to the Sn, whereas the gray phase shows the titania. Apparently the Sn is present in form of individual pillars and blocks. These pillars

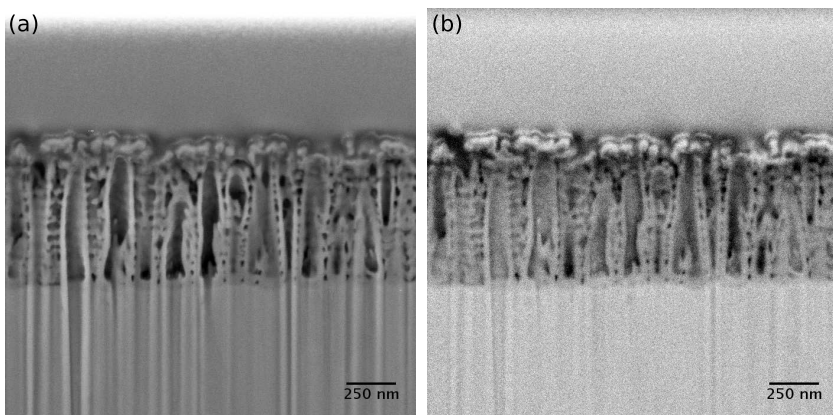


Figure 5.25: SEM micrographs of FIB cut cross section of TiO_2 nanotubes with sputtered CuInS_2 topping. (a) Secondary electron signal. (b) EsB signal.

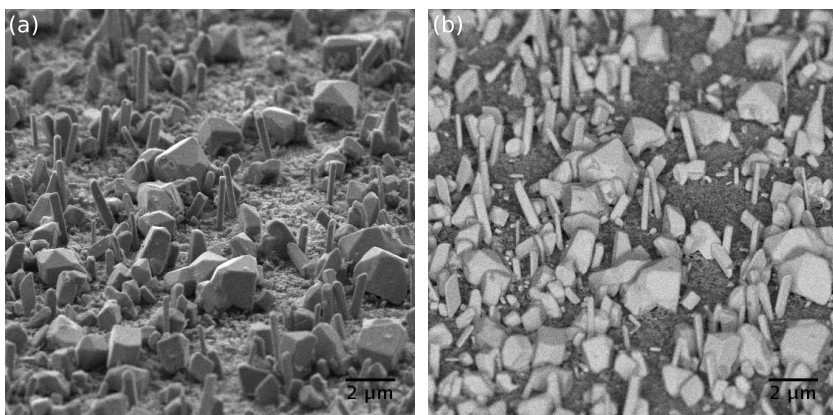


Figure 5.26: TiO_2 nanotubes after electrodeposition of Sn: SEM images of 54° tilted surface: (a) secondary electron signal and (b) EsB signal.

and blocks are evenly distributed on the length scale of tens of micrometers.

A cross section was prepared by FIB in order to investigate the interface between a Sn rod and the titania nanotubes. Fig. 5.27(a) shows an SEM image obtained from EsB signal after polishing with a current of 50 pA. A root of the Sn rod is located in the gap between the walls of two nanotubes. To follow the course of the root the polishing was continued and stopped

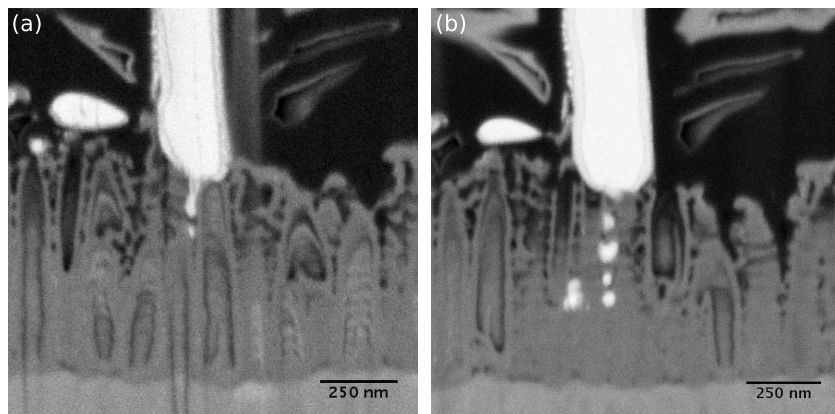


Figure 5.27: TiO_2 nanotubes after electrodeposition of Sn. SEM images from EsB signal of two tightly spaced FIB cut cross sections of a Sn rod (white phase). (a) First cross section. (b) Cross section after some further polishing.

manually as new parts of the root emerged, see (b). Apparently the root goes further down towards the Ti substrate.

The process of electrodeposition, used for preparation of the nanotubes, requires that an electric current flows. The deposition occurs at the interface of electronically conducting solid and electrolyte. Since titania is an insulator the Sn must start growing at the Ti thin film. Extrapolating the course of the Sn root seen in Fig. 5.25 we conclude that the gaps between the titania nanotubes form a pore network which connects down to the Ti substrate.

We have shown that CuIS_2 sputtered on top of titania nanotubes does not reach the interior of the nanotubes but rather forms a new film bridging the holes. Furthermore we found evidence that electrodeposition of Sn on top of the titania nanotubes starts at gaps between individual nanotubes, where the underlying Ti film is directly in contact with the electrolyte.

5.4 Summary and outlook

Focused Ion Beam Scanning Electron Microscopes (FIB-SEM) combine the capability to image and to tailor materials on the nanoscale. The ion beam serves mainly to mill and deposit material, whereas the electron beam is mostly used for imaging. The state of the art ion source, a gallium Liquid Metal Ion Source (LMIS), is characterized by its extreme brightness and an energy spread of about 5 eV. Using optimized lens systems a spot size of

the gallium beam of 10 nm is reached nowadays. Further reduction of the spot size can only be achieved if an ion source with lower energy spread is employed. Currently the extraction of ions from a laser-cooled atomic gas is proposed [47]. Such an Ultra Cold Ion Source (UCIS) would yield a beam with an energy spread of about 0.2 eV. This would allow to focus the beam to a spot size of about 1 nm. Furthermore such sources would offer a wide variety of ion species, ranging from the alkali metals to alkaline earth metals to noble gases.

In materials science the FIB-SEM can be applied for two different classes of applications. On the one hand it is used to image microstructures and on the other hand it allows to set up experiments at small length scales. We summarize the possibilities and limitations of the technology and discuss potential future developments.

In order to image the internal microstructure of materials a tool for precise cutting is necessary. FIB prepared cross sections have very low roughness and allow to image areas ranging from less than one μm^2 to about $10^3 \mu\text{m}^2$. The procedure is simple and fast. The lower limit of the pixel size is about 5 nm at best. From cross section images microstructural information is extracted by means of stereology. If the microstructure shall be characterized comprehensively the FIB-SEM can be applied to generate a stack of cross section images from which a three-dimensional image of the microstructure can be reconstructed. Such FIB-nanotomography (FIB-nt) allows to image volumes ranging from some μm^3 to about $10^4 \mu\text{m}^3$. Investigation of the microstructure of multi-phase thin films and semiconductor heterostructures is at the boarder or beyond the capabilities of today's best SEMs. The key limitation is the size of the interaction volume of electrons with energies in the range of some kV and a solid sample. A beam of focused He ions from a field emission source offers both a small spot size and a small interaction volume with solids [48]. Since 2007 this technology is commercialized through Zeiss SMT under the term Helium Ion Microscope (HIM). Besides a resolution of less than one nanometer such microscopes offer a very clear material contrast.

In materials science one is often interested in the distribution of a specific chemical species throughout the sample. At present the standard technology to infer chemical information from a sample is Energy Dispersive X-ray analysis (EDX). Spatial resolution is typically in the range of micrometers and quantification of concentration variations of few percent is already at the limits of this technology. There is a clear need to replace EDX with a more powerful technique in order to have better spatial resolution. For classical materials science the benefit would be that investigation of segregation phenomena could be done in a FIB-SEM without the need to resort to time consuming Transmission Electron Microscopy (TEM) studies. The use

of Time-of-Flight Secondary Ion Mass Spectrometry (TOF-SIMS) has been shown to provide a feasible solution to this problem [49]. Tescan provides a FIB-SEM equipped with a TOF-SIMS detector developed by TOFWERK.

The focus of much research in the field of material science is on the properties of very small entities of matter. Examples of such materials are nanoclusters, nanowires and nanotubes. The FIB-SEM offers an ideal platform to set up experiments to characterize physical properties of such materials. Apart from the capability to mill and deposit material at the nanometer scale the use of micromanipulators and microsensors round out the FIB-SEM to what has been termed a “nanolaboratory”. Micromanipulator manufacturer Kleindiek has invented various helpful tools to enable simpler experimentation at the nanoscale. To equip micromanipulators with more functionality they provide grippers to hold small solids and capillaries to locally deliver fluid, e.g. an electron beam curable glue. Furthermore platforms integrating micromanipulators with Atomic Force Microscopes (AFM) and electrical micro four point probes are commercialized.

Special sample stages that allow to control the temperature of the sample have been used in SEM and TEM for a while. At present effort is made to bring such equipment into FIB-SEM systems as well. Using a cryo-stage it is possible to investigate hydrated samples, e.g. soil or rock samples, as well as radiation sensitive soft materials such as polymers. Heating stages allow to investigate in detail the evolution of microstructures during heat treatment.

The concept of FIB-SEM has proven to be of outstanding value both in industrial metrology as well as basic research. Limitations in spatial resolution are likely to be overcome with the next generation technologies for ion beams providing solutions for milling as well as imaging. However, at present a perspective for a technology that would allow for materials deposition in the nanometer regime has still to come.

Acknowledgements

This chapter contains results from work to which several people have contributed either by providing samples or conducting further investigations as well as with helpful discussions. The author would like to thank all of them cordially!

The alumina samples with zirconia inclusions were prepared by Meike Schlupp, from the Nonmetallic Inorganic Materials group (NMW) at ETH Zurich and TEM and STEM images were recorded by Ashley Harvey, also NMW, with the Tecnai F30 located at the Electron Microscopy center of ETH Zurich (EMEZ). The SOFC cathode samples were prepared by Brandon B rger, NMW. The porous Ni-CGO cermets used as SOFC anodes

were provided by Hexis AG, the heat treatment including reduction was done by Henning Galinski, NMW. The TZP substrates were also provided by Hexis AG, the mechanical cross sections were prepared by Johannes Keppner, NMW. The EDX analysis of the TZP sample was done with helpful input from Karsten Kunze from EMEZ. Romain Cayzac from the Materials Chemistry group at Université de la Provence at Marseilles prepared the samples of titania nanotubes.

The author would like to thank Dr. Marco Cantoni, Centre Interdisciplinaire de Microscopie Électronique at EPFL, for many valuable lessons in the field of electron microscopy. Philippe Gasser from EMEZ is acknowledge for keeping the “NV” running and for his valuable advice on FIBbing. Finally EMEZ is acknowledged for providing technical support and covering the running costs of the Zeiss NVision 40 FIB-SEM workstation.

Glossary

AFM Atomic Force Microscope, a flat tip attached to a cantilever is rastered over a sample surface, force and position are read out to give various sorts of maps, different operating modes exist: contact, non-contact and tapping

apertured cathode metal plate biased with respect to the LMIS in order to extract ions from it

aperture stripe metal plate with several holes used to reduce the diameter of an electron (ion) beam for adjusting the beam current

APT Atom Probe Tomography, controlled field-evaporation of the atoms one by one from a fine tip, detection of position and mass spectrometry is used to generate a 3d reconstruction with atomic resolution and chemical information of the evaporated tip

BSE Back-Scatter Electrons, produced by high angle scattering of primary electrons hitting a solid, the BSE signal contains elemental information

coincidence point location where both electron and ion beam meet in a FIB-SEM

condenser lens first lens in an optical system used to generate a collimated beam from a point source, plays a role to adjust the beam current

EBSD Electron BackScatter Diffraction, system of detector and software used to obtain crystallographic information from the diffraction pattern created by an electron beam hitting the solid

EDX Energy Dispersive X-ray analysis, system of detector and software used to obtain chemical information from x-rays generated by an electron beam interacting with a solid

EsB detector Energy selective Backscatter electron detector, detector design patented by Zeiss using an in lens detector in a Gemini electron column in order to select a certain window of the BSE electrons generated by the primary beam

FEI US company producing and selling electron microscopes and focused ion beam systems, <http://www.fei.com/>

FIB-CVD Focused Ion Beam induced Chemical Vapor Deposition, through the GIS a precursor gas is delivered to the sample surface where it adsorbs, ion induced decomposition of the adsorbed precursor molecules yields deposition of a solid on the sample

FIB-nt FIB nanotomography, procedure of slicing and imaging repeatedly a sample in order to produce a stack of images from which a 3d image with resolution in the nanometer scale can be reconstructed

HAADF High Angle Annular Dark Field, detector mode used in STEM to obtain elemental and density contrast

HIM Helium Ion Microscope, a beam of He ions is produced by field ionization at a three atoms sharp tip held at cryogenic temperature, achievable resolution is claimed to be about 0.3 nm

Hitachi High-Tech Japanese company selling electron microscopes and focused ion beam systems, <http://www.hitachi-hitec.com/global/em/index.html>

FIB Focused Ion Beam, a finely focused beam of ions, typically Ga^+

FWHM Full Width at Half Maximum, measure of breadth for bell type curves

gas nozzle final tube of GIS, can be moved with pneumatics to approach the coincidence point by about 200 μm

GIS Gas Injection System, heatable crucibles and tube system capable to deliver a local gas atmosphere at the coincidence point

JEOL Japanese company producing and selling electron microscopes and focused ion beam systems, <http://www.jeol.com/>

Kleindiek German company providing add-ons for sample manipulation in high vacuum, <http://www.kleindiek.com>

LMIS Liquid Metal Ion Source, device providing an ion beam from a spot of extreme brightness, a molten metal is field evaporated at the apex of a Taylor-Gilbert cone

micromanipulator system of piezo actuators capable to move a tungsten whisker with sub-nanometer precision, the whisker can be used to move small objects on a sample while watching with the microscope

Orsay Physics French company producing focused ion beam and focused electron beam columns and GIS systems, <http://www.orsayphysics.com/>

pole piece last part of electron (ion) column, it guides the electrical field for the objective lens of the column, i.e., the lens used to focus the beam

SEM Scanning Electron Microscope, digital microscope based on a finely focused electron beam that is scanned over a small area of a sample held in high vacuum

SII NanoTechnology Inc. Japanese company selling electron microscopes and focused ion beam systems, <http://www.siint.com/en/>

SIM Scanning Ion Microscopy, imaging mode in a FIB system using the secondary ion signal generated by a scanning ion beam

sputtering physical process of material removal from a solid through transfer of momentum and energy from a particle beam hitting the surface of the solid

STEM Scanning Transmission Electron Microscope, similar to TEM but the image is created by scanning a focused electron beam over an electron transparent sample, this technique provides extended analytical capabilities as compared to TEM

TEM Transmission Electron Microscope, system of electrical lenses, sample holder and camera used to produce micrographs with a resolution down to the atomic scale, the image is created by passing an electron wave through an electron transparent sample

TEM lamella thin foil prepared from a sample and attached to a standard TEM grid of 3 mm diameter, suitable for inspection in a TEM or STEM

Taylor-cone shape of the fluid in a special solution of electrohydrodynamics first published by G. I. Taylor

Taylor-Gilbert cone cone formed by a fluid when exposed to an intense electrical field

Tescan Czech company producing and selling electron microscopes and focused ion beam systems <http://www.tescan.com/>

TOFWERK Swiss company producing and selling time-of-flight mass spectrometers, <http://www.tofwerk.com/cms/index.php>

UCIS Ultra Cold Ion Source, concept for a new ion source: the ion beam is produced by just-above threshold photo-ionization of laser-cooled atoms held in a magneto-optical trap

working distance distance from pole piece to focal point of electron (ion) beam

Zeiss SMT German company producing and selling electron microscopes and focused ion beam systems, <http://www.zeiss.com/smt>

Bibliography

- [1] R. Feynman, "There's plenty of room at the bottom," *Engineering and Science*, vol. 23, no. 5, pp. 22–36, 1960.
- [2] P. D. Prewett and G. L. R. Mair, *Focused ion beams from liquid metal ion sources*. John Wiley & Sons Inc., 1991.
- [3] J. Orloff, M. Utlaut, and L. W. Swanson, *High resolution focused ion beams: FIB and its applications*. Kluwer Academic, 2003.
- [4] L. A. Giannuzzi and F. A. Stevie, eds., *Introduction to Focused Ion Beams: Instrumentation, Theory, Techniques and Practice*. Springer, 2005.
- [5] N. Yao, ed., *Focused ion beam systems: Basics and applications*. Cambridge University Press, 2007.
- [6] J. Melngailis, "Critical review: Focused ion beam technology and applications," *J. Vac. Sci. Technol. B*, vol. 5, no. 2, pp. 469–495, 1987.
- [7] S. Reyntjens and R. Puers, "A review of focused ion beam applications in microsystem technology," *J. Micromech. Microeng.*, vol. 11, pp. 287–300, 2001.

- [8] M. Sugiyama and G. Sigesato, “A review of focused ion beam technology and its applications in transmission electron microscopy,” *J. Electron Microsc.*, vol. 53, no. 5, pp. 527–536, 2004.
- [9] C. A. Volkert and A. M. Minor, “Focused ion beam microscopy and micromachining,” *MRS Bull.*, vol. 32, pp. 389–399, 2007.
- [10] J. Gierak, “Focused ion beam technology and ultimate applications,” *Semicond. Sci. Technol.*, vol. 24, no. 4, p. 043001, 2009.
- [11] *Workshop: Exakte Zielpräparation und 3D-Werkstoffanalyse in der Praxis*, February 2006. Saarbrücken, Germany.
- [12] J. Reuteler, “Introduction to FIB-SEM: Basic physics and applications.” Nonmetallic Inorganic Materials, ETH Zurich, Switzerland, http://www.nonmet.mat.ethz.ch/Infrastructure/FIB/FIB-SEM_Introduction_JR.pdf, 2008.
- [13] R. G. Forbes, “Understanding how the liquid-metal ion source works,” *Vacuum*, vol. 48, no. 1, p. 85, 1997.
- [14] W. Gilbert, *De Magnete*. London, 1600. Book 2, Chapter 2.
- [15] L. Rayleigh, “On the equilibrium of liquid conducting masses charged with electricity,” *Philos. Mag.*, vol. 14, pp. 184–186, 1882.
- [16] A. Gomez and K. Tang, “Charge and fission of droplets in electrostatic sprays,” *Phys. Fluids*, vol. 6, pp. 404–414, 1994.
- [17] J. Zeleny, “Instability of electrified liquid surfaces,” *Phys. Rev.*, vol. 10, no. 1, pp. 1–6, 1917.
- [18] J. Zeleny, “The electrical discharge from liquid points, and a hydrostatic method of measuring the electric intensity at their surfaces,” *Phys. Rev.*, vol. 3, no. 2, p. 69, 1914.
- [19] G. I. Taylor, “Disintegration of water drops in an electric field,” *Proc. Roy. Soc. Lond.*, vol. A 280, p. 383, 1964.
- [20] V. E. Krohn and G. R. Ringo, “Ion source of high brightness using liquid metal,” *Appl. Phys. Lett.*, vol. 27, no. 9, pp. 479–481, 1975.
- [21] R. Clampitt, K. L. Aitken, and D. K. Jefferies, “Intense field-emission ion source of liquid metals,” *J. Vac. Sci.*, vol. 12, p. 1208, 1975.
- [22] R. Clampitt and D. K. Jefferies, “Miniature ion sources for analytical instruments,” *Nucl. Instrum. Methods*, vol. 149, pp. 739–742, 1978.

- [23] P. Grivet and A. Septier, "Ion microscopy: history and actual trends," *Ann. N.Y. Acad. Sci.*, vol. 306, pp. 158–182, 1978.
- [24] R. L. Seliger, J. W. Ward, V. Wang, and R. L. Kubena, "A high-intensity scanning ion probe with submicrometer spot size," *Appl. Phys. Lett.*, vol. 34, pp. 310–312, 1979.
- [25] L. W. Swanson, "Liquid metal ion sources: mechanism and applications," *Nucl. Instrum. Methods*, vol. 218, pp. 347–353, 1983.
- [26] G. Benassayag and P. Sudraud, "In situ high voltage TEM observation of an electrohydrodynamic (EHD) ion source," *Ultramicroscopy*, vol. 16, pp. 1–8, 1985.
- [27] R. L. Seliger, R. L. Kubena, R. Olney, J. Ward, and V. Wang, "High-resolution ion-beam process for microstructure fabrication," *J. Vac. Sci. Technol.*, vol. 16, no. 6, pp. 1610–1612, 1979.
- [28] S. B. Cronin, Y.-M. Lin, O. Rabin, M. R. Black, J. Y. Ying, M. S. Dresselhaus, P. L. Gai, J.-P. Minet, and P.-P. Issi, "Making electrical contacts to nanowires with a thick oxide coating," *Nanotechnol.*, vol. 13, pp. 653–658, 2002.
- [29] C. Y. Nam, J. Y. Kim, and J. Fischer, "Focused-ion-beam platinum nanopatterning for GaN nanowires: Ohmic contacts and patterned growth," *Appl. Phys. Lett.*, vol. 86, p. 193112, 2005.
- [30] P. J. W. Moll, R. Puzniak, F. Balakirev, K. Rogacki, J. Karpinski, N. D. Zhigadlo, and B. Batlogg, "High magnetic-field scales and critical currents in SmFeAs(O,F) crystals," *Nat. Mat.*, vol. 9, pp. 628–633, 2010.
- [31] K. J. Hemker and W. N. J. Sharpe, "Microscale characterization of mechanical properties," *Annu. Rev. Mater. Res.*, vol. 37, pp. 93–126, 2007.
- [32] A. Dubach, R. Raghavan, J. F. Löffler, J. Michler, and U. Ramamurty, "Micropillar compression studies on a bulk metallic glass in different structural states," *Scr. Mater.*, vol. 60, pp. 567–570, 2009.
- [33] F. Sulser, G. poberaaj, M. Koechlin, and P. Günter, "Photonic crystal structure in ion-sliced lithium niobate thin films," *Opt. Express*, vol. 17, pp. 20291–20300, 2009.
- [34] R. Spolenak, L. Sauter, and C. Eberl, "Reversible orientation-biased grain growth in thin metal films induced by a focused ion beam," *Scripta Mater.*, vol. 53, pp. 1291–1296, 2005.

- [35] T. Sakamoto, Z. Cheng, M. Takahashi, M. Owari, and Y. Nihei, “Development of an ion and electron dual focused beam apparatus for three-dimensional microanalysis,” *Jpn. J. Appl. Phys.*, vol. 37, pp. 2051–2056, 1998.
- [36] W. S. Rasbad, “ImageJ.” U. S. National Institutes of Health, Bethesda, Maryland, USA, <http://imagej.nih.gov/ij/>, 1997-2011.
- [37] “Fiji is just imagej.” <http://fiji.sc/Fiji>.
- [38] P. Thévenaz, U. E. Ruttimann, and M. Unser, “A pyramid approach to subpixel registration based on intensity,” *IEEE Trans. Image Process.*, vol. 7, pp. 27–41, 1998.
- [39] P. Thévenaz, “An ImageJ plugin for the recursive alignment of a stack of images.” Biomedical Imaging Group, EPF Lausanne, Switzerland, <http://bigwww.epfl.ch/thevenaz/stackreg/>.
- [40] L. Holzer, F. Indutnyi, Ph. Gasser, B. Münch, and M. Wegmann, “Three-dimensional analysis of porous BaTiO₃ ceramics using FIB nanotomography,” *J. Microsc.*, vol. 216, pp. 84–95, 2004.
- [41] R. O’Hayre, S.-W. Cha, W. Collela, and F. B. Prinz, *Fuel cell fundamentals*. Wiley, 2nd ed., 2009.
- [42] I. Riess, “On the single chamber solid oxide fuel cells,” *J. Power Sources*, vol. 175, pp. 325–337, 2008.
- [43] B. E. Bürgler, *Single chamber solid oxide fuel cells*. PhD thesis, ETH Zurich, Switzerland, 2006.
- [44] J. Ohser and F. Mücklich, *Statistical Analysis of Microstructures in Materials Science*. John Wiley & Sons Inc., 2000.
- [45] S. Lakiza, O. Fabrichnaya, M. Zinkevich, and F. Aldinger, “On the phase relations in the ZrO₂–YO_{1.5}–AlO_{1.5} system,” *J. Alloys Compd.*, vol. 420, pp. 237–245, 2006.
- [46] G. F. Ortiz, I. Hanzu, P. Knauth, P. Lavela, J. L. Tirado, and T. Djenezian, “TiO₂ nanotubes manufactured by anodization of Ti thin films for on-chip li-ion 2D microbatteries,” *Electrochim. Acta*, vol. 54, pp. 4262–4268, 2009.
- [47] M. P. Reijnders, *Ion beams from laser-cooled gases*. PhD thesis, Technical University Eindhoven, 2010.

- [48] B. W. Ward, J. A. Notte, and N. P. Economou, “Helium ion microscope: A new tool for nanoscale microscopy and metrology,” *J. Vac. Sci. Technol. B*, vol. 24, pp. 2871–2874, 2006.
- [49] M. Ishihara, S. Ebata, K. Kumondai, R. Mibuka, K. Uchino, and Y. H., “Ultra-high performance multi-turn FOF-SIMS system with a femto-second laser for post-ionization: investigation of the performance in linear mode,” *Surf. Interface Anal.*, vol. 42, pp. 1598–1602, 2010.

Chapter 6

Conclusions and outlook

This thesis addresses the relation between the microstructure and the effective electrical conductivity of metal-insulator composites. In contrast to the classical mixing rules and percolation theory, which are based on assumed microstructures, this work is based on detailed real-space micrographs of the microstructure of composite materials. The aim was to explore the possibilities offered by image analysis in order to derive information on the effective conductivity directly from the microstructure. The practical advantage of this approach is the low computational cost as compared to the conventional route which relies on computation of the solutions of complex boundary value problems. From the theoretical point of view the implicit nature of the conventional route is unsatisfactory, as it obscures the relation between microstructure and effective properties.

We developed an image filter, called backbone filter, for two-dimensional metal-insulator composites for reducing the spatial complexity of the boundary value problem that describes steady state conductivity through the metal phase. This allows to reduce the computational cost of numerical studies substantially. However, our result cannot be generalized in a straight forward manner to the case of three-dimensional space. The skeleton by influence zones, which is the main ingredient of our backbone filter, can't identify current carrying structures in three-dimensional space. For structures that contain no watersheds, such as rods connected to all six faces of a cubic image, the skeleton by influence zones gets empty. A pragmatic implementation of a backbone filter for three-dimensional images could be based on truncating its skeleton. The backbone within the skeleton, required to be one voxel wide, then would be its bi-connected part [1].

In order to search for microstructural quantities that could be used besides the volume fraction as additional input for mixing rules, we generated

images representing networks formed by spherical particles from composites, composed of copper particles in an insulating polymer matrix, serving as templates. For these model metal-insulator microstructures we identified the number of loops (second Betti number) to correlate quantitatively with the effective conductivity as estimated by a random walk technique. This shows that topological measures may serve to refine classical mixing rules. Compared to higher order correlation functions, which occur in bounds of effective properties obtained from homogenization, the number of loops can be computed by efficient and comparably simple algorithms. For structures with a large variation of the effective cross sectional area of individual current carrying paths with respect to each other the geometry must be accounted for as well. A first attempt could be to define a width-weighted number of loops.

A yet open but rather basic question concerns the form in which the microstructure can be related to effective transport properties. The above discussed ideas are based on the assumption that certain global or averaged geometrical and topological characteristics of a microstructure determine its effective properties. Another approach can be derived from Eq.(2.5), which expresses the effective conductivity as integral of the squared norm of the current density over the conducting phase. This expression in principle is a weighted area (volume) measure of the conducting phase. The question is whether these weights may be approximated by means of a sequence of image filters. On the metal clusters that are isolated from the percolating clusters the weights are surely zero. Therefore the first member of the sequence of filters has to be the extraction of the percolating cluster. Within dead ends the weights must be very close to zero according to our findings using the backbone filter, which thus might become the second member. Next subsets of the backbone characterized by similar current density must be identified. Both length and width of current carrying paths play a role. Inspired by the idea of the “red bond” from percolation theory, the last member of the new image filter sequence might be one that extracts those parts of the structure that are necessary for its percolation and are characterized by an extraordinarily high ratio of length to width (cross sectional area).

For many practical problems, e.g. diffusion of radioactive isotopes through soil or heat conduction in microchips, estimates or bounds of the effective transport properties are sufficient. In fact a major part of the results from homogenization concern bounds of effective properties. For the case of conductor-insulator composites unfortunately all the lower bounds from homogenization are trivial. This is both inconvenient and somewhat unexpected, since the existence of a percolating cluster within the conducting phase guarantees nonzero effective transport properties. A simple idea to obtain a lower bound is to determine the length and width of a rod that passes

the conducting phase. Care must be taken on how to treat microstructures with many thin parallel paths. A notion of non-intersecting paths may be required to solve this issue.

The random walk technique employed in Chp. 3 (concerned with transport through three-dimensional networks) has the potential to handle situations with coupled transport and complex geometries of sources and sinks, e.g. as they occur in the case of fuel cells. In order to reduce the computational effort a simplification of the microstructure by an image filter similar to the backbone filter could be incorporated. We anticipate that this coupled approach would yield a method capable of handling sample sizes that are beyond the capabilities of the finite element method.

A problem that is relevant to microelectronics industry is heat transport through microchips. Especially in three-dimensionally stacked chips the heat dissipation becomes problematic and cooling is required. Although the microstructure, i.e., the chip layout, is completely known, its complexity is beyond the capabilities of simulation methods. Hence approaches from the theory of heterogeneous materials are being explored to check whether the implemented cooling strategies are sufficient [2]. If a detailed understanding of the relation between microstructure and effective transport was at hand, a direct optimization of the transport paths could be performed. To validate the result the above mentioned random walk approach could be employed. The example of electrical transport within a two dimensional current collector, studied in Chp. 4, shows that complex source geometries are beyond intuition and the most simple ideas on how current flows. A thorough quantitative analysis is required to account for the effects of interaction between different sources, which can lead to mutual obstruction.

The space of all possible microstructures and the structure induced by effective properties is still not well understood and described. The mathematical treatment of complex spatial structures was pioneered by Mathéron [3]. Together with Serra he developed mathematical morphology [4]. Since then the spatial structure of solids has been studied within several disciplines [5, 6]. However, a unifying theory is still lacking. We believe that there is big potential in various fields of mathematics, yet to be explored regarding the description of complex spatial structures. Unfortunately progress is slow due to the gap in terms of language between the relevant fields of mathematics and applied sciences, like materials science. Attempts to bridge this gap in order to accelerate progress have been undertaken [7], but are scarce.

The next generation of microscopes will generate microstructural information with unprecedented resolution and quality. We are convinced that tools from a wide range of mathematical disciplines are suited for the analysis of spatial structures in order to advance the interesting field of relations between microstructures and effective properties.

Bibliography

- [1] S. Kirkpatrick, “The geometry of the percolation threshold,” *AIP Conf. Proc.*, vol. 40, pp. 99–117, 1978.
- [2] T. Brunschwiler, G. Töral, S. Paredes, and B. Michel, “Multi-scale sub-domain and porous media modeling of conjugate heat and mass transfer in interlayer-cooled 3D-chip stacks,” in *Abstract book Transpore 2010*, 2010.
- [3] G. Mathéron, *Random sets and integral geometry*. Wiley, New York, 1975.
- [4] J. Serra, *Image analysis and mathematical morphology*. Academic Press, London, 1982.
- [5] K. R. Mecke and D. Stoyan, eds., *Statistical physics and spatial statistics: the art of analyzing and modeling spatial structures and pattern formation*. No. 554 in Lecture Notes in Physics, Springer, Berlin, 2000.
- [6] K. Mecke and D. Stoyan, eds., *Morphology of condensed matter: Physics and geometry of spatially complex systems*. No. 600 in Lecture Notes in Physics, Springer, Berlin, 2002.
- [7] J. Ohser and F. Mücklich, *Statistical Analysis of Microstructures in Materials Science*. John Wiley & Sons, Ltd., 2000.

Appendix A

Transport properties

This appendix deals with theoretical aspects of transport in heterogeneous materials. In the first section the term “transport properties” is defined precisely. The second section concerns the concept of effective properties. In the third section we discuss the relation between diffusion and random walks. Finally we detail in the fourth section a particular random walk technique that is suited for estimating the effective transport property from a binary image.

A.1 Transport properties: a class of physical properties

Physical properties of materials are generally classified according to the different disciplines within physics. Mechanical, electrical, magnetic and optical properties are distinguished. From the mathematical point of view another classification is natural: physical properties are grouped by the type of differential equation that describes them [1]. The value of this classification is that results obtained for a particular physical property can be translated to other physical properties that belong to the same class.

Electrical conductivity σ , thermal conductivity λ and diffusivity D belong to the same class of physical properties, we call them collectively “transport properties”. The partial differential equations governing the respective physics have the same mathematical form [2], namely

$$\begin{aligned}\mathbf{j} &= -K\nabla g \\ \nabla \cdot \mathbf{j} &= 0,\end{aligned}\tag{A.1}$$

where \mathbf{j} is a current, K the physical property and g the field driving the

current as stated by the first equation. The second equation ensures conservation of the species that flows. In case of diffusion the number of molecules, atoms or particles is constant. In case of electrical conduction the charge is conserved and in case of thermal conduction the thermal energy is constant. Tab. A.1 shows the correspondence of the physical quantities used to describe the three transport phenomena.

A.2 Effective properties of heterogeneous materials

We here stick to the case of transport properties of a conductor-insulator sample to explain the concept of effective properties. The ideas are general though and apply equally to all physical properties of heterogeneous materials.

Using the same notation as in Sec. A.1, the transport property K within a conductor-insulator composite is a function of space, namely

$$K(\mathbf{r}) = \begin{cases} \text{const}, & \mathbf{r} \in \text{conductor} \\ 0, & \mathbf{r} \in \text{insulator} \end{cases}, \quad (\text{A.2})$$

where $\text{const} > 0$ is the transport property of the conducting phase. The spatial variation of K exactly reflects the microstructure. To describe transport through a work piece of the composite, i.e., to determine the macroscopic fluxes into it and out from it, we need to solve Eq. (A.1). Typically the length scale at which the physical property K oscillates is much smaller than the size of the work piece we are interested in. This allows to split the problem given by Eq. (A.1) and the boundary conditions describing the work piece into two. First the transport property K_e of a fictitious homogeneous medium that behaves like the composite on the macroscopic scale is determined. K_e is called effective transport property of the composite. Second the boundary value problem describing transport through the work piece is solved with the spatially modulated transport property replaced by

transport property K	applied field g	resulting current j
diffusivity D	concentration	particle flux
conductivity σ	electric potential	electrical current
thermal conductivity λ	temperature	heat flux

Table A.1: Correspondence between quantities describing different transport properties. An extended table of this kind can be found in [1].

the constant effective transport property K_e of the composite. The idea is illustrated in Fig. A.1.

Mathematically the transition means passing to the limit of a sequence of partial differential equations. The theory of homogenization provides a rigorous framework for this limit process. In practice the effective property of a composite is determined by solving the microscopic equations on a sufficiently large sample. It is convenient to choose a cuboid and to apply a constant potential drop $G > 0$ on opposing faces. From the solution of this boundary value problem the total flux $I \geq 0$ passing the sample can be computed. The effective transport property K_e is determined by the following expression

$$K_e = \frac{G/l}{I/A}, \quad (\text{A.3})$$

where A is the area of one of the faces kept at constant potential and l is the distance between the two faces at constant potential. This expression is equivalent to the first line of Eq. (A.1) for the case of a homogeneous medium.

The normalized effective transport property K_e^* characterizes the effect of the microstructure on the macroscopic behavior of a conductor-insulator composite, it is defined by

$$K_e^* = \frac{K_e}{\text{const}}, \quad (\text{A.4})$$

where const is the transport property of the conducting phase, see Eq. (A.2).

A.3 Diffusion and random walks

The spreading of an ink drop in water with time is called diffusion: concentration gradients decay with time. The erratic (random) movement of small particles suspended in water is called Brownian motion. Einstein developed a theory that links these two effects [3]. He derived a relation between the diffusivity (also known as diffusion constant) and the mean square displacement of a particle subject to Brownian motion for a certain time. Brownian motion can be mimicked by random walks: a step into a random direction is taken at regular intervals. It is a nice exercise to show that the continuum limit of this discrete motion yields the diffusion equation [4]. It reads

$$\partial_t c = \nabla \cdot D \nabla c, \quad (\text{A.5})$$

where c is the concentration of the diffusing species and D is the diffusivity. Note that in the stationary case this equation

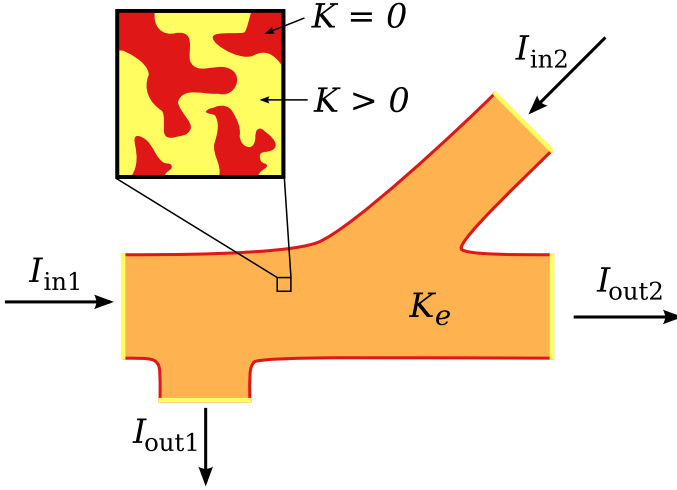


Figure A.1: Illustration of the concept of the effective property K_e of a conductor-insulator composite. For the transport through a macroscopic work piece only macroscopic fluxes I are of interest.

In an infinitely large homogeneous medium the diffusivity D for self-diffusion is given by

$$D = \frac{\langle d^2 \rangle}{6t}, \quad (\text{A.6})$$

where $\langle d^2 \rangle$ is the mean square displacement of a large number of random walks after traveling for a time t each. Note that the numerical factor 6 in the denominator is related to the dimension of space in which the movement occurs. In one- and two-dimensional space it would be 2 and 4 respectively.

Eq. A.6 can be used to compute the effective diffusivity D_e of a porous material from its microstructure. There are several studies of diffusion through model microstructures built from perfect spheres, e.g. [2, 5]. The idea is to perform random walks within the pore space and to record the square of the displacement as a function of time. According to Eq. A.6 the slope of this curve is equal to $6D_e$. The disadvantage of the mean squared displacement method is that it requires either large data volumes or periodic structures. For small aperiodic microstructures the random walks leave the microstructures too early resulting in large scatter of the data.

As pointed out in [5] the ratio Kn between the distance of one step in the random walks (corresponding to the mean free path of the diffusing particles) and the size of the pores affects the result. For large values of Kn one speaks of Knudsen diffusion: the scattering at the pore walls dominates.

In this regime the diffusion is not described anymore by Eq. A.1.

Although completely different from the physical point of view, diffusivity is mathematically equivalent to electrical or thermal conductivity as shown in Sec. A.1. This equivalence means that these three transport properties can be computed using the same methods, i.e., in particular random walk techniques.

Exploiting mathematical analogy even more consequently Laso proposed to use random walks for obtaining selected information on the solution of specific boundary value problems based on the Fokker-Planck equation [6]. With the example of the heat equation, which is equivalent to the diffusion equation shown in Eq. (A.5), he details the implementation of all possible boundary equations.

A.4 Estimation of effective transport properties

We here present a random walk technique to estimate the normalized effective transport property K_e^* of a conductor-insulator composite from an image of its microstructure. The term transport property refers to either electrical conductivity, thermal conductivity or diffusivity, see Sec. A.1.

According to Eqs. (A.4) and (A.3) we need to determine the steady state total flux I through the binary image resulting from applying a potential drop G over opposing faces of the image. The boundary value problem to be solved is based on the partial differential equations given in Eq. A.1. Inserting the first line in the second one yields the following equation for the potential g ,

$$\nabla \cdot K \nabla g = 0. \quad (\text{A.7})$$

The solution of this equation is identical to the stationary solution of the diffusion or heat equation, see Eq. (A.5), provided the same boundary conditions are applied.

Next we exploit the relation between the diffusion equation and random walks to extract information on the stationary solution. We follow the ideas described in [6]. The potential g is proportional to the number of random walks (trajectories) per volume. Fluxes are proportional to the number of trajectories passing a certain area per time unit. Since the transport property within the insulating phase is zero, see Eq. (A.2), the boundaries between the conducting and insulating phase are impenetrable for the trajectories. The boundary held at nonzero potential is the source of the flux, hence the trajectories are started there. The sink consequently absorbs the trajectories. The whole situation is illustrated in Fig. A.2.

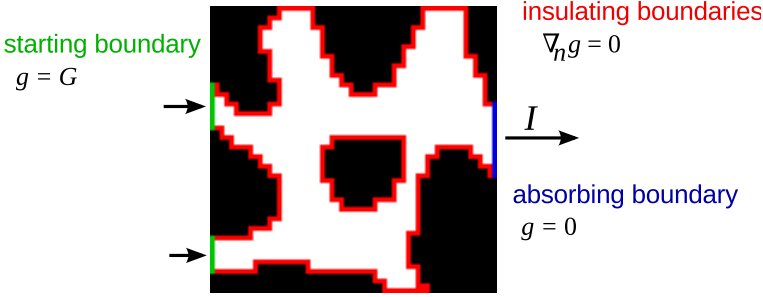


Figure A.2: Boundary conditions applied to binary image for simulation of transport by random walk technique.

In detail we implemented the following procedure. First a pair of opposing faces of the image is chosen, one serves for starting the random walks and the other one serves as destination. Next a voxel in the starting face is chosen randomly. In case it belongs to the conducting phase a random walk is started, else another voxel in the starting face is chosen randomly and checked. The random walk is performed by a sequence of jumps from the present voxel to a neighboring voxel, i.e., one sharing a face with the current voxel. Only voxels that belong to the conducting phase can be reached: if a jump would lead to an insulating voxel another destination is chosen randomly and checked again. The random walk is run until it reaches either the starting face or the destination face. After a large number of random walks has been performed an estimate for the normalized effective transport property is computed from the following expression

$$\langle K_e^* \rangle_\alpha = cd^2 \frac{A}{N}, \quad (\text{A.8})$$

where $\alpha \in \{x, y, z\}$ refers to the direction of the opposing faces, d is the distance in voxels between the opposing faces, c is the area fraction of conducting phase at the starting face, A is the number of trajectories terminated at the destination face and N is the number of trajectories started. Eq. (A.8) contains no time dependent quantities which reflects the fact that the transport property K_e is determined by the steady state situation. The number of arrived trajectories corresponds to the current flowing. The area density N/c of trajectories started corresponds to the potential drop driving the current. The square of the distance in voxels between the opposing faces serves as normalization factor. It accounts for the fact that the probability of arriving at the opposing face decreases for increasing resolution of the voxel data set.

There are three different choices for the pair of opposing faces, one for

each of the three directions in space. Therefore estimates of the normalized effective conductivity can be computed separately for the x-, y- and z-direction. For an isotropic medium all three are equal. As is typical for random walk techniques the estimation of the effective conductivity relies on a large number of random walks in order to produce a fairly accurate value. The error of the estimate scales inversely proportional to the square root of the number of random walks. Furthermore the better the resolution of the discretized microstructure the closer the simulation will be to the continuum case but also the more steps it takes for a random walk to arrive at the opposing face and the smaller will the probability be for this to occur. This is the main draw back of the method: accuracy has to be paid with over proportionally higher computational effort.

Using a two-dimensional version of the program we checked the result against results obtained by the finite element method. About 20 different binary images of 500×500 pixels were investigated. The results from the random walk technique are in satisfactory agreement with the results from the finite element computation.

Bibliography

- [1] S. Torquato, *Random heterogeneous materials : microstructure and macroscopic properties*. Springer, 2002.
- [2] K. A. Akanni, J. W. Evans, and I. S. Abramson, "Effective transport coefficients in heterogeneous media," *Chem. Eng. Sci.*, vol. 42, pp. 1945–1954, 1987.
- [3] A. Einstein, *Investigations on the theory of Brownian movement*. Dover, New York, 1926.
- [4] D. ben Avraham and S. Havlin, *Diffusion and reactions in fractals and disordered systems*. Cambridge University Press, 2000.
- [5] A. Berson, H.-W. Choi, and J. G. Pharoah, "Determination of the effective gas diffusivity of a porous composite medium from the three-dimensional reconstruction of its microstructure," *Phys. Rev. E*, vol. 83, p. 026310, 2011.
- [6] M. Laso, "Stochastic dynamic approach to transport phenomena," *AIChE J.*, vol. 40, pp. 1297–1311, 1994.

Appendix B

Characterization of microstructures

B.1 Morphological operations

We here present some tools that are part of the field of mathematical morphology [1]. First we introduce the concept of morphological operations and then define four particular operations. At the end we explain the implementation we used to apply the operations to our binary images.

Set operations alter the shape of sets. Typically two sets are combined yielding a new one, e.g. by taking their intersection or union. Morphological operations do quite the same. Typically a morphological operation Ψ acts on a binary image X , i.e. the set of pixels with value 1, with the help of a so called structuring element b . The result of such an operation is again a binary image denoted by $\Psi_b X$. In principle there is no restriction regarding the shape of a structuring element. We will however only consider structure elements in the form of discrete Euclidean balls $b_r(0)$ of radius r centered at the origin 0.

The basic building blocks of all morphological operations are the erosion ε and the dilation δ . Given the ball $b_r(0)$, the binary image X eroded by the structuring element $b_r(0)$ is defined by

$$\varepsilon_{b_r} X = \{x \in X \mid b_r(x) \subset X\}, \quad (\text{B.1})$$

where $b_r(x)$ is the structuring element centered on the point x . The action of an erosion is to shrink a set. Erosion by the structuring element $b_r(0)$ removes a surface layer of thickness r from the original set. For every binary image X there is a radius r_e such that for all $r > r_e$ the erosion of X by

$b_r(0)$ results in the empty set, i.e. a binary image containing only the value zero.

The dilation of X by $b_r(0)$ is defined by

$$\delta_{b_r}X = \{x \in X \mid b_r(x) \cap X \neq \emptyset\}. \quad (\text{B.2})$$

A dilation causes an inflation of the original set, i.e. the dilation by the structuring element $b_r(0)$ adds a layer of thickness r to the surface of the original set. For every binary image X there is a radius r_d such that for all $r > r_d$ the dilation of X by $b_r(0)$ results in the binary image containing only the value one. Erosion and dilation are dual in the following sense

$$\varepsilon_{b_r}X = (\delta_{b_r}X^c)^c, \quad (\text{B.3})$$

where the superscript c denotes the complement operator.

The collection of all sets obtained by erosion and dilation with increasing radius of the ball used as structuring element is called parallel bodies. Since the radius of digital balls is discrete and there are maximal radii for both erosion and dilation, the number of parallel bodies is finite. The radius of the balls used as structuring element can be used to parametrize the parallel bodies. By convention a negative sign is added to specify erosion, the radius $r = 0$ specifies the input image and the positive radii refer to the dilated images.

We now come to the second pair of morphological operators. They are obtained from the simplest possible combinations of the erosion and dilation. The opening of X by the structuring element $b_r(0)$ is defined by

$$\circ_{b_r}X = \delta_{b_r}(\varepsilon_{b_r}X). \quad (\text{B.4})$$

The action of opening is to remove all parts of the original set that are smaller than the structuring element. One can think of the opening \circ_{b_r} as a sieve: all “grains” that have a diameter smaller than r are removed.

The closing of X by $b_r(0)$ is defined by

$$\bullet_{b_r}X = \varepsilon_{b_r}(\delta_{b_r}X). \quad (\text{B.5})$$

It causes filling of all gaps that are smaller than the structuring element. Opening and closing are also dual operators in the sense of Eq. B.3.

We call the collection of images obtained from opening and closing by balls of increasing radius the sieving bodies of the original image. As for the parallel bodies there is only a finite number of nontrivial such sieving bodies for a given binary image. This family is also parametrized by the radii of the structuring elements used. Negative radii correspond to opened images and positive values correspond to closed images.

The computation of the four morphological operations just defined can be done in various ways. We used a method that relies on the choice of the structuring elements to be digitized balls. The actual shape of balls depends on the choice of the definition of distance. For our purpose it was most natural to use the Euclidean distance. We now illustrate the relation between distances and the morphological operations. Let's imagine for a moment a binary image X_1 that contains only one voxel with value one located at the center of the image window. For every voxel with value zero we can compute the Euclidean distance to the single voxel with value one. The gray level image $\text{EDT}(X_1)$ containing all such distances rounded to the next integer is called the Euclidean distance transform. Thresholding $\text{EDT}(X_1)$ at the level r yields the digitized Euclidean ball of radius r . For instance this binary image is the same as $\delta_{b_r} X_1$. Therefore the dilations with structuring element $b_r(0)$ of any binary image can be obtained for all $r > 0$ directly from the Euclidean distance transform of this image. The erosions by balls centered at the origin can be obtained from the Euclidean distance transform as well. To do so one exploits the duality relation, see Eq. B.3.

So now we need a way to compute the Euclidean distance transform of binary images. The square of the Euclidean distance between two points is the sum of the squared projected distances for each dimension. Saito and Toriwaki used this property to design a very efficient algorithm for the computation of the Euclidean distance transform of an image [2]. To compute all parallel bodies of a binary image is thus basically reduced to computing the Euclidean distance transform once for the binary image and once for the inverted binary image, the rest is just thresholding. The computation of the sieving bodies is much more expensive from the computational point of view, since for each opening or closing the Euclidean distance transform has to be computed twice and the second one cannot be used further.

B.2 Minkowski functionals

In the theory of geometric probability the Minkowski functionals are used to compute the probability of certain geometric events [3]. One application of this theory is stereology [4]. The Minkowski functionals span the linear space of isotropic measures on compact convex sets in d -dimensional Euclidean space. This theorem was first proven in 1957 by Hadwiger [5]. We restrict our discussion to three-dimensional Euclidean space and present definitions of the Minkowski functionals that use the notion of principle curvature radii, i.e., the minimal and maximal radius of curvature at a point of a smooth surface. Although curvature is only defined for smooth sets it is possible to apply the presented definitions for sets with edges and vertices. The trick is

to consider the sets dilated by a small ball, compute the measures and then let the radius of the ball tend to zero [4].

The volume V of a set X is defined by

$$V(X) = \int_X d\mu,$$

where $d\mu$ is the usual measure on three-dimensional Euclidean space. The surface area S is defined by

$$S(X) = \int_{\partial X} do,$$

where ∂X denotes the boundary of the set X and do is the surface measure. At every non singular point p of the boundary ∂X two principle radii of curvature $r_1(p)$ and $r_2(p)$ are defined. The integrated mean curvature M is defined by

$$M(X) = \int_{\partial X} \frac{1}{2} \left(\frac{1}{r_1} + \frac{1}{r_2} \right) do.$$

Finally the integrated total curvature K is defined by

$$K(X) = \int_{\partial X} \frac{1}{r_1 r_2} do.$$

The latter is related to the Euler characteristic χ , namely by $k = 4\pi\chi$. The Euler characteristic in turn is related to the Betti numbers [6]. We have

$$\chi = b_0 - b_1 + b_2, \tag{B.6}$$

where b_0 is the number of connected parts, b_1 is the number of handles, i.e. tunnels, and finally b_2 is the number of cavities. The definitions of the Minkowski functionals given above allow to compute analytical expressions for a ball b_R of radius R . The volume is $V(b_R) = \frac{4\pi R^3}{3}$, the surface is $S(b_R) = 4\pi R^2$, the integrated mean curvature is $M(b_R) = 4\pi R$ and the integrated total curvature is $K(b_R) = 4\pi$. For a cuboid C with side lengths a_1 , a_2 and a_3 the volume is $V(C) = a_1 a_2 a_3$, the surface is $S(C) = 2(a_1 a_2 + a_2 a_3 + a_3 a_1)$, the integrated mean curvature is $M(C) = \pi(a_1 + a_2 + a_3)$ and the integrated total curvature is $K(C) = 4\pi$, as listed in [4].

The microstructure of materials is typically very fine compared to the actual size of a sample. It is therefore reasonable to think of a microstructure as a infinitely extended but in statistical sense repetitive set. Typically only a limited volume of a microstructure is imaged. The absolute size of such an image should not affect the geometrical quantities derived from it. For the Minkowski functionals this is achieved by normalization with the volume of

the image window W . This yields so-called specific Minkowski functionals. For a set $X \subset W$, we define the specific Minkowski functionals by

$$\begin{aligned} v(X) &= \frac{V(X)}{V(W)} \\ s(X) &= \frac{S(X)}{V(W)} \\ m(X) &= \frac{M(X)}{V(W)} \\ k(X) &= \frac{K(X)}{V(W)}. \end{aligned}$$

The specific volume is the same as the volume fraction.

There is an elegant and very efficient algorithm to compute the Minkowski functionals for a binary image [4]. First the histogram of the 256 possible configurations of the 8-neighborhood of every voxel in the binary image is computed. Then all Minkowski functionals are deduced from this vector representing the neighborhood configuration histogram. For example the sum of all configurations where the first voxel has value one, i.e., the entries of the vector with odd index, yields the volume. With the proper weights the values of the other Minkowski functionals are obtained just as efficiently. Tab. B.1 shows the weights used to compute the 6-connected Euler characteristic from the histogram of neighborhood configurations. The values were computed using a MATLAB script.

The Minkowski functionals are applied in a wide range of disciplines. Typically they are computed for a family of sets, e.g. level sets of gray level images or the parallel bodies of a binary image. The latter case the resulting curves are known as the Minkowski functions of erosion/dilation radius. They are a powerful method to characterize irregular spatial structure in order to fit the parameters of geometrical models to a given microstructure [7]. The influence of image distortions on the Minkowski functions was found to be most significant for the integrated total curvature [8]. An early study using this measure concerned the connectivity in cancellous bone as a measure that is related to its strength and stiffness [9]. Mecke *et. al.* used Minkowski functions of dilation radius to show that the spatial distribution of galaxy clusters in the universe differs considerably from a Poisson process, but rather resembles a double Poisson process [10]. Another application in the field of astronomy is testing of the Gaussianity of the microwave background radiation [11]. Pore connectivity as a function of pore size was proposed by Vogel to better understand water transport in soil [12]. Becker *et. al.* have developed a theory to describe the evolution of patterns formed by dewetting thin films [13]. Hütter investigated the differences in the networks

range	values
0 ... 15	0, 1, 0, 0, 0, 0, 0, -1, 0, 1, 0, 0, 0, 0, 0, 0,
16 ... 31	0, 0, 0, -1, 0, -1, 0, -2, 0, 0, 0, -1, 0, -1, 0, -1
32 ... 47	0, 1, 0, 0, 0, 0, 0, -1, 0, 1, 0, 0, 0, 0, 0, 0,
48 ... 63	0, 0, 0, 0, 0, -1, 0, -1, 0, 0, 0, 0, 0, -1, 0, 0,
64 ... 79	0, 1, 0, 0, 0, 0, 0, -1, 0, 1, 0, 0, 0, 0, 0, 0,
80 ... 95	0, 0, 0, -1, 0, 0, 0, -1, 0, 0, 0, -1, 0, 0, 0, 0,
96 ...111	0, 1, 0, 0, 0, 0, 0, -1, 0, 1, 0, 0, 0, 0, 0, 0,
112...127	0, 0, 0, 0, 0, 0, 0, 0, 0, 0, 0, 0, 0, 0, 0, 1,
128...143	0, 1, 0, 0, 0, 0, 0, -1, 0, 1, 0, 0, 0, 0, 0, 0,
144...159	0, 0, 0, -1, 0, -1, 0, -2, 0, 0, 0, -1, 0, -1, 0, -1,
160...175	0, 1, 0, 0, 0, 0, 0, -1, 0, 1, 0, 0, 0, 0, 0, 0,
176...191	0, 0, 0, 0, 0, -1, 0, -1, 0, 0, 0, 0, 0, -1, 0, 0,
192...207	0, 1, 0, 0, 0, 0, 0, -1, 0, 1, 0, 0, 0, 0, 0, 0,
208...223	0, 0, 0, -1, 0, 0, 0, -1, 0, 0, 0, -1, 0, 0, 0, 0,
224...239	0, 1, 0, 0, 0, 0, 0, -1, 0, 1, 0, 0, 0, 0, 0, 0,
240...255	0, 0, 0, 0, 0, 0, 0, 0, 0, 0, 0, 0, 0, 0, 0, 0,

Table B.1: Weights used to compute the 6-connected Euler characteristic from the histogram of the 8-neighborhood configurations of three-dimensional images.

formed by coagulated monodisperse colloidal systems [14]. In the field of surface characterization the Minkowski functionals of surface level sets yield a generalization of the Abbott-Firestone curve [15].

B.3 Particle size from granulometry

The particle size distribution is one of the most used means to characterize the microstructure of materials. There are several definitions and methods to determine them. We here present an approach originally due to Delfiner [16]. Let W denote the image window. Given the set $X \subset W$ representing the space occupied by the phase of interest, e.g. sand grains, we compute the volume $V(\circ_{b_r}X)$ of X opened by balls of increasing radius r . The granulometry distribution is defined by

$$G(r) = \frac{V(\circ_{b_r}X)}{V(X)}.$$

This function is monotonically decreasing. It describes how much volume is occupied by sand grains with radius larger than r . The negative derivative

$$-\frac{dG}{dr}(r) = \frac{-1}{V(X)} \frac{dV(\circ_{b_r}X)}{dr}$$

is the volume weighted size distribution of the sand grains X . From this the volume weighted mean particle radius is obtained by

$$r_{vwm} = - \int_0^\infty r \frac{dG}{dr}(r) dr = \int_0^\infty G(r) dr,$$

where we have integrated by parts and used the fact that $G(\infty) = 0$.

Bibliography

- [1] P. Soille, *Morphological image analysis: principles and applications*. Springer, 2nd edition ed., 2004.
- [2] T. Saito and J.-I. Toriwaki, “New algorithms for euclidean distance transformation of an n-dimensional digitized picture with applications,” *Pattern Recognit.*, vol. 27, pp. 1551–1565, 1994.
- [3] D. A. Klain and G.-C. Rota, *Introduction to geometric probability*. Cambridge University Press, 1997.

- [4] J. Ohser and F. Mücklich, *Statistical Analysis of Microstructures in Materials Science*. John Wiley & Sons, Ltd., 2000.
- [5] H. Hadwiger, *Vorlesungen über Inhalt, Oberfläche und Isoperimetrie*. Springer, Berlin, 1957.
- [6] K. Jänich, *Topologie (7. Aufl.)*. Springer, 2001.
- [7] C. H. Arns, M. A. Knackstedt, and K. R. Mecke, “Characterization of irregular spatial structures by parallel sets and integral geometric measures,” *Colloids Surf, A*, vol. 241, pp. 351–372, 2004.
- [8] C. H. Arns, M. A. Knackstedt, and K. R. Mecke, “3d structural analysis: sensitivity of minkowski functionals,” *Journal of Microscopy*, vol. 240, pp. 181–196, 2010.
- [9] A. Odgaard and H. J. G. Gundersen, “Quantification of connectivity in cancellous bone, with special emphasis on 3-d reconstructions,” *Bone*, vol. 14, pp. 173–182, 1993.
- [10] K. R. Mecke, T. Buchert, and H. Wagner, “Robust morphological measures for large-scale structure in the universe,” *Astron. Astrophys.*, vol. 288, pp. 697–704, 1994.
- [11] S. Winitzki and A. Kosowsky, “Minkowski functional description of microwave background Gaussianity,” *New Astron.*, vol. 3, pp. 75–99, 1997.
- [12] H. J. Vogel, “Morphological determination of pore connectivity as a function of pore size using serial sections,” *Eur. J. Soil Sci.*, vol. 48, pp. 365–377, 1997.
- [13] J. Becker, G. Grün, R. Seemann, H. Mantz, K. Jacobs, K. R. Mecke, and R. Blossey, “Complex dewetting scenarios captured by thin-film models,” *Nat. Mater.*, vol. 2, pp. 59–63, 2002.
- [14] M. Hütter, “Heterogeneity of colloidal particle networks analyzed by means of minkowski functionals,” *Phys. Rev. E*, vol. 68, p. 031404, 2003.
- [15] J. Schmähling and F. A. Hamprecht, “Generalizing the Abbott-Firestone curve by two new surface descriptors,” *Wear*, vol. 262, pp. 1360–1371, 2007.
- [16] P. Delfiner, “A generalization of the concept of size,” *J. Microsc.*, vol. 95, pp. 203–216, 1972.

Acknowledgments

First I would like to thank my supervisors Prof. Ludwig Gauckler and Prof. Markus Hütter for their trust in me and the freedom I enjoyed during my time as PhD student. The topic was new to all of us and we all had to learn some hard lessons. Discussions and written feedback have greatly enhanced the quality of this thesis. I am especially grateful to Prof. Gauckler for constantly motivating me and urging me to give talks on FIB-SEM and its use for the analysis of microstructures.

With former and present “nonmets” I could enjoy several entertaining social gatherings and excursions. I am happy to thank all members of the institute and in particular my office mates for friendship and collegiality. Special thanks go to Dr. Brandon Bürgler, Dr. Jennifer Rupp, Barbara Scherrer, Dr. Iwan Schenker, Meike Schlupp and Ben Seeber for thrilling discussions and pleasant off time activities. Furthermore I would like to thank Johannes Keppner for conducting his diploma thesis under my guidance, I wish you all the best for your own PhD.

At the beginning of my time at the Institute for Nonmetallic Inorganic Materials I had the chance to be involved in the purchase process of the first FIB-SEM for the ETH Zurich. During the whole process from evaluation to installation I have met several people engaged in the field of microscopy. I am thankful to all of them. In particular I would like to acknowledge heartily Dr. Marco Cantoni and Dr. Otte Homan for their advice on technical questions and the purchase process in general. The work with the NVision40 was difficult at times, but thanks to Philippe Gasser, Dr. Kasten Kunze, Peter Tittmann and Jean-Pierre Lorenz the problems were always solved in due time. Furthermore I want to thank Dr. Heniz Lüscher and Dr. Harry Brandenberger for financial support that in particular allowed to have the backbone paper freely available online.

The Cortona week 2006 will always be in my memory: I found new friends with whom I enjoyed interesting talks, deep philosophical discussions and practiced arts as well as sports. I want to thank all participants and of course the organizers who made this wonderful week possible.

Special thanks go to Dr. Marc Petitmermet from the IT support of the Materials department for helping me out whenever I got in trouble with the Linux workstation on which the computations for this thesis were carried out.

My duty as teaching assistant for the introductory lecture on materials science was an interesting and pleasant experience. I want to express my gratitude to Prof. Peter Uggowitzer and all my assistant colleagues Dr. Ulrich Mücke, Dr. Fabian Eckermann, Dr. Anja Haenzi, Michael Schinhammer, Minh Becker and Dr. Dorota Koziej for the good collaboration.

I am indebted to Prof. Ralph Spolenak, Prof. Jürg Fröhlich, Prof. Camillo De Lellis, Elisabetta Chiodarolli, Prof. Andrei Gusev and Prof. Hans-Christian Öttinger for interesting and helpful discussions.

I am grateful to Dr. Roger Wepf and Prof. Vanessa Wood for taking over the duty of being co-referees of my thesis. I also want to thank Roger for giving me the opportunity to join the electron microscopy center of ETH Zurich (EMEZ) as scientific co-worker.

For good discussions at lunch, relaxing coffee breaks and pleasurable evening beers I thank all my friends who used to work or still are working at the Hönggerberg: Ralf Streichan, Dr. Andreas Rüegg, Dr. Sven Burkardt, Dr. David Märki, Dr. Wei Hu and Dr. Marc Dusseiller.

Very special thanks go to my family for their support and patience throughout the time of my PhD-thesis. I could not have survived without you!

Curriculum Vitae

Joakim Reuteler

born on June 15th, 1979 in Schaffhausen, Switzerland

citizen of Saanen (BE)

Swiss / Swedish nationality

married, daughter Jelina born in 2008

Education

Sep.'05 – Mar.'12 **PhD Thesis**

“Microstructures and transport properties of heterogeneous materials”

Institute for Nonmetallic Inorganic Materials, Department of Materials, ETH Zurich, Switzerland

Oct.'00 – Apr.'05 **Studies of Physics**

Diploma thesis: “Quantum mechanical particles scattering off a dynamical target”

Department of Physics, ETH Zurich, Switzerland

Aug.'94 – Jun.'99 **Matura Tyus C**

Mathematics and Natural Sciences

Gymnasium Lerbermatt, Köniz, Switzerland

Publications

- ◇ “Backbone of conductivity in two-dimensional metal-insulator composites”

J. Reuteler, M. Hütter and L.J. Gauckler
Journal of Applied Physics **110**, 024909 (2011)

Selected oral presentations

- ◇ “Backbone of conductivity in two-dimensional conductor-insulator composites”
J. Reuteler, M. Hütter and L.J. Gauckler
International Symposium on transport in porous materials (August 19-20, 2010, PSI Viligen, Switzerland)
- ◇ “Materials’ functionality and microstructure: Porous Ni-Ce_{1-x}Gd_xO_{2-x/2} cermet anodes in solid oxide fuel cells”
J. Reuteler and L.J. Gauckler
SSOM – DGM/DGE – ASEM Workshop Arbeitskreis FIB (July 3-4, 2008, Luzern Switzerland)
- ◇ “Microstructure and conductivity of metal-insulator composites”
J. Reuteler, M. Hütter and L.J. Gauckler
European Congress on Advanced Materials and Processes EUROMAT (September 10-13, 2007, Nürnberg, Germany)
- ◇ “FIB/SEM in materials research”
J. Reuteler and L.J. Gauckler
First MRC Symposium (June 29, 2006, ETH Zurich, Switzerland)
- ◇ “Introduction to Focused Ion Beam (FIB)”
J. Reuteler and L.J. Gauckler
Seminar of Institute for Nonmetallic Inorganic Materials (November 17, 2005, ETH Zurich, Switzerland)

Poster presentations

- ◇ “Focused Ion Beam Scanning electron microscope”
J. Reuteler and L.J. Gauckler MNSP Industry Day (May 8, 2008, ETH Zurich, Switzerland)
- ◇ “Microstructure and conductivity of metal/insulator composites”
J. Reuteler, M. Hütter and L.J. Gauckler
Second MRC Symposium (September 10, 2007, ETH Zurich, Switzerland)

- ◇ “Characterization of spatial structures by means of Minkowski functionals”

J. Reuteler, M. Hütter and L.J. Gauckler

First MRC Symposium (June 29, 2006, ETH Zurich, Switzerland)

Supervised undergraduate students

- ◇ Johannes Keppner (RWTH Aachen), Diploma thesis, “Relation between microstructure and electrochemical properties of platinum thin film electrodes for solid oxide fuel cells”
- ◇ Belinda Schmied, Thomas Bächler, Tobias Bachman, tutor for course Forschungslabor, Department of Materials ETH Zurich